universität innsbruck

Mode temperature analysis of a readout resonator

A master's thesis submitted to the faculty of mathematics, computer science and physics, of the University of Innsbruck
in partial fulfillment of the requirements for the degree of

Master of Science (MSc)

carried out at the Institute of Experimental Physics under the supervision of
Dr. Gerhard Kirchmair

Presented by

Alvise Borgognoni

Abstract

The main objective of this thesis is to measure the temperature of the mode of the readout resonator coupled to the transmon qubits. A second objective is to benchmark the thermal baths associated with the microwave lines wired to the quantum system (i.e. readout resonator and qubits). In order to accomplish these tasks, the coherence properties of the transmon qubits are monitored under different time domain experiments. In other words, the qubits represent the "quantum sensors" used to measure the temperature of the system.

The models used in order to describe the connection between the coherence properties of the transmon qubits and the environment are the Linblad master equation (see chapter 3) and the Johnson-Nyquist noise propagation along the microwave lines (see chapter 4). The measured temperature of the readout resonator mode represents an upper limit for the temperature of the resonator. The temperature measurements of the readout resonator are consistent with the theoretical predictions in the two cooldowns. Indeed, for the first cooldown the measured temperatures of the readout cavity are $T_{cav} \leq 81(1)\,\mathrm{mK}$ and $T_{cav} < 76(1)\,\mathrm{mK}$ while the predicted temperature is 67 mK; for the second cooldown the measured temperature is $73(1)\,\mathrm{mK}$ while the predicted temperature is 63 mK. The model though strongly deviates in the prediction of the temperature of the qubits for both of the cooldowns by more than 50 mK. This points to an unknown "hot" reservoir were coupled resonantly to the qubits. Further measurements should be performed in order to verify the reason and the reproducibility of this phenomena.

Contents

List of Figures

Chapter 1

Introduction

Over the past twenty years the field of superconducting quantum circuits has maturated from a predominantly basic research endeavour to one that increasingly explores the engineering of larger-scale superconducting quantum system [1]. A particular "large" system of interest in the field of quantum information and computation is represented by the quantum computer. One recent example for the central role of the Circuit QED field on quantum information and computation and large scale systems is represented by the demonstration of the so called "Quantum advantage" [2]. In this experiment a processor made of 53 superconducting qubits has performed a computational task beyond the capabilities of supercomputers.

The essential advances that have enabled the development of multiqubit systems include improvements in the energy relaxation time T_1 and coherence time T_2 [3, 4], which have risen by five orders of magnitude from the early results of Nakamura [5]. As T_1 increases, T_2 becomes increasingly sensitive to the presence of dephasing [6, 7, 8]. For transmon qubits, one of the main channels of dephasing is represented by the residual thermal population in the readout cavity [7]. This can be explained by the fact that in the dispersive regime each photon populating the cavity shifts the qubit a frequency shift by χ: stochastic fluctuations of the photon number in the cavity due to thermal radiation lead to a dephasing thermal rate Γ_{th}^{ϕ} proportional to the average number of thermal photons n_{th} populating the cavity.

The main objective of this thesis is indeed to measure the mean number of photons n_{th} populating the readout cavity (i.e. the temperature of the mode coupled to the qubit). In order to accomplish this task, the dephasing of the transmon qubits is measured with time domain experiments. In other words, the qubits represent the "quantum sensors" that are used in order to measure the temperature of the mode of the readout cavity through their coherence properties.

The source of thermal noise is generally addressed by Johnson-Nyquist noise coming from control and measurement microwave lines [9]. An attempt to benchmark the reservoirs associated with the microwaves lines is made. In order to accomplish this task, the temperature measurements are performed in two consecutive cooldowns, in which the configurations of the microwave lines are kept fixed (i.e. the temperature of the reservoirs remains the same) but different "couplers" between the quantum system and the input line are inserted in order to change the coupling between the quantum system and the reservoirs in the two different cooldowns. As a result of these measurements, a new configuration of the microwave lines is proposed in order to provide a colder environment for the quantum system.

Chapter 2

Basic concepts

2.1 Quantum information

Computer Science and Information Science deals with the fundamentals of storing information and processing information. Usually, those processes are carried out by warm and macroscopic devices (classical computers) that obey to the laws of Classical Mechanics. The information is stored in collections of bits, that represent a logical state that can have two values, 0 or 1. The information processing is carried out with processors who perform gate operation on the bit collections.

In a similar way, Quantum Information studies the mechanisms of storing and processing the information with devices obeying the laws of Quantum Mechanics. The fundamental unit of information is represented by a qubit (Quantum Bit), an ideal two level system, whose logical state is described by the wavefunction $|\psi\rangle$. The quantum bit has the possibility to represent the analog classical states ($|0\rangle$, $|1\rangle$) but also all the infinite possible superposition of them ($|\psi\rangle = a\,|0\rangle + b\,|1\rangle$). The information processing is carried out with Quantum Gates, that can be realized as Hamiltonian terms which are switched on for a time interval that govern the evolution of the quantum mechanical state.

The main requirements needed in order to achieve physical implementations of quantum computation are nicely outlined in the so called "DiVincenzo criteria" (see [10]). In the present thesis, just single qubit experiments are performed, thus a subset is only needed. Following the same logic of the DiVincenzo criteria, the main ingredients required in order to perform single qubit experiments will be outlined in the following sections.

2.1.1 The quantum bit

The quantum bit is the fundamental building block of quantum computation and quantum information [11]. A qubit is simply a quantum two-level system like the two states of a spin 1/2 particle, the ground and excited states of an atom, the vertical and horizontal polarization of a single photon [10] or like the charge states of an electron in a double dot potential [12]. According to the rules of Quantum Mechanics, the *state* of the qubit is defined by the wavefunction of the two level system

$$
\begin{aligned}
&|\psi\rangle = a\,|0\rangle + b\,|1\rangle \\
&1 = a^2 + b^2 \\
&a\,,\, b \in \mathbb{C}
\end{aligned}
$$

which can be described as a two-dimensional complex vector space [11]. The states $|0\rangle$ and $|1\rangle$ are known as *computational basis states*, and form an orthonormal basis for this vector space [11]. The density matrix that describes the qubit is simply

$$\rho = \begin{pmatrix} |a^2| & a\,b^* \\ a^*b & |b^2| \end{pmatrix}$$

where the diagonal elements represent the probability of finding the qubit in the $|0\rangle$ or $|1\rangle$ state, and the off diagonal elements (called *coherences*), represent the probabilty of finding the qubit in a *coherent* superposition between the states.

Another convenient representation of the qubit state is through the vector representation in spherical coordinates in the Bloch sphere (see fig. 2.1.1)

$$|\psi\rangle = \cos\frac{\theta}{2}|0\rangle + e^{i\phi}\sin\frac{\theta}{2}|1\rangle$$

where θ is the zenithal angle and ϕ is the azimuthal angle. The z axes is the quantization axes of the system, where the north pole points to the $|0\rangle$ state and the south pole points to the $|1\rangle$ state.

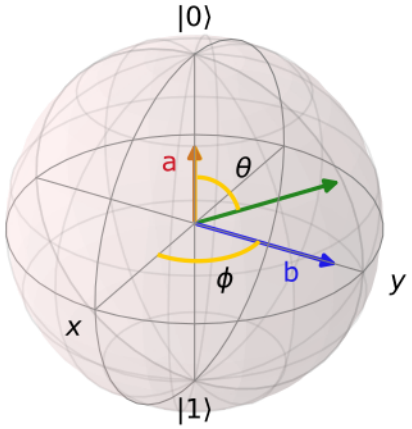

Figure 2.1.1: Bloch sphere representation of an arbitrary state $|\psi\rangle$ of a two level system. The z axis, called *longitudinal* axis, represents the quantization axis of the system. The projection of the state vector $|\psi\rangle$ along this axis (called *polarization*) can be found by calculating the expectation value of the σ_z operator $\langle\psi|\,\sigma_z\,|\psi\rangle$. The x and y axes form the *transverse plane* and the projection of the state vector along these axes can be found by calculating respectively the expectation values of the σ_x and σ_y operators.

2.1.2 State manipulation

In order to perform quantum computation on a qubit a "universal" set of quantum gates is needed. A quantum algorithm is typically specified [13] as a sequence of unitary transformations U_1, U_2, U_3,$\cdots$, each acting on a small number of qubits [10].

The most straightforward transcription of this into a realization is to identify Hamiltonians which generate these unitary transformations, viz. $U_1 = e^{-i/\hbar\int H_1 t}$, $U_2 = e^{-i/\hbar\int H_2 t}$, $U_3 = e^{-i/\hbar\int H_3 t}$, etc: then, the physical apparatus should be designed so

that H_1 can be turned on from time 0 to time t, then turned off and H_2 turned on from time t to time $2t$, etc. [10].

In the context of single qubit experiments, this requirement means that we have to be able to manipulate in a deterministic manner the state of the qubit from some initial state ψ_i to a final state ψ_f by engineering a time evolution operator $U(t-t_0)$. This time evolution operator can be engineered by adding a time dependent term in the qubit Hamiltonian

$$H = H_0 + V(t), \tag{2.1.1}$$
$$\psi_I(t) = e^{\frac{i}{\hbar}H_0 t}\,\psi_S(t), \tag{2.1.2}$$
$$V_I(t) = e^{\frac{i}{\hbar}H_0 t}\,V(t)\,e^{-\frac{i}{\hbar}H_0 t}, \tag{2.1.3}$$
$$\psi_I(t) = U_I(t-t_0)\psi_I(t_0), \tag{2.1.4}$$
$$U_I(t-t_0) = T\left\{\exp\left[-\frac{i}{\hbar}\int_{t_0}^{t} V_I(t)\,dt\right]\right\}, \tag{2.1.5}$$

where H_0 represents the qubit Hamiltonian, $V(t)$ is the time dependent interaction term, $\psi_I(t)$ represents the state of the qubit at a time t in the interaction picture, T is the time ordering operator and $U_I(t-t_0)$ is the time evolution operator in the interaction picture.

A useful representation of the action of the time evolution operator in the interaction picture on the qubit state can be depicted in the Bloch sphere representation (see fig. 2.1.2).

Let's imagine for example that the time dependent interaction term in eq. 2.1.3 has the simple form $V_I(t) = \frac{1}{2}\left(\theta_x(t)\sigma_x\right)$. The time evolution operator $U_I(t-t_0)$ generated by this Hamiltonian term is

$$U_I(t-t_0) = e^{-\frac{i}{\hbar}\int_{t_0}^{t} V_I(t)}, \tag{2.1.6}$$
$$U_I(t-t_0) = e^{-\frac{i}{2\hbar}\Theta_x|_{t_0}^{t}\sigma_x}, \tag{2.1.7}$$
$$U_I(t-t_0) = R_x(\Theta_x), \tag{2.1.8}$$
$$R_x(\Theta_x) = \begin{pmatrix} \cos\frac{\Theta_x}{2} & -i\sin\frac{\Theta_x}{2} \\ i\sin\frac{\Theta_x}{2} & \cos\frac{\Theta_x}{2} \end{pmatrix} \tag{2.1.9}$$

which results to be nothing else than the rotation operator along the x axis $R_x(\Theta_x)$.

It is easy then to imagine that a general time evolution operator $U_I(t-t_0)$ composed by a sequence of unitary transformations U_1, U_2, U_3,$\cdots$ in the Bloch sphere representation acts as a composition of rotation operators $R_{\hat{n_1}}(\Theta_1)$, $R_{\hat{n_2}}(\Theta_2)$, $R_{\hat{n_3}}(\Theta_3)$,$\cdots$ that moves the state vector from one point to another in the Bloch sphere (see see fig. 2.1.2)

2.1.3 Qubit readout

One fundamental requirement for performing quantum computation tasks (and single qubit experiments as well) is the ability to read the state of the qubit. For example, if the density matrix of the qubit is

$$\rho = \begin{pmatrix} |a^2| & a\,b^* \\ a^*b & |b^2| \end{pmatrix}$$

in an ideal experiment the qubit readout should give outcome "0" with probability $|a^2|$ and outcome "1" with probability $|b^2|$. In addition, if after the readout procedure the

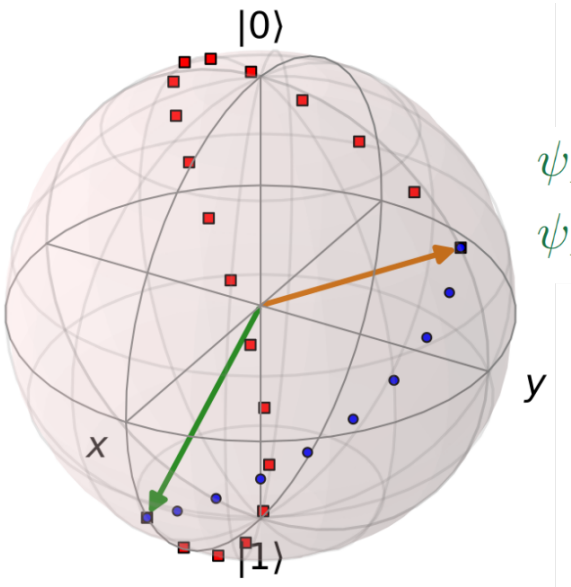

Figure 2.1.2: State manipulation representation on the Bloch sphere. The initial state $\psi_I(t_0)$ is depicted as an orange vector, while the final state $\psi_I(t)$ is depicted as a green vector. The blue dots and the red dots represent two of the infinite paths that can lead to this state manipulation, called *single qubit gate*. The trajectories of the state evolution are uniquely determined by the engineered time evolution operators ($U_I(t-t_0)$,$U_I(t-t_0)$) that can be described as compositions of $R_{\hat{n}}(\theta)$ rotation operators.

qubit state is projected in the same state that has been read, the readout measurement is called *nondemolition* measurement.

Given that there is a great variety of platforms suitable for quantum computation, it is not surprising that multiple readout techniques exist. For example, for ion qubits, one common form of readout consists of the measurement of the fluorescence of a bright state (low lifetime) of the ion which is conditionally populated by an imaging laser in resonance with the transition between the bright state and one of the two level of the qubit.

Another example is the light polarization measurement, performed by means of polarized beam splitter and photodetectors on the single photons polarization qubits. In our field of superconducting qubits, the most common form of readout is the so called *dispersive readout* (described in detail in section 2.2.6) in which the state of the qubit can be measured from the state-dependent frequency shift of a cavity called *readout resonator*.

2.2 Circuit QED

The interaction of atoms and optical photons inside cavities is described by the well known field of Cavity QED. In the following sections we are going to describe the fundamentals of the Circuit QED framework, in which superconducting qubits and microwave photons interact in a microwave resonator.

2.2.1 The LC circuit quantization

In order to understand the structure and dynamics of readout resonators and superconducting qubit it is important to be familiar with quantum and classical properties of the LC resonator.

LC circuits are the lumped element description of microwave resonators: they are used in a variety of applications, including filters, oscillators, frequency meters and tuned amplifiers [14]. In these systems energy oscillates between electrical energy in the capacitor C and magnetic energy in the inductor L.

The instantaneous time-dependent energy $E(t)$ in each element can be described in terms of its current and voltage

$$E(t) = \int_{-\inf}^{t} I\left(t'\right) V\left(t'\right) dt'$$

if we describe the generalized flux as

$$\Phi(t) = \int_{-\inf}^{t} V\left(t'\right) dt'$$

and we use the standard relations between voltage and current for inductance and capacitance $V = L\,\frac{\mathrm{d}I}{\mathrm{d}t}$, $I = C\,\frac{\mathrm{d}V}{\mathrm{d}t}$, it is possible to recover the potential energy $\mathcal{U}_L$ and the kinetic energy $\mathcal{P}_C$ as

$$\mathcal{U}_L = \frac{1}{2L}\Phi^2$$
$$\mathcal{P}_C = \frac{1}{2}C\dot{\Phi}^2.$$

As usual, the dynamics of the system can be calculated through the Lagrangian, which is

$$\mathcal{L} = \mathcal{P}_C - \mathcal{U}_L$$
$$\mathcal{L} = \frac{1}{2}C\dot{\Phi}^2 - \frac{1}{2L}\Phi^2.$$

In order to change from the Lagrangian formalism to the Hamilton formalism, we have to apply the well known Legendre transformations. As a first step, we calculate the momentum conjugate to the flux that in our case represents the charge on the capacitor

$$Q = \frac{\mathrm{d}\mathcal{L}}{\mathrm{d}\dot{\Phi}} = C\dot{\Phi}.$$

The Hamiltonian of the system is described then by

$$H = \frac{\mathrm{d}\mathcal{L}}{\mathrm{d}\dot{\Phi}}\dot{\Phi} - \mathcal{L}$$
$$H = \frac{Q^2}{2C} + \frac{\Phi^2}{2L}$$
$$H = \frac{1}{2}CV^2 + \frac{1}{2}LI^2.$$

In order to proceed further to the quantum description of the LC resonator, we need

to promote the generalized coordinates Φ, Q to quantum mechanical operators. These quantum mechanical operators obey the commutation relation

$$\left[\hat{\Phi}, \hat{Q}\right] = i\hbar.$$

Defining the reduced flux as $\hat{\phi} = 2\pi\hat{\Phi}/\Phi_0$ and the reduced charge as $n = Q/2e$ we can rewrite the Hamiltonian as

$$H = 4E_C\hat{n}^2 + \frac{1}{2}E_L\hat{\phi}^2 \tag{2.2.1}$$

where $E_C = e^2/2C$ is the charging energy, $E_L = (\Phi_0/2\pi)^2/L$ is the inductive energy and $\Phi_0 = h/(2e)$ is the superconducting magnetic flux quantum. The advantage of the new formulation of the Hamiltonian is that the new quantum operators obey the canonical commutation relation $[\phi, n] = i$. From now on the quantum mechanical operators will be written without the hat.

The Hamiltonian in equation 2.2.1 is quadratic and therefore represents a quantum harmonic oscillator (see fig. 2.2.1). The first term represents the kinetic energy and the second term represents the quadratic potential energy with respect to the phase ϕ of the system. It is easy then to express the hamiltonian in the second quantization picture

$$n = n_{zpf}\, i\left(a - a^\dagger\right) \tag{2.2.2}$$

$$\phi = \phi_{zpf}\, i\left(a + a^\dagger\right) \tag{2.2.3}$$

$$H = \hbar\omega_r\left(a^\dagger a + \frac{1}{2}\right) \tag{2.2.4}$$

where $a^\dagger$ and a are respectively the creation and annihilation operators, $\omega_r = \sqrt{8E_CE_L}/\hbar = 1/\sqrt{LC}$ is the resonant frequency of the LC resonator, $n_{zpf} = [E_L/(32E_C)]^{1/4}$ is the zero point fluctuation of the charge variable and $\phi_{zpf} = (2E_C/E_L)]^{1/4}$ is the zero point fluctuation of the phase variable.

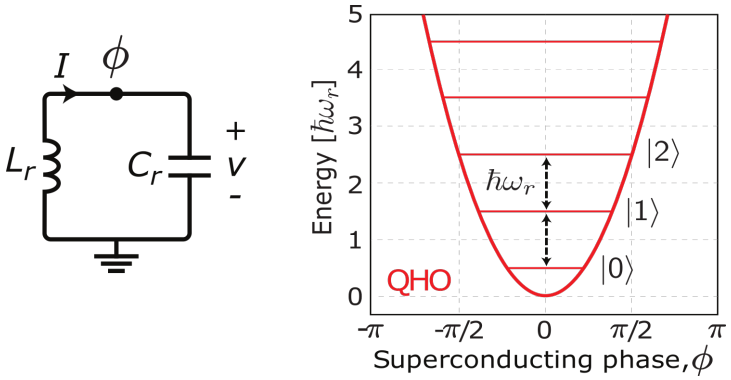

Figure 2.2.1: In the figure above, taken from [1], we can see the energy diagram for a quantized LC circuit. The parabola potential with respect to the phase across the circuit gives rise to the even energy spacing between the states typical of the harmonic oscillator.

2.2.2 The transmon qubit

As we have seen in section 2.1.1, a qubit is described as a quantum two-level system, i.e. a two dimensional Hilbert space. The necessary condition for the implementation of a physical qubit from a general quantum system is the ability to isolate a subspace with dimension 2 from the Hilbert space of that system.

As we can see from equation 2.2.4 and picture 2.2.1, the LC circuit is described by the well known harmonic oscillator, which has an infinite Hilbert space. In order to create a qubit out of the harmonic oscillator, it is necessary then to isolate the two lowest energy levels ($|0\rangle$, $|1\rangle$) forming a computational subspace [1] with an energy separation ω_{01} which is different than ω_{12} (see fig. 2.2.2). The reason behind that specification comes directly from the fact that a classical (coherent) drive applied on resonance to the resonator creates a coherent state in the resonator, i.e. moves the population of the qubit out of the computational subspace. It is well known that the even spacing between the energy levels comes from the fact that the harmonic oscillator is a *linear* element. In order to brake this equidistant energy spacing it is necessary to add some some *nonlinearity* to the system.

In the transmon qubit, the nonlinearity is provided by a Josephson Junction, that can be depicted in a circuit layout as a nonlinear inductance L_j in parallel with a capacitance C_j. The transmon qubit is engineered by shunting the Josephson junction (see fig. 2.2.2) with a capacitance C_s. In order to derive the transmon qubit Hamiltonian, we have to derive the new inductive energy $\mathcal{U}_L$ of the Josephson Junction. We start out by introducing the Josephson relations for voltage and current [1]

$$V = \frac{\hbar}{2e}\frac{\mathrm{d}\phi}{\mathrm{d}t}, \tag{2.2.5}$$

$$I = I_c \sin(\phi), \tag{2.2.6}$$

we then calculate the usual time dependent energy term

$$\begin{aligned}
\mathcal{U}_L &= \int_{-\inf}^{t} I(t')\, V(t')\, dt', \\
&= \int \frac{\hbar}{2e} I_c \sin(\phi)\, d\phi, \\
&= -\frac{\hbar}{2e} I_c \cos(\phi), \\
&= -\frac{\phi_0}{2\pi} I_c \cos(\phi), \\
&= -E_j \cos(\phi).
\end{aligned}$$

The new Hamiltonian is given by

$$H = 4E_c n^2 - E_j \cos(\phi),$$

where $E_c = 2e^2/C_\Sigma$, $C_\Sigma = C_s + C_j$ and $E_j = \frac{\phi_0}{2\pi}$. The Hamiltonian above is analogous to the Hamiltonian describing a particle with kinetic energy $4E_c n^2$ in a periodic potential. For the transmon qubit the inductive energy is much bigger than the charging energy (the shunted capacitance C_s of fig. 2.2.2 lowers the charging energy E_c) and therefore one can

expand the phase of the potential in the first terms

$$\cos(\phi) \simeq \frac{1}{2}\phi^2 - \frac{1}{24}\phi^4$$

which results in modified parabolic potential for the Hamiltonian

$$H = 4E_c n^2 - E_j\left(\frac{1}{2}\phi^2 - \frac{1}{24}\phi^4\right).$$

As we can see, the resulting Hamiltonian is equivalent to an anharmonic oscillator with quartic perturbation (Duffing oscillator). If we proceed further using the second quantization, the role of the anharmonicity in the system becomes even more clear:

$$H = \omega_{qb}\, a^\dagger a + \alpha\, a^\dagger a^\dagger a a, \tag{2.2.7}$$

$$\omega_{qb} = \left(\sqrt{8E_c\, E_j} - E_c\right), \tag{2.2.8}$$

$$\alpha = -E_c, \tag{2.2.9}$$

as we can see, the anharmonicity of the system is given by the charging energy E_c and is a *negative* number, meaning that the energy spacing between the levels diminish with higher energy. That means that a coherent drive with frequency ω_{01} in resonance with the first two energy levels ($|0\rangle$,$|1\rangle$) would be out of resonance with the frequencies relative to the other energy levels of the transmon qubit, i.e. $\omega_{12} = \omega_{01} - \alpha$, $\omega_{23} = \omega_{01} - 2\alpha$, etc. Consequently, the first two levels of the transmon qubit (see fig. 2.2.2) can be isolated from the system and therefore represent a closed computational subspace suitable for computation.

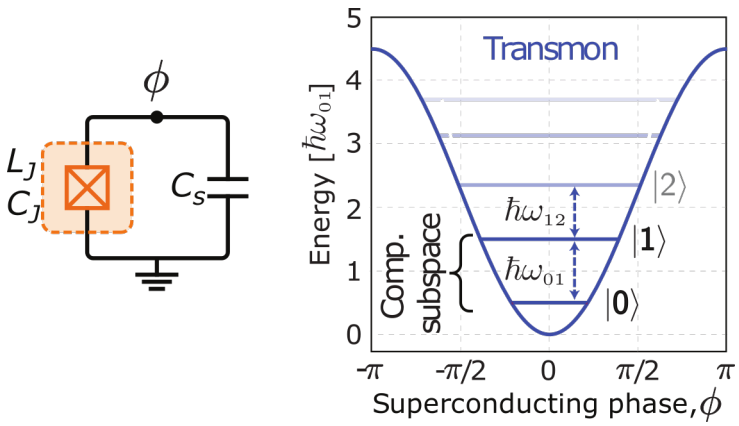

Figure 2.2.2: In the figure above, taken from [1], we can see the circuit diagram of a transmon qubit next to his energy diagram. The introduction of the Josephson junction element, which substitute the linear inductance of the LC circuit, gives rise to a cosinus like potential with respect to the phase across the circuit. This potential, for low energy levels, sets off an energy diagram typical of the anharmonic oscillators. This feature, along with a careful pulse shaping of the qubit drive, allows to create a closed computational subspace between the ground and first excited state of the qubit.

As a final remark it is interesting to note that the ratio between E_j/E_c sets up the magnitude of the charge dispersion and the anharmonicity both [15]. On one hand, since the sensitivity to the charge noise depends on the charge dispersion of the qubit, increasing

the ratio E_j/E_c means decreasing the sensitivity of the qubit to charge noise. On the other hand, increasing the ratio means reducing the (relative) energy levels anharmonicity, which limits the speed of qubit operations [15] (i.e. we have to use long pulses). Anyway, the transmon exploits a remarkable fact: the charge dispersion reduces exponentially in E_j/E_c, while the anharmonicity only decreases algebraically with a slow power law E_j/E_c [15]. That means that for a transmon qubit the ratio is usually set to $E_j/E_c \simeq 50$, an intermediate value between charge qubits and phase qubits.

2.2.3 Single qubit gates

As we have seen in section 2.1.2, in order to perform single qubit experiments, we have to be able to manipulate the state of the qubit in a deterministic manner through the qubit-drive interaction. This operation, called *single qubit gate*, can be seen as a rotation of the state vector on the Bloch sphere (see eq. 2.1.8 and figure 2.1.2).

In section 2.1.2, we have described generally the drive as a time dependent Hamiltonian term that interacts with the qubit. In the context of Circuit QED, this interaction term is introduced by a microwave pulse such that

$$\begin{aligned} H &= H_0 + V(t), \\ H &= -\frac{\omega_q}{2}\sigma_z + gV_d(t)\,\sigma_y, \end{aligned}$$

where ω_q is the frequency of the qubit, $V_d(t)$ is the time-dependent voltage of the drive pulse and g is the coupling constant between the microwave drive and the qubit.

Since the dynamics of the 2-level system is always measured in the rotating frame of the drive, it is useful to move to the interaction picture

$$\begin{aligned} V_I(t) &= e^{\frac{i}{\hbar}H_0 t}\, V(t)\, e^{-\frac{i}{\hbar}H_0 t}, \\ &= e^{-i\omega_q t\sigma_z}\, \left(g\, V_d(t)\,\sigma_y\right)\, e^{i\omega_q t\sigma_z}. \end{aligned}$$

Recalling the Baker–Campbell–Hausdorff formula

$$\begin{aligned} e^{\hat{x}}\,\hat{y}\,e^{-\hat{x}} &= \hat{y} + [\hat{x},\hat{y}] + \frac{1}{2}[\hat{x},[\hat{x},\hat{y}]] + \cdots \\ e^{\hat{x}}\,\hat{y}\,e^{-\hat{x}} &= \sum_{m=0}^{\infty}\frac{1}{m!}[\hat{x},\hat{y}]_m, \end{aligned}$$

we can simplify the form of $V_I(t)$ further, which becomes

$$\begin{aligned} V_I(t) &= g\, V_d(t) \sum_{m=0}^{\infty}\frac{1}{m!}[-i\omega_q t\sigma_z, \sigma_y]_m \\ &= g\, V_d(t)\left(\sigma_y\cos(\omega_q t) - \sigma_x\sin(\omega_q t)\right). \end{aligned}$$

Following closely the approach used in [1], we can describe the microwave pulse $V_d(t)$

as

$$
\begin{aligned}
V_d(t) &= V_0 v(t) \qquad ; \qquad v(t) = s(t)\sin(\omega_d t + \varphi), \\
V_d(t) &= V_0\, s(t)\,(I\sin(\omega_d t) + Q\cos(\omega_d t)), \\
V_I(t) &= V_0 g\, s(t)\,(I\sin(\omega_d t) + Q\cos(\omega_d t))\,(\sigma_y\cos(\omega_q t) - \sigma_x\sin(\omega_q t))
\end{aligned}
$$

where V_0 is the voltage amplitude, $s(t)$ is the envelope of the pulse, $I = \cos(\varphi)$ is the "in-phase" component of the pulse and $Q = \sin(\varphi)$ is the "out-of-phase" component of the pulse. It is important to note that the choice of describing the phase of the drive through its I/Q decomposition is closely related to the fact that we use IQ mixers for generating the pulses (see section 5.1).

If the drive is resonant with the qubit ($\omega_q = \omega_d$) and we use the RWA we can simplify further the interaction part of the Hamiltonian

$$
V_I(t) = -\frac{g}{2} V_0\, s(t)\,(I\sigma_x + Q\sigma_y).
$$

Recalling equation 2.1.6 we can built up the time evolution operator in the interaction picture

$$
U_I(t - t_0) = \exp\left(\left[\frac{i}{2} g\, V_0 I \int_{t_0}^{t} s(t)dt\right]\sigma_x \left[\frac{i}{2} g\, V_0 Q \int_{t_0}^{t} s(t)dt\right]\sigma_y\right) \tag{2.2.10}
$$

$$
\Theta(t) \equiv -g\, V_0 \int_{t_0}^{t} s(t)\, dt = -\,\Omega \int_{t_0}^{t} s(t)\, dt, \tag{2.2.11}
$$

$$
U_I(t - t_0) = \exp\left(-\frac{i}{2}\Theta(t)\,(I\sigma_x + Q\,\sigma_y)\right), \tag{2.2.12}
$$

as we can see in equation 2.2.12 and figure 2.2.3, the time evolution operator $U_I(t - t_0)$ represent a rotation operator around the x axes $R_x(\cos\phi\,\Theta(t))$ in the case of I pulses and around the y axes $R_y(\sin\phi\,\Theta(t))$ in the case of Q pulses.

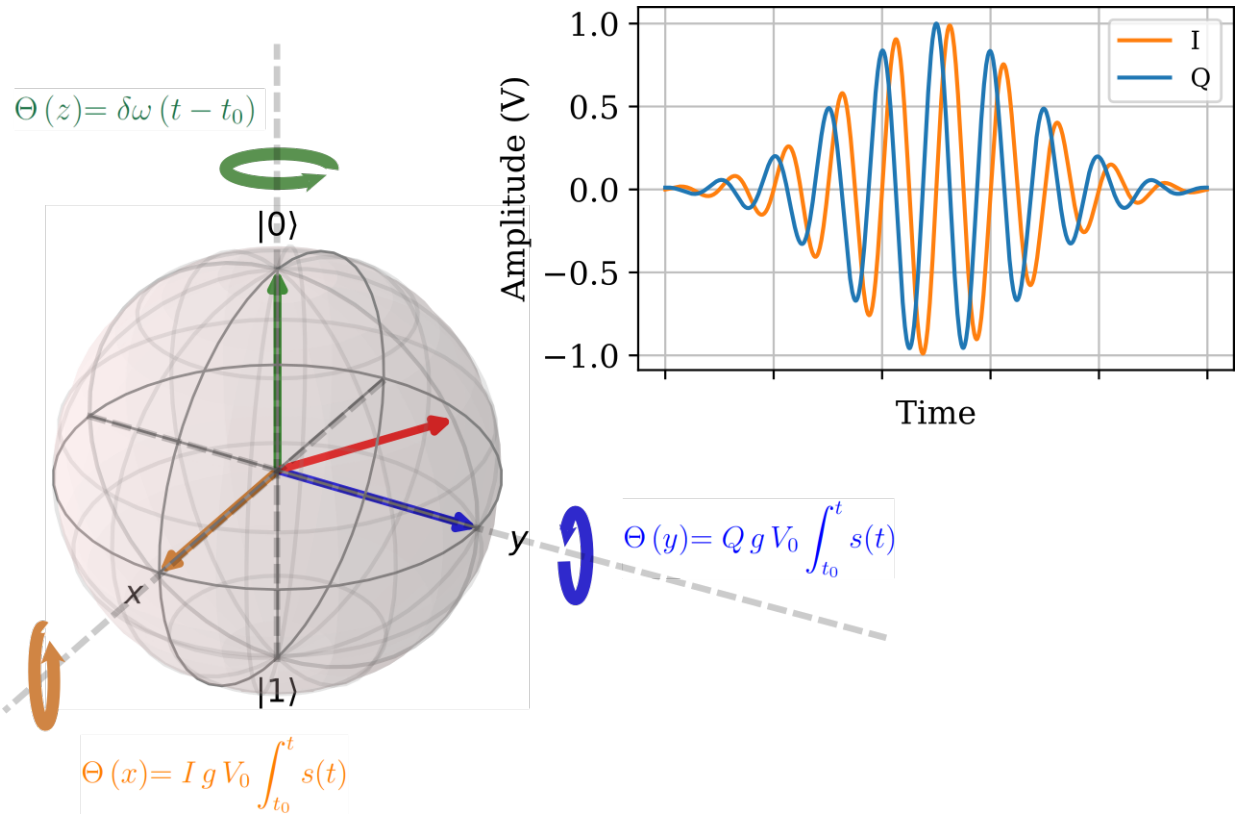

Figure 2.2.3: Rotation of a generic state vector (red vector) on the Bloch sphere generated by a microwave pulse coupled *transversally* to the qubit. As we have seen in eq. 2.2.12, the rotation of the state vector around the x (y) axes depends on the I (Q) component of the pulse, while the angle of rotation depends on the time integral of the envelope of the pulse. Since the rotating frame is defined by the drive frequency ω_d, an additional rotation around the z axes can be set off by driving the qubit out of resonance, which will cause the state vector to have a precession around the z axis with a frequency $\delta\omega$.

2.2.4 The readout resonator

As we have seen in section 2.2.1, the LC resonators can be described as Quantum Harmonic Oscillators (see eq. 2.2.4) and in the Circuit QED framework they play an analogous role to the optical cavities in the Cavity QED framework.

LC circuits are not the only way to realize microwave resonators. Another important kind of resonator is represented by the Rectangular Waveguide Cavity Resonator. The Waveguide resonators (see [14]) are nothing else than empty metallic boxes (see fig. 2.2.4). By solving Maxwell equations in the box and by imposing boundary conditions on the walls (i.e. tangent electric fields at the walls is zero) we can see that only modes with specific frequencies are allowed to exist in the cavity with

$$f_{mnl} = \frac{c}{2\pi}\sqrt{\left(\frac{m\pi}{a}\right)^2 + \left(\frac{n\pi}{b}\right)^2 + \left(\frac{l\pi}{d}\right)^2} \tag{2.2.13}$$

$$E_y = E_0 \sin\frac{m\pi x}{a} \sin\frac{l\pi z}{d} \cos\frac{n\pi z}{b} \tag{2.2.14}$$

where f_{mnl} is the frequency of the mode, a b d are the internal dimension of the cavity and c is the speed of light in the waveguide.

In general, the mode of interest of the Waveguide Cavity is the fundamental mode TE_{110} (see fig. 2.2.4 panel **(b)**) which is coupled to the transmon qubit through a dipole interaction. It is important to note that since the field of the mode goes to zero on the walls,

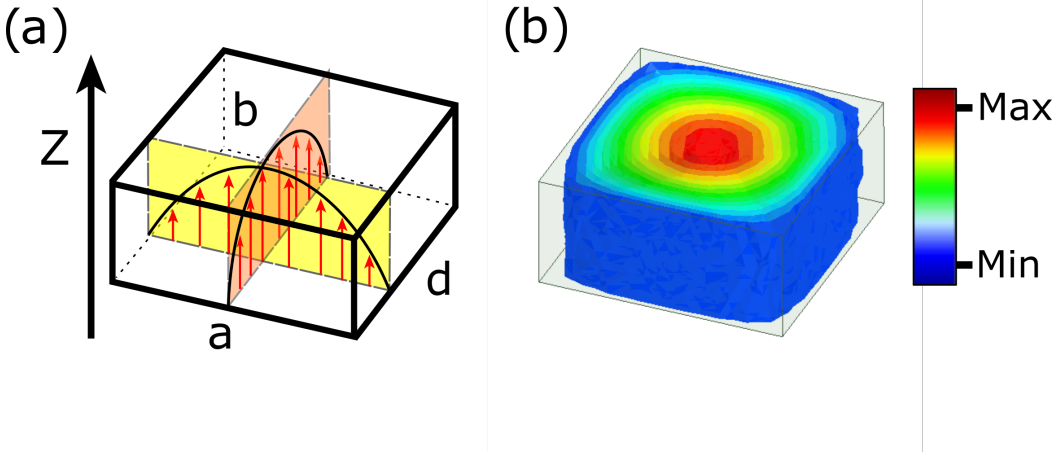

Figure 2.2.4: Waveguide microwave cavity field distribution
(a) Schematic representation of a waveguide microwave cavity with internal dimensions a, b, d. The red arrows represent the electric field for the fundamental mode TE_{110}. **(b)** Electric field magnitude for the fundamental mode TE_{110} of the cavity simulated with the HFSS [16] solver. The double sinus dependence of the electric field gives rise to the typical "sushi roll" intensity dependence of the field, from maximum intensity (red) on the center to zero intensity on the walls.

the coupling of the mode to non-magnetic impurities on the walls is minimized. Moreover, Waveguide Cavities made of superconducting materials (like aluminium) can reach very high quality factor ($Q_{int} \simeq 10^6$) due to the low internal losses at mK temperature, which makes them ideal candidates for the role of readout resonators.

2.2.5 Coupling qubit and resonator

In the previous sections (see section 2.2.2, section 2.2.4) we have described the main ingredients of the Circuit QED framework: the transmon qubit and the readout resonator. In analogy to the Cavity QED framework [17], the next step consists in coupling together the two systems. Moreover, since the qubit-cavity system is an *open* quantum system, it is important to consider the interaction between the qubit/cavity and the environment, where the environment is usually described as a large number of harmonic oscillators.

In order to understand the physical properties of such a composite system (see fig. 2.2.5), we have to pay attention to three rates: the cavity-transmon coupling rate g, the decay rate γ from the qubit to the environment, the coupling rate between the cavity and the environment κ. The relative strength between those rates and the qubit cavity detuning Δ will determine the dynamics of the system [18])

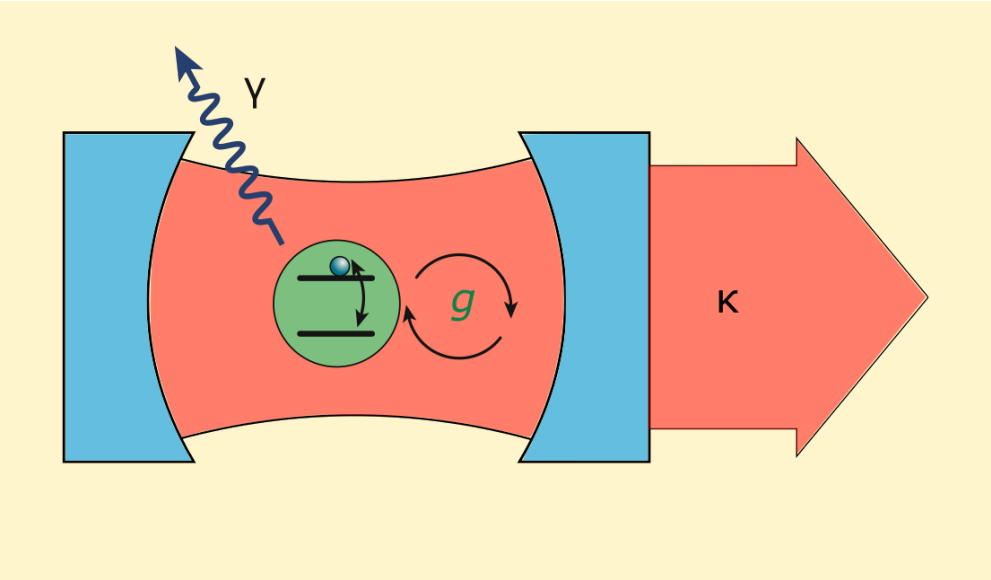

Figure 2.2.5: In the figure above we can see the general scheme of the Cavity QED architecture. The qubit is represented by the two level system in the green circle, and it is coupled to the cavity mode with a coupling constant g and to the environment with a coupling rate γ. The coupling rate of the cavity to the environment is κ. The relative strength between g, γ, κ and the qubit-cavity detuning Δ determines the dynamics of the system.

The coupling rate g between the qubit and the microwave cavity is proportional to the magnitude of the dipole moment of the transmon qubit and the electric field of the cavity at the qubit position.

The coupling rate κ represents the rate at which the cavity and the environment can exchange energy. The energy exchange can come from dissipation processes (e.g. energy dissipation due to the finite resistivity of the cavity walls) or from the exchange of photons through the microwave lines wired to the system in order to interact with it. In the case of a "cold" environment, the coupling rate κ represents the rate at which the cavity looses photons

$$\langle n(t) \rangle = n(0)\, e^{-\kappa t},$$
$$\kappa = \kappa_i + \kappa_c,$$

where $\langle n(t) \rangle$ is the mean number of photons in the cavity, κ_i is the loss rate relative to internal losses (dissipation on the cavity walls) and κ_c is the loss rate through the microwave lines.

The decay rate γ, often referred to "energy relaxation rate", represents the rate at which the qubit and the environment exchange energy. In a similar way with respect to the cavity, the energy relaxation processes are connected to dissipation processes (e.g. dissipation to the finite resistivity elements connected to the qubit) and to energy exchange, meaning interaction with photons coming from the microwave lines wired to the system. Using the language of quantum computation, γ represent the inevitable loss of quantum information owing to coupling to undesired degrees of freedom [19].

2.2.6 Dispersive readout

As we have already discussed in section 2.1.3, the ability to perform fast and reliable (high fidelity) readout of the qubit states is an important cornerstone of any quantum processor [10]. In order to perform quantum measurement on our qubit, we use a technique called *dispersive readout*, - the most common readout technique used today in the circuit QED architecture [1]- in which the transmon qubit is coupled to the readout resonator through a σ_z operator. As we have described in the previous section (see section 2.2.5) the dynamics of the qubit-cavity system depends on the relative strength between g, γ, κ, Δ.

For example, if $\Delta << g$, the energy levels of the two system hybridize and a vacuum Rabi splitting of frequency $\sqrt{n}g/\pi$ opens up, where $n = 1, 2, 3, \cdots$ denotes the resonator excitations [1]. This regime, called *resonant strong regime*, in which the excitation is swapped coherently between the qubit and the resonator, is described by the well-known Jaynes-Cummings Hamiltonian

$$H_{JC} = \omega_r \left(a^\dagger a + \frac{1}{2} \right) + \frac{\omega_{qb}}{2} \sigma_z + g \left(a\, \sigma^+ + a^\dagger \sigma^- \right), \tag{2.2.15}$$

where ω_r is the cavity frequency, ω_{qb} is the qubit frequency, g is the cavity-qubit coupling rate, a ($a^\dagger$) is the annihilation (creation) operator acting on the cavity microwave photons and σ^+ (σ^-)is the raising (lowering) operator acting on the qubit state.

On the other hand, if the qubit frequency is far detuned from the resonator such that $\Delta >> g$, κ, there is no longer a direct exchange of energy between the two systems. In this case the dispersive approximation applies [1] and the Hamiltonian of the syestem can be described by using second order perturbation in g/Δ, taken in the limit of few photons in the resonator [20, 21]:

$$H_{disp} = \left(\omega_r + \frac{\chi}{2} \sigma_z \right) \left(a^\dagger a + \frac{1}{2} \right) + \frac{\tilde{\omega}_{qb}}{2} \sigma_z \tag{2.2.16}$$

where $\chi/2 = g^2/\Delta$ is called *dispersive shift* and $\tilde{\omega}_{qb} = \omega_{qb} + \chi/2$ is the Lamb shifted frequency of the qubit. As we can see from the form of the Hamiltonian, the frequency of the cavity acquires a qubit state-dependent frequency shift χ. Moreover, the interaction term ($\chi \sigma_z a^\dagger a$) commutes with the qubit and the resonator terms: that means it is possible to do a quantum-non demolition [22] (QND) measurement of the qubit state by measuring the frequency shift of the resonator through a transmission (S_{21}) measurement of the resonator (see fig. 2.2.6).

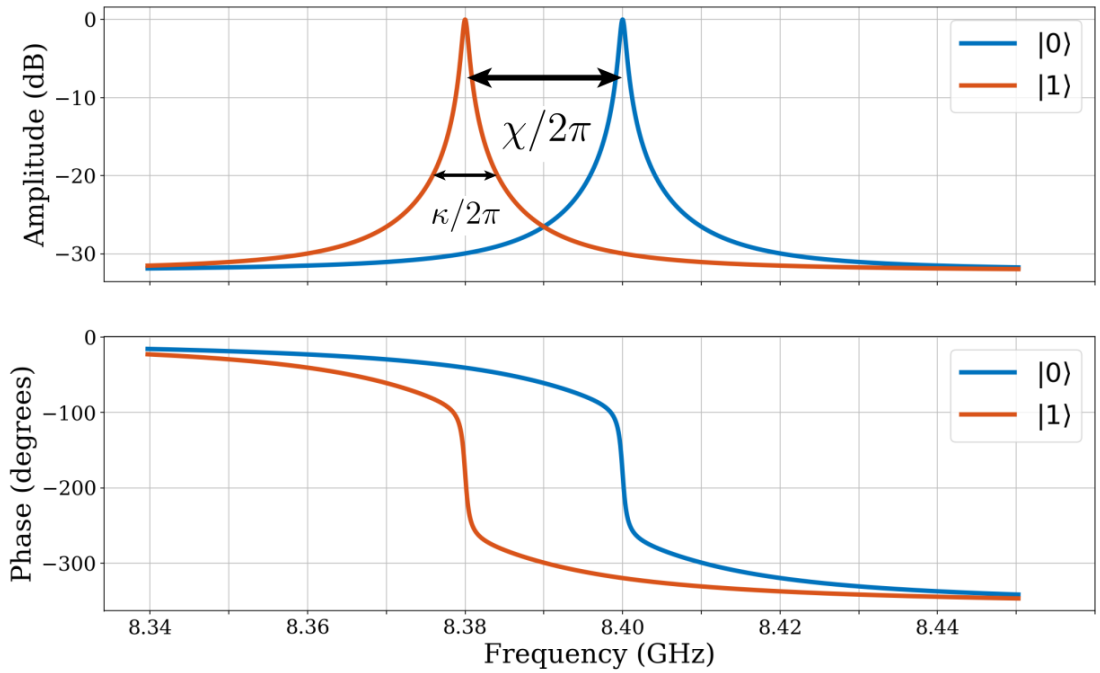

Figure 2.2.6: Transmission profile (S_{21}) of the readout resonator in the dispersive regime (see eq. 2.2.16) for the qubit in ground state (blue line) and excited state (red line). As we can see, the information of the state of the qubit is encoded both in the amplitude and the phase of the resonator, and can be extracted by probing the resonator with a *readout pulse*.

Chapter 3

Coherence and noise

The decoherence phenomenon controls the transition from the quantum world to the classical one [23]. The interaction between a quantum system and its environment leads to an energy transfer associated with a loss of quantum information with respect to a time span T_1 called *relaxation time*. Moreover, the interaction between the quantum system and its environment induces a complex entanglement between both parties that selects classical states for the system after a certain interaction time T_2 called the *coherence time* [24, 25]. In general, it is possible to regroup the decoherence phenomenon in two main groups: depolarization and dephasing.

The depolarization processes involve an irreversible energy transfer between the qubit and the environment [23] and correspond to the loss of information with respect to a $\langle \sigma_z(t) \rangle$ measurement. Dephasing processes regard the loss of information of the coherent superposition of the qubit in the excited and ground state, these are caused by random fluctuation of the qubit frequency due to interaction with the environment.

From a quantum computing point of view, this decoherence phenomenon is equivalent to random errors affecting the qubit state during an operation and thus severely hinders the implementation of a quantum computer [23]. It is clear then how important is to adopt several measures - materials engineering, qubit design, electronic design, cryogenic engineering ...- in order to create high coherent qubits.

In the present chapter, the non-unitary evolution of the open quantum system represented by the qubit and the environment (see section 3.1), resonator and environment (see section 3.2) and qubit-resonator in dispersive regime and environment (see section 3.3) will be studied by solving the master equations of these open quantum systems in the Linblad form.

3.1 Qubit and the environment

As we have already seen in section. 2.1.1, the quantum properties of a qubit can be fully described by the qubit density matrix. When the qubit interacts with the environment, the time evolution of density matrix can be calculated through the Von Neumann equations:

$$\dot{\rho}_{tot} = -\frac{i}{\hbar}\left[H_{tot}, \rho_{tot}\right], \tag{3.1.1}$$

$$H_{tot} = H_{qb} + H_{env} + H_{int}, \tag{3.1.2}$$

$$\rho_{tot} = \rho_{qb} \otimes \rho_{env}. \tag{3.1.3}$$

Since we are only interested in the dynamics of the qubit, we can at this point perform a partial trace over the environmental degrees of freedom in eq. 3.1.1 and thereby obtain a master equation for the motion of the original qubit density matrix. The most general trace-preserving and completely positive form of this evolution [26] is the Lindblad master equation for the reduced density matrix $\rho_{qb} = \mathbf{Tr}_{env}[\rho_{tot}]$

$$\dot{\rho}_{qb} = -\frac{i}{\hbar}[H_{qb}, \rho_{qb}] + \sum_n \Gamma_n \mathcal{D}[A_n]\rho_{qb} \tag{3.1.4}$$

Where $\mathcal{D}[L]\rho = \left(2L\rho L^\dagger - L^\dagger L\rho - \rho L^\dagger L\right)$ is the standard dissipation superoperator, A_n is the operator with which the qubit interacts with the environment in H_{int} and Γ_n are the corresponding rates.

As we have already described in the chapter's introduction, the rates of loss of quantum information for our qubit system are

$$\Gamma_1 \equiv \frac{1}{T_1}, \tag{3.1.5}$$

$$\Gamma_2 \equiv \frac{1}{T_2} = \frac{\Gamma_1}{2} + \Gamma_\phi, \tag{3.1.6}$$

where Γ_1 is the relaxation rate relative to *depolarization* processes (diagonal part of the qubit density matrix) and Γ_2 is the relaxation rate relative to the loss of the information of the coherent superposition of the qubit (off-diagonal elements of the qubit density matrix, called *coherences*).

As a final remark, it is important to underline the limits of applicability of the master equation in the Linblad form. The following approximations are applied:

- Separability
- Born approximation
- Markov approximation
- Secular approximation.

Using superconducting Qubits, all the approximations hold quite well with the great exception of the Markov approximation, for which we have to ensure that the system has a short memory with respect to the timescale of the qubit. Looking at the environment as a noise source, this requirement means that the noise from the environment which triggers depolarization and decoherence processes has no correlations, i.e. is a *white* type of noise. As a result, the markovian approximation holds for uncorrelated noises like thermal noise but not for noise sources like magnetic noise and charge noise as they are tipically $1/f$.

3.1.1 Depolarization (longitudinal relaxation)

In the chapter's introduction we have seen that the energy exchange between the environment and the qubit leads to a loss of information on the diagonal elements of the density matrix at a rate Γ_1. This process describes a "depolarization" of the qubit

along the quantization axis. In this language, if we define the qubit polarization as

$$\begin{aligned} p &= \langle \sigma_z \rangle \\ &= \mathrm{Tr}\left(\rho\, \sigma_z\right), \\ &= \rho_{00} - \rho_{11}, \end{aligned}$$

a qubit with polarization $p = 1$ is entirely in the ground state $|0\rangle$ at the north pole of the Bloch sphere (see fig. 3.1.1), $p = -1$ is entirely in the excited state $|1\rangle$ at the south pole of the Bloch sphere and $p = 0$ is a completely depolarized mixed state at the center of the Bloch sphere [1]. Since the z axis is the qubit quantization axis, the depolarization is often called a *longitudinal relaxation* process.

By using the standard raising and lowering operators for the qubit state σ^+ and σ^-, the annihilation and creation operators for the harmonic oscillators composing the reservoir b and $b^\dagger$ and the Pauli matrix σ_z, the Hamiltonian of the open quantum system associated to this process can be described as

$$\begin{aligned} H &= H_{qb} + H_{bath} + H_{int}, \\ H_{qb} &= \frac{\omega_{qb}}{2}\sigma_z, \\ H_{env} &= \sum_j \omega_i \left(b_j^\dagger b_j + \frac{1}{2}\right), \\ H_{int} &= g\left(\sigma^+ b + b^\dagger \sigma^-\right), \end{aligned}$$

where H_{qb} is the Hamiltonian of the qubit, H_{bath} is the Hamiltonian of the bath (taken as a large number of harmonic oscillators) and H_{int} is the energy exchanging interaction between the qubit and the reservoir in the RWA. The equations of motion of the density matrix of the qubit can be found by solving the Lindblad master equation

$$\frac{\mathrm{d}}{\mathrm{d}t}\rho_{qb} = -\frac{i}{\hbar}\left[H_{qb}, \rho_{qb}\right] + \frac{1}{2}\Gamma_{1\downarrow}\mathcal{D}[\sigma^-]\rho_{qb} + \frac{1}{2}\Gamma_{1\uparrow}\mathcal{D}[\sigma^+]\rho_{qb}, \tag{3.1.7}$$

where $\mathcal{D}[\sigma^-]\rho_{qb} = (2\sigma^-\rho_{qb}\sigma^+ - \sigma^+\sigma^-\rho_{qb} - \rho_{qb}\sigma^+\sigma^-)$ is the collapse superoperator representing the energy relaxation from the qubit to the environment at rate $\Gamma_{1\downarrow}$ and $\mathcal{D}[\sigma^+] = (\sigma^+\rho_{qb}\sigma^- - \sigma^-\sigma^+\rho_{qb} - \rho_{qb}\sigma^-\sigma^+)$ is the collapse superoperator representing the energy excitation from the environment to the qubit at rate $\Gamma_{1\uparrow}$ (see fig. 3.1.1).

For a two level system is easy to access to the analytical solution of the master equation. If we define the general density matrix of a two level system as

$$\rho = \rho_{00}\,|0\rangle\langle 0| + \rho_{11}\,|1\rangle\langle 1| + \rho_{10}\,|1\rangle\langle 0| + \rho_{01}\,|0\rangle\langle 1|,$$

where ρ_{00} represents the probability of the qubit to be in the $|0\rangle$ state, ρ_{01} is the probability of the qubit to be in the $|0\rangle\langle 1|$ state, etc. ...and we take into account that $H_{qb} = \frac{\omega_{qb}}{2}\sigma_z$ and that $\sigma^- = |0\rangle\langle 1|$ and $\sigma^+)\,|1\rangle\langle 0|$ we can rewrite the master equation as

$$\begin{aligned} \frac{\mathrm{d}}{\mathrm{d}t}\rho_{qb} = {} & \frac{-i\omega_{qb}}{2}\left(\rho_{10}\,|1\rangle\langle 0| - \rho_{01}\,|0\rangle\langle 1|\right) + \frac{1}{2}\Gamma_{1\downarrow}\left(2\rho_{11}\left(|0\rangle\langle 0| - |1\rangle\langle 1|\right) - \rho_{10}\,|1\rangle\langle 0| - \rho_{01}\,|0\rangle\langle 1|\right) + \\ & + \frac{1}{2}\Gamma_{1\uparrow}\left(2\rho_{00}\left(|1\rangle\langle 1| - |0\rangle\langle 0|\right) - \rho_{01}\,|0\rangle\langle 1| - \rho_{10}\,|1\rangle\langle 0|\right), \end{aligned}$$

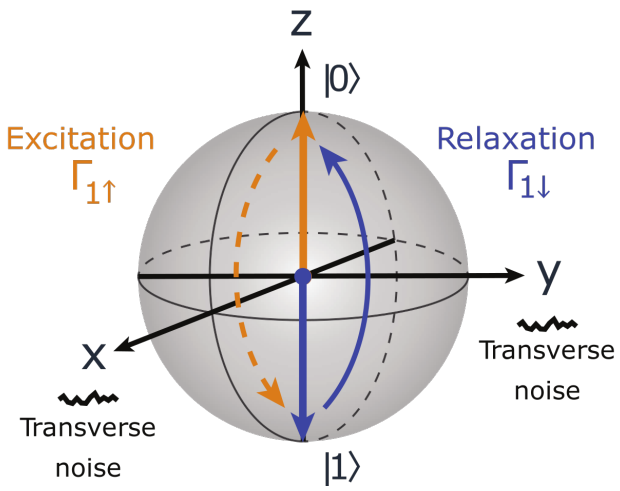

Figure 3.1.1: Longitudinal relaxation
Picture taken from [1]. Visualization of depolarization of the qubit due to the coupling to transverse noise of the open system, i.e. noise coupled through σ_x, σ_y operators. The depolarization process is always associated with an energy exchange between the qubit and the environment: $\Gamma_{1\uparrow}$ represents the *excitation* of the qubit due to energy coming from the environment while $\Gamma_{1\downarrow}$ represents the *relaxation* of the qubit due to energy released into the environment.

which can be combined in 4 differential equations

$$\begin{aligned}
\dot{\rho}_{00} &= -\Gamma_{1\uparrow}\rho_{00} + \Gamma_{1\downarrow}\rho_{11}, \\
\dot{\rho}_{10} &= \left(\frac{-i\omega_{qb}}{2} - \frac{1}{2}\left(\Gamma_{1\uparrow} + \Gamma_{1\downarrow}\right)\right)\rho_{10}, \\
\dot{\rho}_{01} &= \left(\frac{+i\omega_{qb}}{2} - \frac{1}{2}\left(\Gamma_{1\uparrow} + \Gamma_{1\downarrow}\right)\right)\rho_{01}, \\
\dot{\rho}_{11} &= \Gamma_{1\uparrow}\rho_{00} - \Gamma_{1\downarrow}\rho_{11}.
\end{aligned}$$

As we can see, the differential equations relative to the ground and excited state population of the qubit are coupled together, whereas the coherences are independent.

We proceed then by solving the coupled differential equations for the diagonal elements of the density matrix. The usual ansatz for this problem is

$$\begin{pmatrix}\rho_{00}\\ \rho_{11}\end{pmatrix}(t) = A\,\overline{x}_1\,e^{-\lambda_1 t} + B\,\overline{x}_2\,e^{-\lambda_2 t},$$

we look then for the solution of the set of eigenvalues (λ_1, λ_2) and eigenvectors ($\overline{x}_1$, $\overline{x}_2$)

$$
\begin{aligned}
&det\begin{pmatrix} -\Gamma_{1\uparrow}-\lambda & \Gamma_{1\downarrow} \\ \Gamma_{1\uparrow} & -\Gamma_{1\downarrow}-\lambda \end{pmatrix} = 0, \\
&\lambda\left(\lambda+\left(\Gamma_{1\uparrow}+\Gamma_{1\downarrow}\right)\right)=0, \\
&\lambda_1 = 0, \\
&\lambda_2 = -\left(\Gamma_{1\uparrow}+\Gamma_{1\downarrow}\right), \\
&\overline{x}_1 = \begin{pmatrix} \Gamma_{1\downarrow}/\Gamma_{1\uparrow} \\ 1 \end{pmatrix}, \\
&\overline{x}_2 = \begin{pmatrix} 1 \\ -1 \end{pmatrix}.
\end{aligned}
$$

The solution to the coupled differential equations are

$$
\begin{pmatrix} \rho_{00} \\ \rho_{11} \end{pmatrix}(t) = A\begin{pmatrix} \Gamma_{1\downarrow}/\Gamma_{1\uparrow} \\ 1 \end{pmatrix} + B\begin{pmatrix} 1 \\ -1 \end{pmatrix} e^{-\left(\Gamma_{1\uparrow}+\Gamma_{1\downarrow}\right)t}.
$$

As usual, if we assume initial conditions for the density matrix at $t = 0$

$$
\rho(0) = \begin{pmatrix} \alpha^2 & \alpha\beta^* \\ \alpha^*\beta & \beta^2 \end{pmatrix} \tag{3.1.8}
$$

$$
1 = \alpha^2 + \beta^2 \tag{3.1.9}
$$

we find that the constants A, B are

$$
\begin{aligned}
A &= \frac{\Gamma_{1\uparrow}}{\Gamma_{1\uparrow}+\Gamma_{1\downarrow}}, \\
B &= \frac{\Gamma_{1\uparrow}}{\Gamma_{1\uparrow}+\Gamma_{1\downarrow}} - \beta^2.
\end{aligned}
$$

It is interesting to note that the decay of all elements in the density matrix is always associated with the sum of the rates $\Gamma_{1\uparrow}$ and $\Gamma_{1\downarrow}$. We can define then a new rate

$$
\Gamma_1 \equiv \frac{1}{\mathrm{T}_1} = \Gamma_{1\uparrow} + \Gamma_{1\downarrow}
$$

associated with the overall depolarization process. Since the environment is typically "cold" with respect to the qubit frequency, usually Γ_1 is referred to the "relaxation rate" and T_1 is referred to "relaxation time".

The equations of motion of the density matrix can then be written as

$$
\rho_{qb}(t) = \begin{pmatrix} \frac{\Gamma_{1\downarrow}}{\Gamma_{1\uparrow}+\Gamma_{1\downarrow}} + \left(\frac{\Gamma_{1\uparrow}}{\Gamma_{1\uparrow}+\Gamma_{1\downarrow}} - \beta^2\right) e^{-\Gamma_1 t} & \alpha^*\beta\, e^{\frac{-i\omega_{qb}}{2}} e^{-\frac{\Gamma_1}{2}} \\ \alpha\beta^*\, e^{\frac{i\omega_{qb}}{2}} e^{-\frac{\Gamma_1}{2}} & \frac{\Gamma_{1\uparrow}}{\Gamma_{1\uparrow}+\Gamma_{1\downarrow}} + \left(\beta^2 - \frac{\Gamma_{1\uparrow}}{\Gamma_{1\uparrow}+\Gamma_{1\downarrow}}\right) e^{-\Gamma_1 t} \end{pmatrix} \tag{3.1.10}
$$

and in the long time limit ($t >> 1/\Gamma_1$) we find the steady state solutions

$$\rho_{qb} = \begin{pmatrix} \frac{\Gamma_{1\downarrow}}{\Gamma_{1\uparrow}+\Gamma_{1\downarrow}} & 0 \\ 0 & \frac{\Gamma_{1\uparrow}}{\Gamma_{1\uparrow}+\Gamma_{1\downarrow}} \end{pmatrix} \tag{3.1.11}$$

3.1.1.1 Qubit and thermal bath with finite temperature

Up to now, nothing has been said about the values of the rates $\Gamma_{1\uparrow}$ and $\Gamma_{1\downarrow}$ associated with the energy exchange between the environment and the qubit. As we can imagine, their value depend both on the properties of the environment (phase dependent correlation $\langle b(\omega_1)b(\omega_2)\rangle$, intensity spectrum $\langle b^\dagger(\omega)b(\omega\rangle)$ and on the coupling rate between the qubit and the environment (see [27]).

The case in which the reservoir is represented by a thermal bath is a well-known problem in the context of open quantum system. Without going into the details of the derivation (the interested readers can have a look in [27] and [28]) for a thermal bath $\langle b(\omega_1)b(\omega_2)\rangle = 0$ (i.e. thermal state does not carry any phase information) and $\langle b^\dagger(\omega_{qb})b(\omega_{qb})\rangle = n_{th}$. Following [27] and [28] the qubit to environment dumping rate γ and the depolarization rates $\Gamma_{1\uparrow}$ and $\Gamma_{1\downarrow}$ are

$$\gamma = g^2\rho^2_{env}(\omega_{qb}), \tag{3.1.12}$$
$$\Gamma_{1\uparrow} = \gamma\, n_{th}, \tag{3.1.13}$$
$$\Gamma_{1\downarrow} = \gamma(n_{th}+1), \tag{3.1.14}$$
$$\Gamma_1 = \gamma(2n_{th}+1), \tag{3.1.15}$$

where γ is calculated through the Fermi golden rule, $\rho_{env}(\omega_{qb})$ is the density of states of the thermal reservoir at the qubit frequency, n_{th} is the mean number of photons of the reservoir at the qubit frequency and g is the coupling rate between the qubit and the bath.

Since the mean number of photons in a thermal bath follows a Bose Einstein statistics, from equations 3.1.13 and 3.1.14 we can show that the excitation and relaxation rate follow a detailed balance equation:

$$\frac{\Gamma_{1\uparrow}}{\Gamma_{1\downarrow}} = \frac{n_{th}}{(n_{th}+1)}, \tag{3.1.16}$$
$$n_{th} = \frac{1}{e^{\frac{\hbar\omega_q}{k_bT}}-1}, \tag{3.1.17}$$
$$\Gamma_{1\uparrow} = \Gamma_{1\downarrow}e^{-\frac{\hbar\omega_q}{k_bT}}. \tag{3.1.18}$$

We have already seen the solutions of the equations of motion of the qubit density matrix (see 3.1.10) relative to the qubit-environment depolarization process. In order to recover the solution of the qubit density matrix dynamics in the case in which the environment is represented by a thermal bath all we have to do is to insert the particular values of the rates $\Gamma_{1\uparrow}$ and $\Gamma_{1\downarrow}$ in the solutions. It is particularly interesting to have a closer look at

the steady state solutions ($t >> 1/\Gamma_1$):

$$\rho_{qb} = \begin{pmatrix} \frac{1}{1+e^{-\frac{\hbar\omega_q}{k_bT}}} & 0 \\ 0 & \frac{1}{1+e^{+\frac{\hbar\omega_q}{k_bT}}} \end{pmatrix}. \tag{3.1.19}$$

From what we can see, the coherences of the density matrix go to zero while the populations on the ground state and excited state of the qubit reach a steady state value equal to the Boltzmann distribution for a two level system. In fact, we can see that

$$\frac{\rho_{11}}{\rho_{00}} = e^{-\frac{\hbar\omega_q}{k_bT}}.$$

At last, we calculate the value of the polarization expected for the qubit in the steady state

$$\begin{aligned} \langle\sigma_z\rangle &= \rho_{00} - \rho_{11}, \\ &= \frac{\Gamma_{1\downarrow} - \Gamma_{1\uparrow}}{\Gamma_{1\uparrow} + \Gamma_{1\downarrow}}, \\ &= \frac{e^{+\frac{\hbar\omega_q}{k_bT}} - 1}{e^{+\frac{\hbar\omega_q}{k_bT}} + 1}, \\ &= \tanh\left(\frac{\hbar\omega_q}{2k_bT}\right). \end{aligned}$$

As we can see, the steady state carries information about the temperature of the bath.

3.1.1.2 Qubit and thermal bath at zero temperature

A particular case of the previous example is represented by a qubit connected with a thermal bath at zero temperature. As a matter of fact, the mean number of photons of a reservoir at tens of milli-kelvins (the base temperature of the Cryostats in Circuit QED) at the qubit frequency (4-10 GHz) is usually a small number ($n_{th} \simeq 10^{-6}$), and in certain cases can be approximated to zero.

The rates become then

$$\begin{aligned} &\gamma = g^2\rho_{env}^2(\omega_{qb}), \\ &\Gamma_{1\uparrow} = 0, \\ &\Gamma_{1\downarrow} = \gamma, \\ &\Gamma_1 = \gamma. \end{aligned}$$

The solution of the master equation simplifies to

$$\rho(t) = \begin{pmatrix} 1 + (\alpha^2 - 1)e^{-\Gamma_1 t} & \alpha\beta^* e^{\frac{-i\omega_{qb}}{2}} e^{-\frac{\Gamma_1}{2}t} \\ \alpha^*\beta e^{\frac{i\omega_{qb}}{2}} e^{-\frac{\Gamma_1}{2}t} & \beta^2 e^{-\Gamma_1 t} \end{pmatrix}, \tag{3.1.20}$$

and we can see that in the long time limit ($t >> 1/\Gamma_1$) the qubit is found in the ground

state

$$\rho = \begin{pmatrix} 1 & 0 \\ 0 & 0 \end{pmatrix}.$$

3.1.2 Decoherence (transverse relaxation)

As we have seen in the introduction of the chapter, the decoherence processes are defined as those processes for which the information encoded in the off-diagonal element of the qubit density matrix (called "coherences") are lost [27, 1].

Since the "coherences" of the qubit density matrix describe the phase of the qubit state vector (see fig. 2.1.1), the decoherence processes can be seen as a loss of phase information of the qubit state vector. Since the phase information is encoded in the projection of the state vector onto the plane *transverse* to the qubit quantization axes, the decoherence processes are often referred to *transverse relaxation* processes. We recall that the transverse relaxation rate is defined as

$$\Gamma_2 \equiv \frac{1}{T_2}$$

3.1.2.1 Energy exchange contribution

The master equation relative to the energy exchange between the qubit and the environment has been solved in section 3.1.1. We have seen in the equation of motion of the coherences (see eq. 3.1.10 for the general case and eq. 3.1.20 for the zero temperature environment) that transverse decay rate was equal to

$$\Gamma_2 = \frac{\Gamma_1}{2}.$$

In other words we can see that the coherence time T_2 is upper bounded by the relaxation time T_1

$$T_2 = 2\,T_1.$$

3.1.2.2 Dephasing contribution

In the previous sections we have solved the master equation for the qubit coupled *transversally* (i.e. through a σ_x, σ_y operator) to the bath. Now we are in about to investigate what is the effect on the decoherence process with respect to a qubit coupled *longitudinally* (i.e. through a σ_z operator) to the reservoir.

Before starting to solve the master equation, we can already gain some intuition on the process through some heuristic consideration. It is easy to figure out that an element coupled through a σ_z operator shifts the energy levels of the qubit. Moreover, in the equation of motion of the coherences (see eq. 3.1.10) we have seen that the relative phase of the superposition between ground and excited state oscillates at the qubit frequency ω_{qb}. Consequently, a stochastic process associated with a random energy shift of the qubit would cause a random phase shift which would cause a loss of information on the phase information of the qubit (see 3.1.2). This decoherence contribution is called *pure dephasing*.

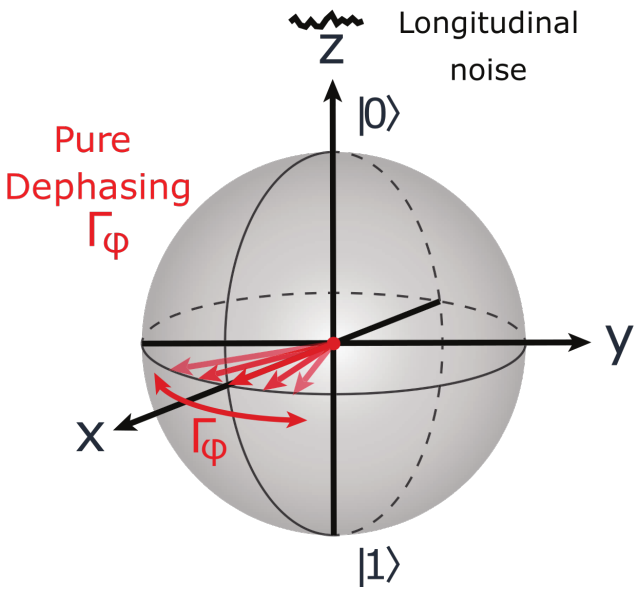

Figure 3.1.2: Pure dephasing
The picture is taken from [1]. Visualization of the dephasing of the qubit due to the coupling to longitudinal noise of the open system, i.e. Hamiltonian terms of the environment coupled to the qubit through a σ_z operator. This noise causes the frequency of the qubit to fluctuate, and it causes the Bloch vector to precess backward and forward in the rotating frame [1].

As usual, in order to get a quantitative answer on the dephasing contribution given by the interaction of between the qubit and the environment we have to solve the Linblad master equation. In the process of pure dephasing the qubit is coupled to the reservoir through a σ_z operator, and the master equation is given by

$$\frac{\mathrm{d}}{\mathrm{d}t}\rho_{qb} = -\frac{i}{\hbar}\left[H, \rho_{qb}\right] + \frac{1}{2}\frac{\Gamma_\phi}{2}\mathcal{D}[\sigma_z]\rho_{qb}$$

where ρ_{qb} is the qubit density matrix, H is the qubit Hamiltonian, $\mathcal{D}[\sigma_z]\rho = 2\sigma_z^\dagger\rho\sigma_z - \sigma_z^\dagger\sigma_z\rho - \rho\sigma_z^\dagger\sigma_z$ is the dissipation superoperator and γ_ϕ is the dephasing rate. We proceed to solving the differential equations

$$\begin{aligned}\frac{\mathrm{d}}{\mathrm{d}t}\rho_{qb} &= \frac{-i\omega_{qb}}{2}\left(\rho_{10}\left|1\right\rangle\!\left\langle 0\right| - \rho_{01}\left|0\right\rangle\!\left\langle 1\right|\right) + \\ &+ \frac{1}{2}\frac{\Gamma_\phi}{2}\left(2\left(\rho_{00}\left|0\right\rangle\!\left\langle 0\right| + \rho_{11}\left|1\right\rangle\!\left\langle 1\right| - \rho_{01}\left|0\right\rangle\!\left\langle 1\right| - \rho_{10}\left|1\right\rangle\!\left\langle 0\right|\right) - 2\rho\right) \\ &= \frac{-i\omega_{qb}}{2}\left(\rho_{10}\left|1\right\rangle\!\left\langle 0\right| - \rho_{01}\left|0\right\rangle\!\left\langle 1\right|\right) - \Gamma_\phi\left(\rho_{01}\left|0\right\rangle\!\left\langle 1\right| \rho_{10}\left|1\right\rangle\!\left\langle 0\right|\right).\end{aligned}$$

Rewriting the equations above we get

$$\begin{aligned}
\dot{\rho}_{00} &= 0, \\
\dot{\rho}_{10} &= \left(\frac{-i\omega_{qb}}{2} - \Gamma_\phi\right)\rho_{10}, \\
\dot{\rho}_{01} &= \left(\frac{+i\omega_{qb}}{2} - \Gamma_\phi\right)\rho_{01}, \\
\dot{\rho}_{11} &= 0.
\end{aligned}$$

As we can see, we end up with 4 uncoupled differential equations.

Using the same initial conditions of eq. 3.1.9 (and going to the rotating frame) we find

$$\rho(t) = \begin{pmatrix} \alpha^2 & \alpha\beta^* e^{-\Gamma_\phi t} \\ \alpha^*\beta e^{-\Gamma_\phi t} & \beta^2 \end{pmatrix}. \tag{3.1.21}$$

As a result we can see from the time evolution of the density matrix that the interaction of a qubit to the environment through a σ_z operator leads to a loss of information on the coherences at a rate Γ_ϕ, called *dephasing* rate.

3.1.2.3 Dephasing and energy exchange

As we have anticipated before, in order to recover the transverse relaxation rate Γ_2 we combine the energy-exchange contribution (see eq. 3.1.20) and the pure dephasing contribution (see eq. 3.1.21) and we find

$$\Gamma_2 = \frac{\Gamma_1}{2} + \Gamma_\phi.$$

The mechanism of the transverse relaxation through the Bloch sphere representation can be found in figure 3.1.3.

As a final step, we can write down the equation of motion for the density matrix taking into account both energy-exchange and energy shifting mechanism. For a qubit coupled to a bath at zero temperature combining eq. 3.1.20 and eq. 3.1.21 we find

$$\rho = \begin{pmatrix} 1 + (\alpha^2 - 1)e^{-\Gamma_1 t} & \alpha\beta^* e^{-\frac{\Gamma_1}{2}t} e^{-\Gamma_\phi t} \\ \alpha^*\beta e^{-\frac{\Gamma_1}{2}t} e^{-\Gamma_\phi t} & \beta^2 e^{-\Gamma_1 t} \end{pmatrix}. \tag{3.1.22}$$

More generally, the time evolution of the density matrix in eq. 3.1.22 describes the loss of information about the qubit density matrix due to the interaction of the qubit to a zero temperature environment through a *transverse* interaction (coupled through a σ_x operator) and through a *longitudinal* interaction (coupled through a σ_z operator)

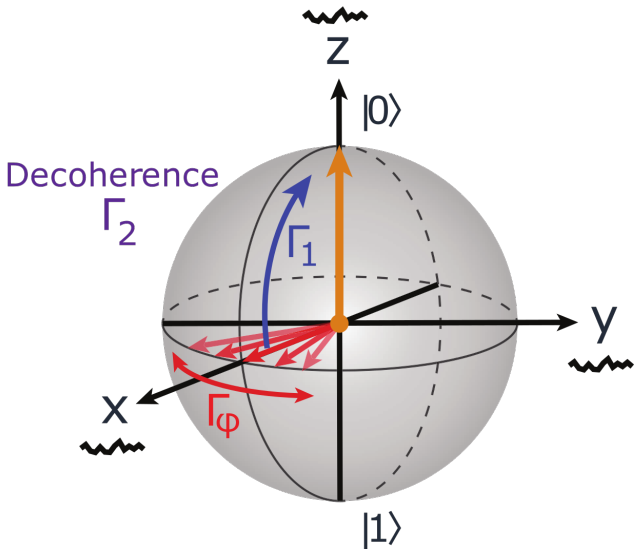

Figure 3.1.3: Transverse relaxation
The picture is taken from [1]. Visualization of the *decoherence* process of the qubit triggered by noise coupled either *longitudinally* (through σ_z operators, i.e. dephasing mechanism) than *transversally* (trough σ_x and σ_y operators, i.e. depolarization mechanism). According to the definition seen in eq. 3.1.6, the contribution of the transverse noise to the transverse relaxation rate is $\Gamma_1/2$, while the contribution of the longitudinal noise to the transverse relaxation rate is Γ_ϕ.

3.2 Resonator and the environment

The non-unitary evolution of a cavity coupled to a thermal reservoir is a well known problem in quantum optics (see [27, 28]).

The Hamiltonian of the overall system (resonator and thermal bath) is described by

$$
\begin{aligned}
H &= H_{cav} + H_{bath} + H_{int} \\
H_{cav} &= \hbar\omega_c \left(a^\dagger a + \frac{1}{2} \right), \\
H_{bath} &= \sum_j \hbar\omega_i \left(b_j^\dagger b_j + \frac{1}{2} \right), \\
H_{int} &= \hbar g_j \sum_j \left(a^\dagger b_j + b_j^\dagger a \right),
\end{aligned}
$$

where H_{cav} it the Hamiltonian of the cavity, H_{bath} is the Hamiltonian of the bath (taken as a large number of harmonic oscillators) and H_{int} is the interaction Hamiltonian that describes the energy exchange between the quantum system and the reservoir.

Using the same considerations as in section 3.1.1.1, we can write the master equation of the cavity as

$$
\frac{\mathrm{d}}{\mathrm{d}t}\rho_{cav} = -\frac{i}{\hbar}\left[H, \rho_{cav}\right] + \frac{1}{2}\kappa(n_{th}+1)\mathcal{D}[a]\rho_{cav} + \frac{1}{2}\kappa\, n_{th}\, \mathcal{D}[a^\dagger]\rho_{cav} \tag{3.2.1}
$$

where $\kappa = g^2(\omega_c)\rho_{bath}^2$ is the cavity damping term, $\mathcal{D}[a]\rho_{cav} = \left(2a\rho_{cav}a^\dagger - a^\dagger a\rho_{cav} - \rho_{cav}a^\dagger a\right)$ is the dissipation superoperator representing the energy relaxation from the resonator to the environment at rate $\kappa(n_{th}+1)$ and $\mathcal{D}[a^\dagger]\rho_{cav} = \left(2a^\dagger\rho_{cav}a - a\,a^\dagger\rho_{cav} - \rho_{cav}a\,a^\dagger\right)$ is the dissipation superoperator representing the energy excitation from the environment to the qubit at rate $\kappa\, n_{th}$.

In order to solve the master equation, we have to express the resonator density matrix in an appropriate basis (photon number representation, P representation, Q representation, Wigner function representation) and solve the relative c-number differential equations.

In the present thesis, we are particularly interested in the time evolution and steady state solution of the mean number of photons $\langle n(t)\rangle$. If we insert the relation between the mean number of photons and the cavity density matrix

$$
\langle n(t)\rangle = \mathrm{Tr}\left(\rho_{cav}\, a^\dagger a\right) \tag{3.2.2}
$$

into the master equation 3.2.1 and use the commutation algebra of the creation-annihilation operators and the cyclic property of the trace it is possible to recover the time evolution of the mean number of photons

$$
\langle n(t)\rangle = n(0)e^{-\kappa t} + n_{th}(1 - e^{-\kappa t}). \tag{3.2.3}
$$

As we can see, the mean number of photons in the cavity $\langle n(t)\rangle$ decays from the initial condition $n(0)$ to the mean number of photon of the reservoir n_{th} with a rate κ. Moreover, solving the proper master equation 3.2.1 (see [27]) it is possible to find that the population of the levels of the harmonic oscillator in the steady state follows a power law photon

number distribution of thermal light

$$\rho = \sum_n \frac{1}{1+n_{th}} \left(\frac{n_{th}}{1+n_{th}} \right)^n |n\rangle\langle n| \,. \tag{3.2.4}$$

The simulation of time evolution of the mean number of photons and the density matrix in the Fock basis and in the Wigner function representation can be found in figure 3.2.1.

it is interesting to ask ourselves the question of what happens when the cavity is coupled to multiple reservoir with mean number of photons n_{th}^j through coupling rates κ_j. If we write down the master equation

$$\frac{\mathrm{d}}{\mathrm{d}t}\rho_{cav} = -\frac{i}{\hbar}\left[H, \rho_{cav}\right] + \sum_j \frac{1}{2}\kappa_j(n_{th}^j + 1)\mathcal{D}[a]\rho_{cav} + \sum_j \frac{1}{2}\kappa_j\, n_{th}^j\, \mathcal{D}[a^\dagger]\rho_{cav},$$

one can note that by reorganizing the terms (see [29, 6])

$$\kappa_{tot} = \sum_j \kappa_j, \tag{3.2.5}$$

$$n_{eff} = \frac{\sum_j \kappa_j n_{th}^j}{\kappa_{tot}}, \tag{3.2.6}$$

we can recover the same form of the master equation for a single bath of equation 3.2.3

$$\frac{\mathrm{d}}{\mathrm{d}t}\rho_{cav} = -\frac{i}{\hbar}\left[H, \rho_{cav}\right] + \frac{1}{2}\kappa_{tot}(n_{eff} + 1)\mathcal{D}[a]\rho_{cav} + \frac{1}{2}\kappa_{tot}\, n_{eff}\, \mathcal{D}[a^\dagger]\rho_{cav}. \tag{3.2.7}$$

That means that every time that a resonator interacts with multiple baths (see fig. 3.2.2) it is possible to describe this interaction as the interaction of the resonator with one fictitious "effective" thermal bath with mean number of photons n_{eff} and coupling rate k_{tot}.

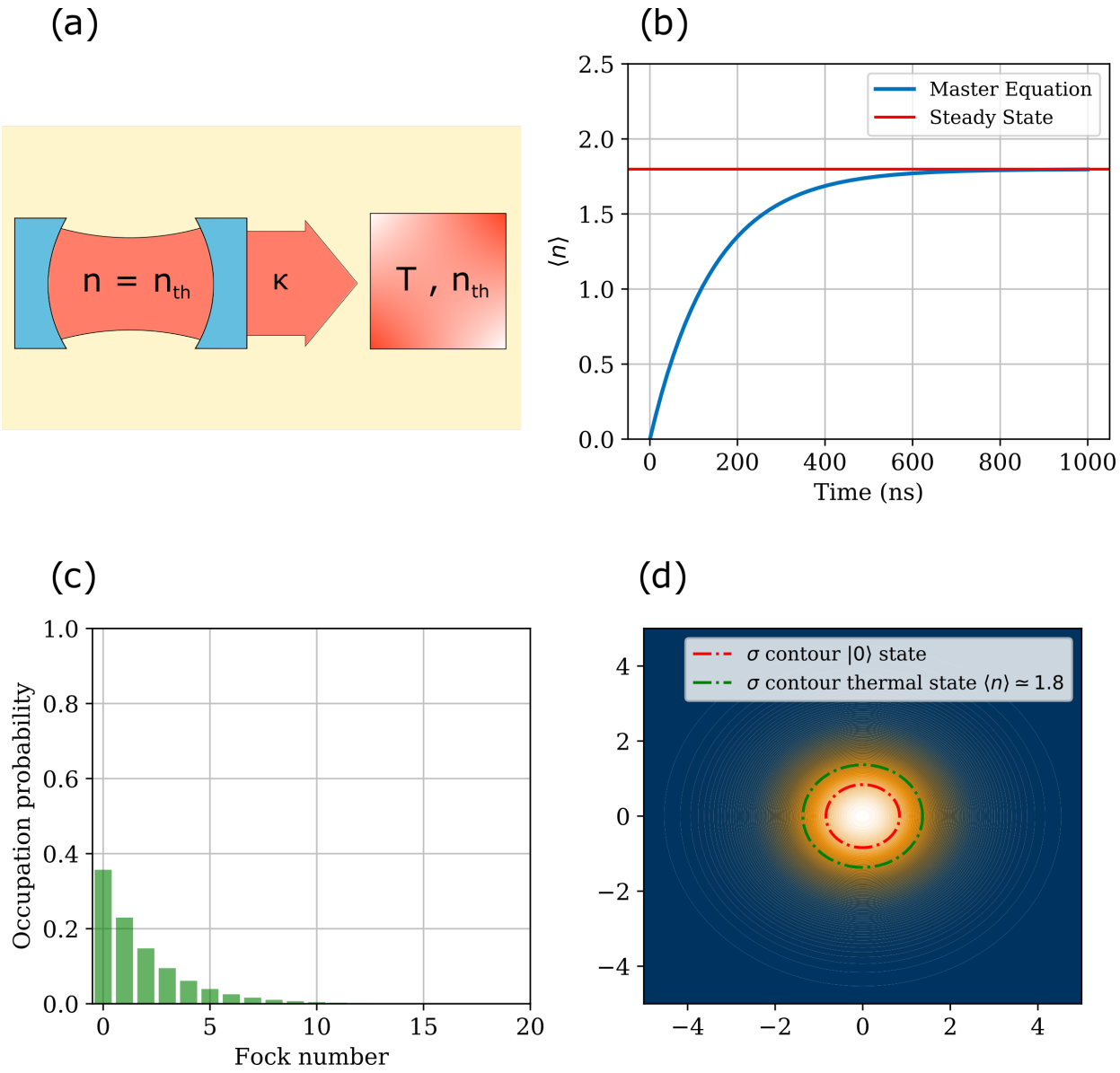

Figure 3.2.1: QuTiP [26] simulation of a resonator coupled to a thermal bath **(a)** Scheme of a one port lossless resonator coupled to the environment, represented by a thermal bath with temperature T and mean number of photons n_{th}. The coupling constant of the resonator κ represents the relaxation rate of the field from the cavity to the bath and vice versa. **(b)** Evolution of the mean number of photons of a cavity coupled to a thermal bath. For long times (i.e. $t >> 1/\kappa$), as described in eq. 3.2.3, the system reaches a steady state in which the mean number of photons in the cavity equals the mean number of photons in the bath. **(c)** Photon number probability distribution of the cavity in the long time limit $t >> 1/\kappa$. As we can see, the probability distribution follows the Planck distribution for black body radiation (see eq. 3.2.4). **(d)** Wigner function representation of the cavity density matrix in the long time limit. As we can see, the phase space distribution represents a thermal state with $\langle n \rangle = n_{th}$.

.

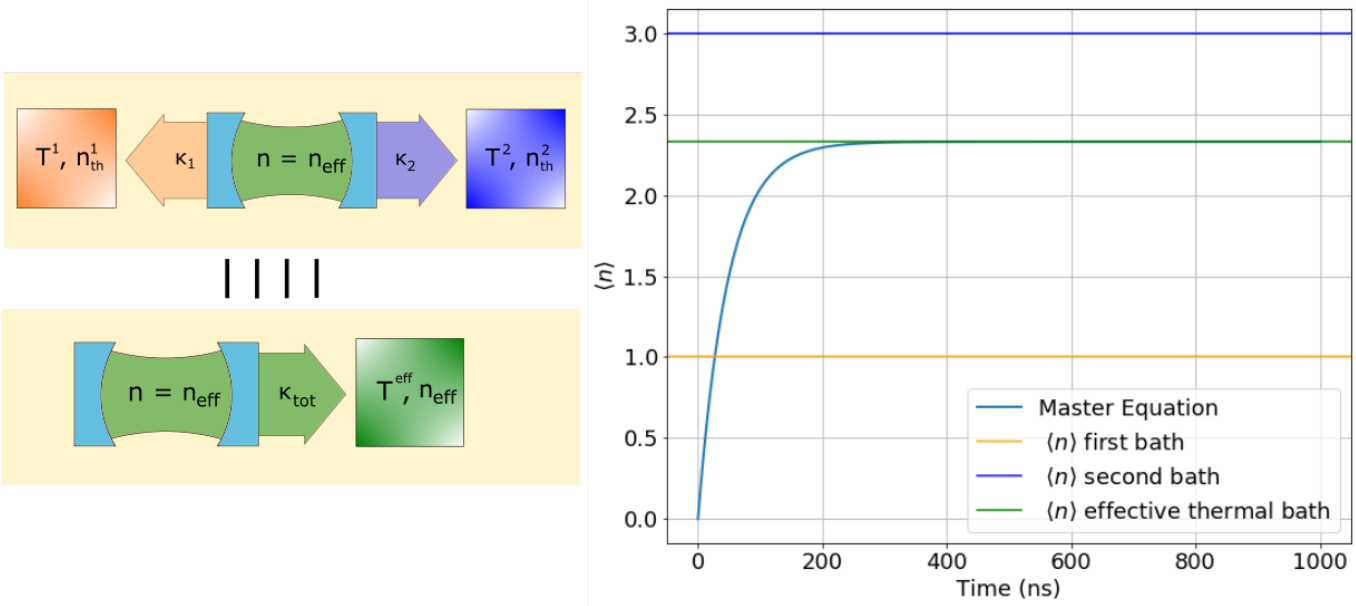

Figure 3.2.2: Scheme of a lossless resonator coupled to two thermal baths and the simulation of the time evolution of the mean number of photons in the resonator. As highlited in equation 3.2.7, the time evolution of a resonator coupled to two different baths with different coupling constants κ_1, κ_2 and different temperatures T^1, T^2 is equivalent to the evolution of a resonator coupled with a coupling constant κ_{tot} to a single bath with an effective temperature T^{eff}. The evolution of the mean number of photons shows that in the long time limit $t >> 1/\kappa_{tot}$ the resonator reaches the thermal equilibrium with an "effective" thermal bath with n_{eff} number of photons.

3.3 Qubit, resonator and the environment - dephasing from thermal noise

In the previous sections we have studied the open quantum system composed of the qubit or the resonator connected to the reservoir by longitudinal (σ_z) or transverse (σ_x) interaction.

Here we will describe what happens when the open quantum system is composed of a "isolated" qubit (i.e. not coupled directly to the environment) but coupled dispersively to the cavity which exchanges energy with the environment.

The Hamilonian of this open system is described by

$$\begin{aligned} H &= H_{sys} + H_{bath} + H_{int}, \\ H_{sys} &= \hbar\omega_c\, a^\dagger a + \frac{1}{2}\left(\omega_q + \frac{\chi}{2} + \chi a^\dagger a\right)\sigma_z, \\ H_{bath} &= \sum_j \hbar\omega_j \left(b_j^\dagger b_j + \frac{1}{2}\right), \\ H_{int} &= \sum_j \hbar\, g_j \left(a^\dagger b_j + b_j^\dagger a\right), \end{aligned}$$

where H_{sys} represents the Hamiltonian of the qubit and cavity coupled in the dispersive regime, H_{bath} is the usual Hamiltonian of the thermal bath described as a large number of harmonic oscillators and H_{int} represents the energy exchanging interaction between the cavity and the thermal bath.

Since the cavity and the qubit in our architecture are coupled longitudinally (see section 2.2.6), it is easy to figure out that an energy dissipating process in a cavity would act as a pure dephasing mechanism to the qubit.

In order to find a quantitative answer, we have to solve the master equation, which for the present case is

$$\begin{aligned} \rho_{sys} &= \rho_{qb} \otimes \rho_{cav}, \\ \dot{\rho}_{sys} &= -\frac{i}{\hbar}\left[H, \rho_{sys}\right] + \frac{1}{2}\kappa(n_{th}+1)\mathcal{D}[a]\rho_{sys} + \frac{1}{2}\kappa\, n_{th}\,\mathcal{D}[a^\dagger]\rho_{sys}. \end{aligned}$$

As we can see, in order to find the solution of the master equation we have to solve the coupled differential equations of the density matrix ρ_{sys} which describes the qubit and the resonator. It is possible to find an analytical solution by expressing the density matrix via Wigner function representation (see [30]) or positive P function representation (see [6]) and then solving the differential equations for the terms coupled to the off-diagonal elements of the qubit density matrix.

From these calculations, the dephasing from thermal noise in the long time limit $1 >> 1/\kappa$ can be written as

$$\Gamma_\phi^{th} = \frac{\kappa}{2}\,\mathrm{Re}\left[\sqrt{\left(1 + \frac{i\,\chi}{\kappa}\right)^2 + \left(\frac{4i\,\chi\, n_{th}}{\kappa}\right)} - 1\right]. \tag{3.3.1}$$

For $n_{th} << 1$ we can expand Γ_ϕ^{th} to first order in n_{th} (see [7] and [8]) and find the

approximate solution for the thermal induced dephasing

$$\Gamma_{\phi}^{th} \simeq \frac{n_{th}\,\kappa\,\chi^2}{\kappa^2+\chi^2}. \tag{3.3.2}$$

As we can see, the thermal dephasing rate Γ_{ϕ}^{th} depends on the mean number of photons in the reservoir n_{th}, the dispersive shift χ and the cavity damping rate κ.

The behavior of the thermal dephasing with respect to the mean number of photons in the cavity is also shown through the simulation of the time evolution of $\langle\sigma_x\rangle$ in fig. 4.3.2. The parameter of the simulation are: $\omega_{qb}/2\pi = 6.8\,\text{GHz}$, $\omega_{cav}/2\pi = 9.2\,\text{GHz}$, $\chi/2\pi = 3.6\,\text{MHz}$ and $\kappa/2\pi = 1.1\,\text{MHz}$.

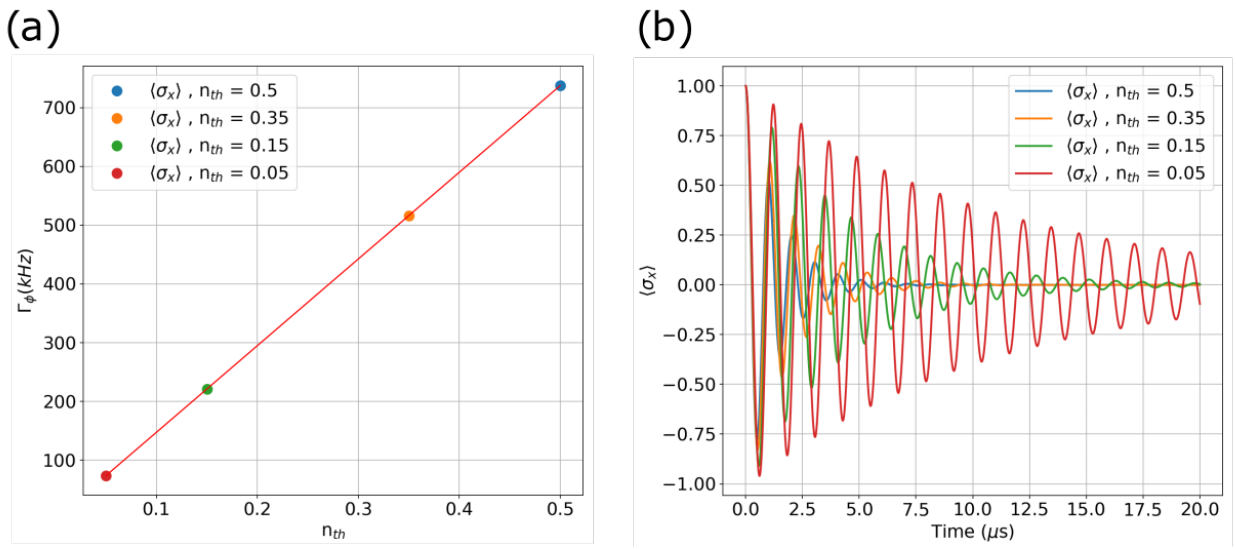

Figure 3.3.1: Simulation of qubit dephasing with respect to different bath temperatures
(a) Qubit dephasing in dependence of the mean number of photons n_{th} of a thermal bath coupled to the readout resonator. The coloured dots represent the dephasing rates extracted by the decay of the $\langle\sigma_x\rangle$ operator carried out by simulation with QuTiP [26]. The red line represents the analytical formula of the dephasing in the low photon number regime described in eq. 3.3.2. **(b)** Time evolution of $\langle\sigma_x\rangle$ in a rotating frame detuned with respect to the qubit frequency of $\delta\omega = 2.5\,\text{MHz}$ for different mean number of photons in the thermal bath coupled to the resonator. We can see that the decay rate increases linearly with respect to n_{th} according to eq. 3.3.2.

As a final remark, we can also figure out what is the form of the thermal dephasing rate when several thermal baths are connected to the readout resonator. In analogy to what we have already seen in 3.2.7, the solution of the master equation (see [6]) leads to the same equation for the thermal dephasing Γ_{ϕ}^{th} seen in eq. 3.3.2 with the exception of changing n_{th} and κ with the new values n_{eff} and κ_{tot} (see eq. 3.2.6 and eq. 3.2.5).

Chapter 4

Thermal noise and attenuators

The first question that we have to ask to ourselves is: why do we care about thermal noise? Which difference do we see in the experiment if we couple our quantum system to a "cold" or "hot" environment?

First of all, as we have seen in section 3.1.1.1 and section 3.2, in the qubit and resonator both the steady state population of the levels depends on the temperature of the environment, and follows a Boltzmann distribution for the qubit and a Bose-Einstein for the resonator.

In other words, if the mean number of photons of the bath n_{th} at the frequency of the quantum system is not zero, the system doesn't settle to the ground state and the population of the system is distributed among the higher energy levels of the system.

The second effect is that an environment with high temperature is characterized with a high loss of information, either through a dephasing channel or through a depolarization channel (see chapter 3).

In the second instance it is important to recall (see section 2.2.6) that one of the main channel of interaction between the Circuit QED architecture and the environment is represented by the microwave lines attached to a system. As we can see from fig. 4.0.1, in the present work of this thesis the microwave lines are divided in two main parts: the *input lines*, from which the input signals used to interact to the Circuit QED are transmitted and the *output lines*, from which the output signals are collected, amplified and finally recorded.

In this chapter it is described how the theory developed about open quantum system and thermal reservoirs (see chapter 3) will be applied to general Circuit QED systems. In the first part the connection between the properties of the reservoir and the characteristics of attenuation/isolation of the microwave lines will be discussed. Afterwards, the effect of the thermal reservoir on the qubits and the cavities will be explained. Following that, the strategies that can be adopted in order to lower the temperature of the reservoir will be outlined.

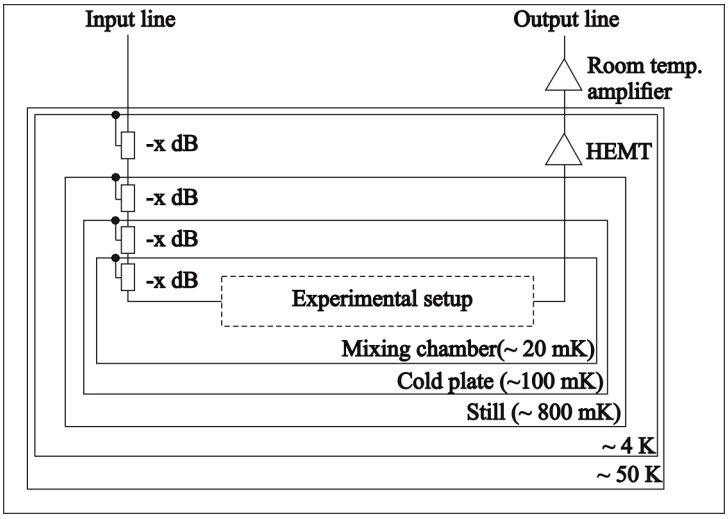

Figure 4.0.1: Schematic diagram describing the wiring of the experimental setup to the Cryostat. As we can see, the microwave lines are divided in two lines: the input line and the output line. The input lines are used to send microwave signals to control the Circuit QED system. The output line is used to collect, amplify and record the microwave signals coming from the Circuit QED system.

4.1 The role of attenuators in the input line

The experiments on qubits and cavities in the framework Circuit QED of are generally performed at temperatures of a few tens of milli-kelvins. This represents a cold environment with respect to the relevant frequency range of the transitions of the quantum system ($k_b\mathrm{T} << \hbar\omega \ \forall\omega \in [4\,\mathrm{GHz},\ 12\,\mathrm{GHz}]$).

However, the temperature of the plate with which the cavity/qubit system is in contact does not represent the only bath our quantum system is coupled to. Indeed, the input and output lines that we use to control and to readout our Circuit QED system represent an additional reservoir which our quantum system is coupled to.

As an example, let's think about an input line that couples the cavity at 20 mK with a 50 Ω resistor at room temperature (see left side of fig. 4.1.1). As we can imagine, if the cavity is not coupled to any other reservoir, the mean number of photons inside the cavity will be the same as the mean number of photons emitted by the resistor; in other words, the temperature of the cavity will come into equilibrium with the temperature of the resistor, which in the present example is room temperature!

More quantitatively, we can describe the voltage noise power spectral density emitted by a resistor R at a temperature T as

$$S_{VV}(\nu, R, T) = 4R\, h\nu\, n_{th}\,(T)$$
$$n_{th}\,(T) = \frac{1}{e^{\frac{h\nu}{k_b T}} - 1}$$

where $n_{th}\,(T)$ is the mean photon number population according to the Bose - Einstein distribution. $n_{th}\,(T)$ is dimensionless and can be thought as photon flux spectral density, i.e as number of photons per Hz frequency interval, per second [31].

This form of voltage noise PSD, which in the classical limit $\hbar\omega << K_bT$ describes the Johnson-Nyquist noise $S_{VV}(\nu, R, T) = 4K_bTR$ is blackbody radiation propagating in a one-dimensional cable [31, 32, 33].

The usual solution to that problem is to install a series of attenuators (see fig. 4.1.1) on the different stages of the cryostat in order to attenuate the amount of thermal photons that interact with our Circuit QED architecture. Of course, each attenuator is by itself a dissipative object which (in the best case scenario) will have the same temperature as the plate of the cryostat to which it is anchored. It will re-emit thermal photons according to that temperature.

The effective voltage noise spectral density seen by the Circuit QED architecture coming of such a cascade system (see [32] , [14]) can be described as

$$S_{VV}(\nu) = \sum_i A^{(i)}\, S_{VV}(\nu, R^{(i)}, T^{(i)}) \tag{4.1.1}$$

where $S_{VV}(\nu, R^{(i)}, T^{(i)})$ is the voltage noise PSD emitted from the resistor $R^{(i)}$ in the i_{th} attenuator with temperature $T^{(i)}$, and $A(i)$ accounts for the collective attenuation after the corresponding thermal source and before reaching the quantum system (see [32]).

The resulting environment seen by the qubit can be described as a reservoir in which the noise photon occupation number $n_{th}^{eff}(\omega)$ and relative effective temperature $T^{eff}(\omega)$

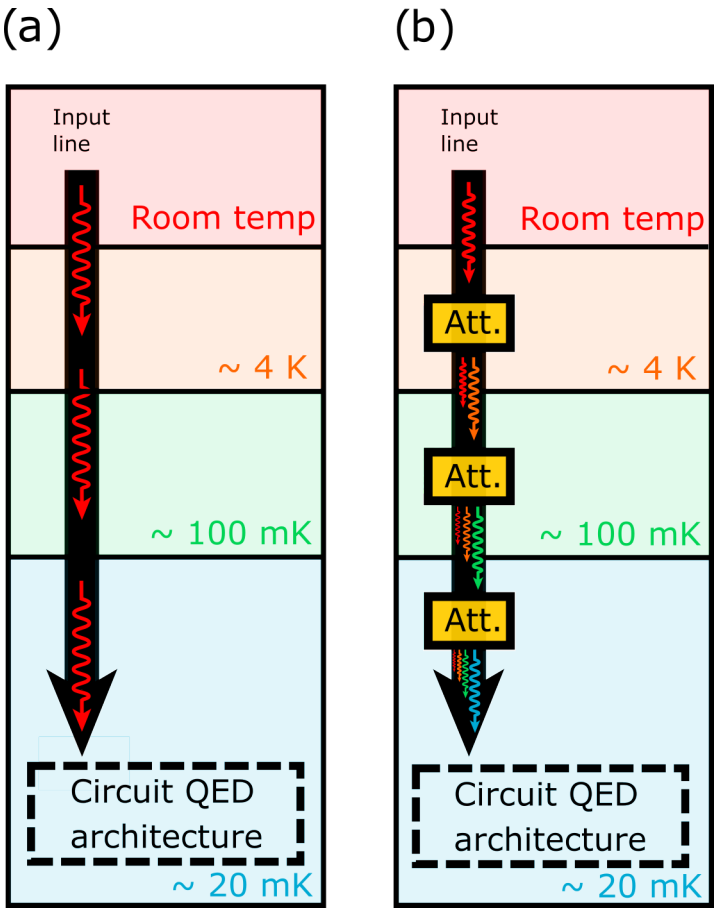

Figure 4.1.1: Thermal noise propagation in the cryostat.
(a) Schematic diagram of thermal noise propagation from room temperature to the circuit QED architecture through the input line. As we can see, the input line creates a *thermal shortcut* that causes the quantum system to be coupled with the blackbody radiation originating at room temperature . **(b)** Schematic diagram of thermal noise propagation through an input line interspersed with attenuators located at stages with different temperature. Each attenuator decreases the amplitude of the blackbody radiation coming from the previous stages while it re-emits blackbody radiation at the temperature of his stage.

can be described as

$$n_{th}^{eff}(\omega) = \sum_i A^{(i)}\, n_{th}\left(T^{(i)}\right) \tag{4.1.2}$$

$$T^{eff}(\omega) = \frac{\hbar\omega}{k_b \ln\left(\frac{1}{n_{th}^{eff}} + 1\right)} \tag{4.1.3}$$

It is important to note that this mixture of thermal noise from different thermal sources gives rise to a reservoir in which the noise photon occupation number distribution is not thermal anymore. This means that the effective temperature of the reservoir changes with respect to the frequency.

4.1.1 Thermal noise from the input line

In the experimental setup used in this thesis, the attenuation chain in the input line (see fig. 6.1.1) presents 20 dB of attenuation on the 4K plate, 10 dB of attenuation on the 100 mK plate and 20 dB of attenuation at the base temperature. Equation 4.1.2 can be written in an expanded form as

$$n_{in}(\omega) = \frac{n_0(T_{300\,K})}{A_1\,A_2\,A_3} + \frac{n_1(T_{4\,K})}{A_2\,A_3} + \frac{n_2(T_{100\,mK})}{A_3} + n_3(T_{20\,mK})\,. \tag{4.1.4}$$

From what we can see, thermal noise components with different temperatures (see panel

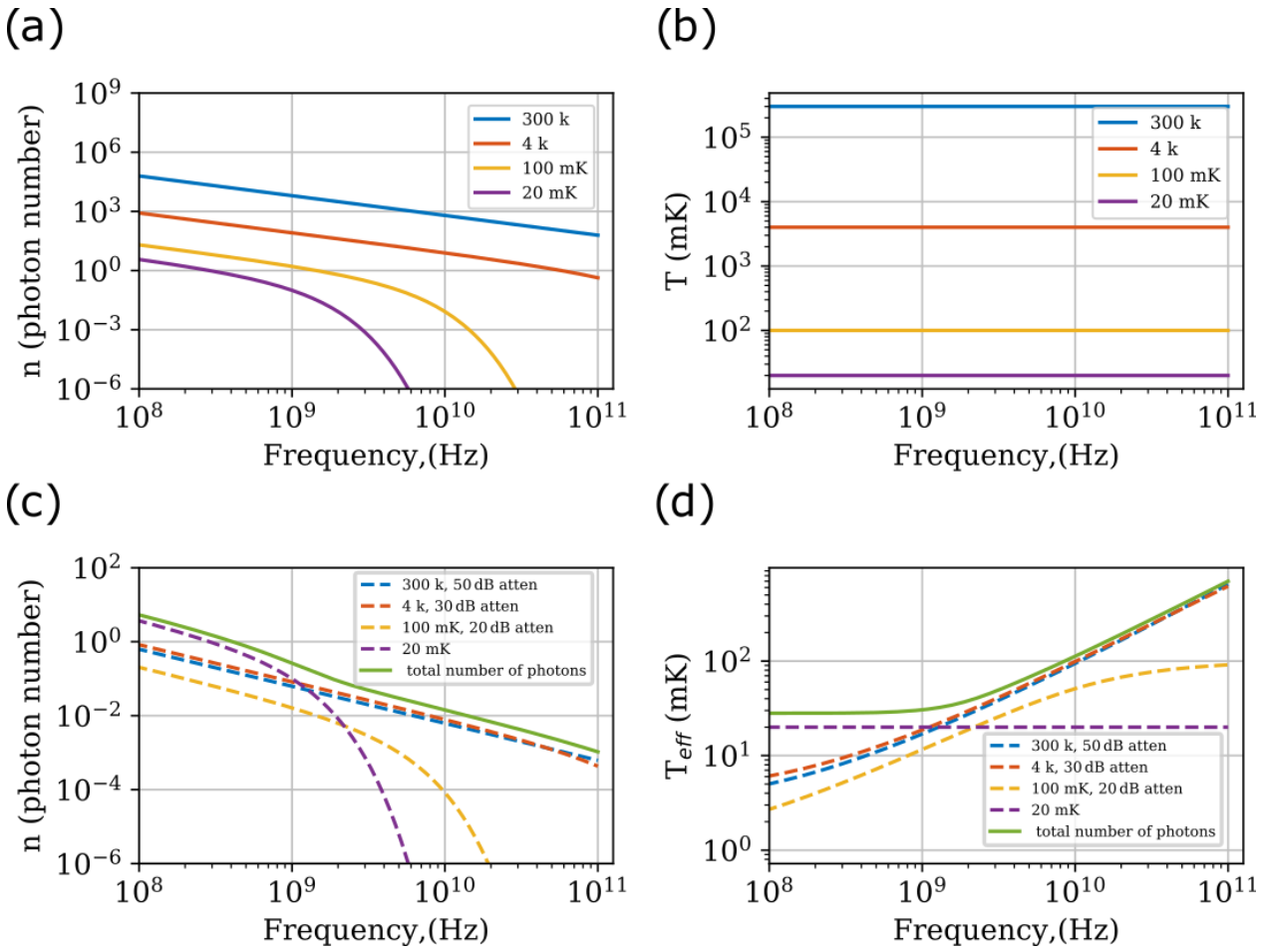

Figure 4.1.2: Blackbody radiation from the input line
(a) Mean photon number distribution for different thermal baths with respect to frequency. As we can see, the mean photon number distribution is described by the Bose Einstein distribution. **(b)** For a mean photon number distribution that follows the Bose Einstein distribution (see panel **a**) there is no temperature dependence with respect to the frequency. **(c)** The photons emitted from each stages (see panel **a**) are attenuated according to equation 4.1.4 and are plotted as dashed lines. The total mean number of photons distribution $n_{in}(\omega)$ is the sum of them (see eq 4.1.4) and is plotted as a green line. **(d)** Temperature dependence of the mean number of photon distribution relative to panel **c**. As we can see, since the photon distribution is not thermal, the effective temperature T_{eff} of the input bath acquires a frequency dependence.

(b) of fig. 4.1.2) and therefore different frequency distributions of the mean number of photons (in amplitude and cutoff, see panel **(a)** of fig. 4.1.2) are mixed together with different weights, where the weights depend on the attenuation chain described above. It is clear that the frequency distribution of the mean number of photons $n_{in}(\omega)$ recovered from eq. 4.1.4 describes the *input bath* coupled to the qubit which is not thermal (see panel **(c)**) of fig. 4.1.2. This has the effect that the effective temperature of the input bath $T_{in}(\omega)$ is frequency dependent (see panel **(d)** of figure 4.1.2).

4.1.2 Thermal noise from the output line

In the experimental setup used in this thesis, the attenuation from the thermal noise coming from the output line (see fig. 6.1.1) is provided by two isolators at the base temperature for a total of 40 dB of isolation. The main source of noise from the output is considered to be the 4 K plate at which the HEMT is sitting on [32] along with a small contribution of the 20 mK radiation coming from the resistors of the 50 Ω loads of the isolators. Equation 4.1.2 can be written as

$$n_{out}(\omega) = \frac{n_1(T_{4\,K})}{I_3} + n_3(T_{20\,mK}), \tag{4.1.5}$$

$$I_3 = 10^4 \tag{4.1.6}$$

where the factor I_3 is given by the 40 dB of isolation provided by the isolators at base temperature.

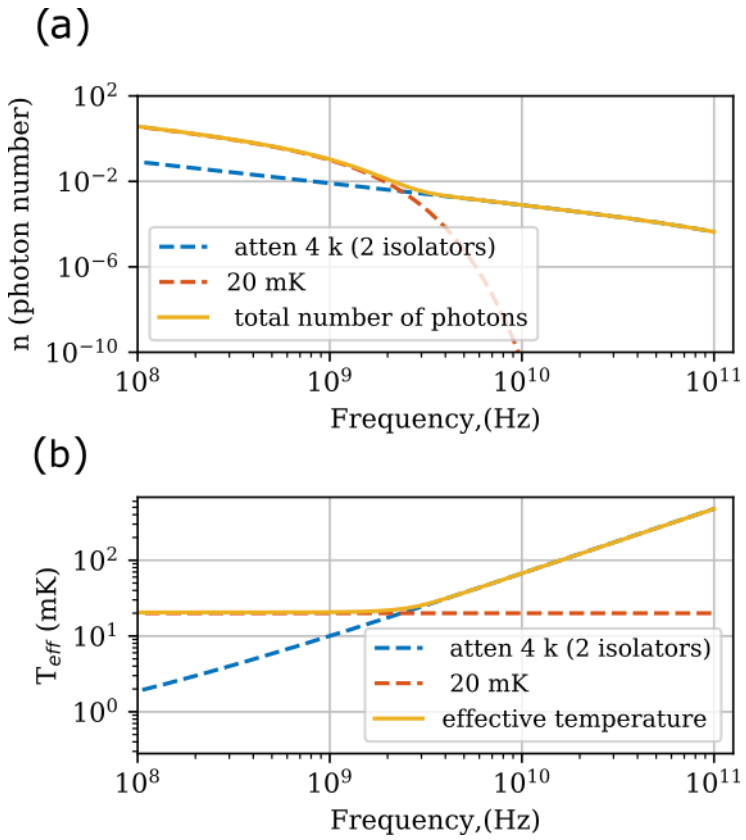

Figure 4.1.3: Blackbody radiation from output line
(a) In this panel we can see the mean number of photons distribution relative to the output bath. According to eq. 4.1.5, the main sources of noise are given by the 4 K plate and by the 20 mK, which are plotted as dashed lines in the graph. The total mean number of photons distribution that describes the output bath $n_{out}(\omega)$ is the sum of them (see eq. 4.1.5) and is plotted as a yellow line. **(b)** Temperature dependence of the photon distributions relative to panel **a**. The yellow line represents the temperature distribution of the output thermal bath with respect to frequency.

The mean number of photons distribution of the output bath $n_{out}(\omega)$ and the relative effective temperature $T_{out}(\omega)$ are plotted respectively in panel **(a)** and **(b)** of fig. 4.1.3.

In a similar way with respect to the previous section, we can see that the mean number of photons distribution $n_{out}(\omega)$ which describes the *output bath* coupled to the qubit is not thermal (see panel **(a)** of fig. 4.1.3, with the effect that the effective temperature of the output bath $T_{out}(\omega)$ is frequency dependent (see panel **(b)** of figure 4.1.3)

4.1.3 Effective thermal noise for qubits and cavities

In the previous sections we have calculated the distribution for the mean number of photons for the input and output bath. Moreover, in the previous chapter we have seen how our quantum system (qubit, resonator, qubit and resonator in dispersive regime) is affected by the presence of a thermal bath by solving the master equation of the open quantum system.

We have also seen (see 3.2) that if the quantum system is coupled with multiple baths, we can very conveniently use the same solution of the single bath problem, just defining an effective thermal bath in which the coupling rates and the mean number of photons are modified (see equations 3.2.5, 3.2.6).

In this section, we will provide an example of how to use the concept of the effective thermal bath in order to calculate the qubit and resonator temperature if we have a qubit (or resonator) connected to an input bath, an output bath and a bath connected to the internal losses of the quantum system.

Applying eq.3.2.6 the mean number of photons impinging on the cavity is given by

$$n_{eff}(\omega_c) = \frac{n_{in}(\omega_c)\cdot\kappa_{in} + n_{out}(\omega_c)\cdot\kappa_{out} + n_{loss}(T\omega_c)\cdot\kappa_{loss}}{\kappa_{in}+\kappa_{out}+\kappa_{loss}}. \tag{4.1.7}$$

As we have already seen, the effective number of photon is nothing else than a weighted mean of the number of photons of the multiple baths calculated at the cavity frequency, and the weights are represented by the decay rates of the cavity through the baths.

In the same way, we can calculate the mean number of photons relative to reservoir coupled to the qubit

$$n_{eff}(\omega_{qb}) = \frac{n_{in}(\omega_{qb})\cdot\gamma_{in} + n_{out}(\omega_{qb})\cdot\gamma_{out} + n_{loss}(\omega_{qb})\cdot\gamma_{loss}}{\gamma_{in}+\gamma_{out}+\gamma_{loss}}. \tag{4.1.8}$$

In our specific case, the qubit is coupled to the input and output bath through the readout resonator. The decay rates are represented then by the very well known *Purcell factor* [34]:

$$\gamma_{in} = \frac{g^2}{\Delta^2}\kappa_{in},$$
$$\gamma_{out} = \frac{g^2}{\Delta^2}\kappa_{out}.$$

As a reminder, the link between the effective number of photons at the qubit frequency $n_{eff}(\omega_{qb})$ and the temperature of the qubit (for a 2 level system approximation) described

through the populations of the level in the steady state (see 3.1.1) is

$$T_{eff} = \frac{\hbar\omega_{qb}}{k_b \ln\left(1/n_{eff}(\omega_{qb}) + 1\right)} \tag{4.1.9}$$

$$\frac{\rho_{11}}{\rho_{00}} = \exp\left\{-\frac{\hbar\omega_{qb}}{k_b T_{eff}}\right\} \tag{4.1.10}$$

$$\rho_{11} = \frac{1}{1 + \exp\left\{+\frac{\hbar\omega_{qb}}{k_b T_{eff}}\right\}} \tag{4.1.11}$$

while the link between the effective number of photons at the cavity frequency $n_{eff}(\omega_c)$ and the dephasing of the qubit (see 3.3.2) is

$$\Gamma_\phi^{th} \simeq \frac{n_{eff}(\omega_c)\,\kappa_{tot}\,\chi^2}{\kappa^2 + \chi^2} \tag{4.1.12}$$

4.2 The role of lossless filters in the line

As we have seen in the previous sections, the insertion of a chain of attenuators between a thermal bath and the Circuit QED architecture modifies the temperature of the bath seen by the quantum system.

On the contrary, the insertion of a chain of lossless microwave filters between the Circuit QED architecture and the bath does not change the temperature of the bath, but modifies the *rate* with which the quantum system interacts with the bath.

Let's imagine for example one lossless cavity with frequency ω_{cav} coupled with a rate κ_{old} to a thermal bath with mean number of photons n_{bath}. As we have already seen in section 3.2, in the long time limit the mean number of photons in the resonator will be equal to n_{bath}, and the time evolution of the system will develop at a rate κ_{old}.

If we insert a reflective element between the cavity and the bath, the steady state solution of the system will not change, but the rate at which the system will evolve into the steady state will change as (see [35])

$$\kappa_{new} = \kappa_{old}\left|S_{21}\left(\omega_{cav}\right)\right|^2 \tag{4.2.1}$$

where κ_{new} is the new coupling rate of the system, κ_{old} is the coupling rate between system and bath without the reflective element, $|S_{21}(\omega_{cav})|$ is the absolute value of the scattering parameter that describes the power transmission between the Circuit QED architecture and the bath, due to the insertion of the reflective element. As a result, the microwave lossless filters can be used to modify the coupling of the quantum system to the bath, but not to modify the *temperature* of the bath.

4.3 Changing the temperature of the effective thermal bath

The objective of this thesis is to characterize the thermal noise of the reservoir at the cavity frequency, which is considered to be the major source of dephasing for the transmon qubit. It is natural to think about which kind of strategies can be adopted in order to minimize the magnitude of this source of noise. We have already seen in eq. 4.1.7 that the mean number of photons of the effective reservoir is the weighted mean of the input bath, the output bath and the bath relative to the internal losses, whereas the weights are represented by the couplings between the cavity and those baths. Moreover, following the calculation of the input and output thermal baths (see eq. 4.1.4 and eq. 4.1.5) we have seen that the temperature of these reservoirs depend on the amount of attenuation/isolation in the lines. Following these considerations, it is clear that in order to minimize $n_{eff}(\omega_c)$ two strategies can be adopted.

From one side, we can try to minimize the mean number of photons from the different baths, for example by increasing the attenuation in the attenuation chain described in the previous section. Unfortunately, implementing this type of solution is usually very hard.The reason behind that is that the effectiveness of the attenuation chain depends on the *thermalization* properties of the attenuators: if the attenuators are not able to dump the hot microwave photons into the cold cryostat plate, they will inevitably warm up and become a source of hot photons too. Actually, several articles pointed out that the thermalization properties of the cryogenic attenuators are very poor at mK temperatures [7] and that the temperature of those objects is strongly dependent on the amount of power that they are required to attenuate [9] (for example, some commercial attenuators heat up to $\simeq 100\,\text{mK}$ by dissipating $\simeq 10\,\text{nW}$ of power). In order to work in that direction it is very important to use special attenuators with remarkable attenuation properties. Two great examples are represented by the "Hot electron heatsinks" microwave attenuators (see [36] and [9]) and the cavity attenuators (see [7]). In the next subsection the general characteristics of the cavity attenuators will be presented.

From the other side, we can try to minimize $n_{eff}(\omega_c)$ by choosing carefully the coupling between the cavity and the different baths. In fact, if we attach a very cold bath to the cavity, and we maximize the coupling of the qubit to that bath, the mean number of photons of the effective thermal bath would move towards the value of the cold bath. Physically, that means that we would cool the cavity by giving to the cavity the chance to "dump" the hot photons to a cold reservoir. In this thesis the second strategy is adopted since the output bath seems to be much colder of the input bath. In order to fine tuning the coupling between the quantum system and the input bath some lossless reflective element are inserted between the quantum system and the input bath, according to eq. 4.2.1.

In the next subsection the engineering of such reflective elements (waveguide section, composition of waveguide section and cavity attenuator) will be presented.

4.3.1 Cavity attenuators

As we have already described, the engineering of a source of attenuation able to thermalize at mK temperature is an outgoing challenge in the field of Circuit QED.

The thermalization problem comes from the fact that the resistors in the attenuators

dump the dissipated power to the cold cryostat plate through the electron-phonon interaction and phonon-phonon transport [37] [38]. The problem is now that very few phonons are present at millikelvin temperatures.

Using the same language of the previous chapter, at millikelvin temperatures the commercial resistor are more and more decoupled to the "cold" environment represented by the cryosat plate and more coupled with the "hot" reservoir represented by the previous stages of the cryostat, with the effect of having a resistor hotter than the cryostat plate.

One solution to this problem is to find a source of dissipation which would present an efficient coupling with the cold bath (i.e. the cryostat plate) at mK temperature. One good attempt in this direction is represented by cavity attenuators [7]. Those object are *undercoupled* (i.e. the major source of loss is represented by the *internal* losses) 3D waveguide cavities made of metals with good thermalization characteristics, like copper or brass. Actually, the power sent to those objects is dissipated into the cavity walls, and the resulting heat is transported into the bulk metal means electrons in a Fermi degenerate system, since electronic excitations are always present at low temperatures [7].

One example of a home-made cavity attenuator can be found in fig. 4.3.1. Taking a

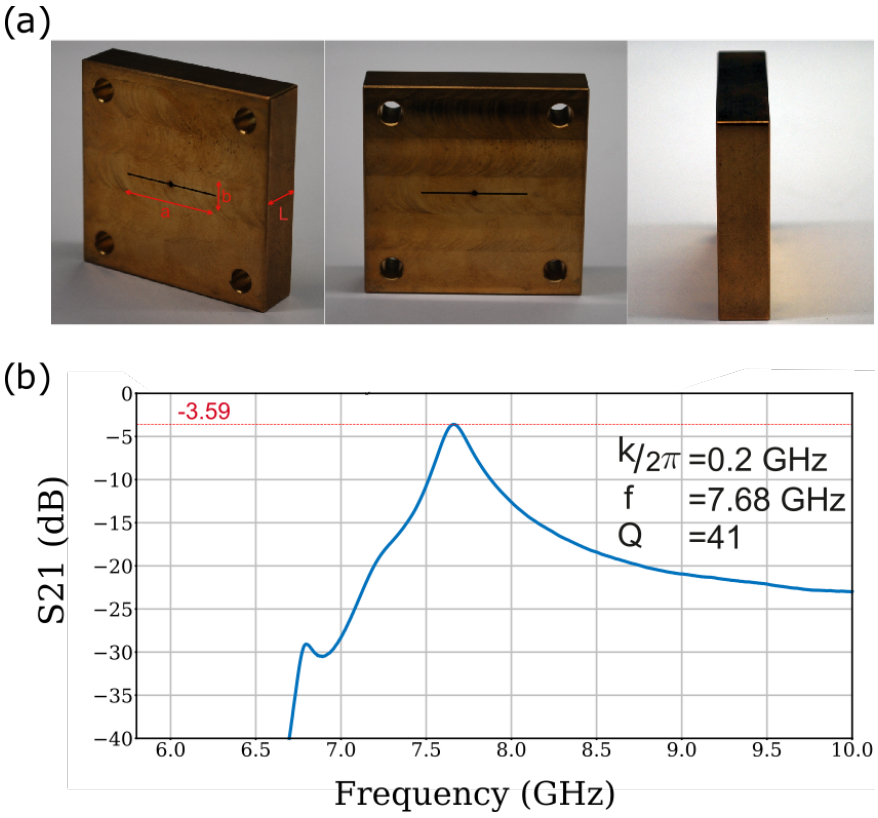

Figure 4.3.1: **(a)** Pictures of a cavity attenuator made of brass with internal dimensions $a = 19.76\,\text{mm}$, $b = 0.24\,\text{mm}$, $L = 10\,\text{mm}$. The "flat" profile of the cavity ($b << L < a$) secures an high surface to volume ratio in order to maximize the resonator losses and turns the cavity into a dissipative element. **(b)** Transmission profile of a cavity attenuator in series with a 3D waveguide. We can see the cutoff drop of the 3D waveguide at $\simeq 6.6\,\text{GHz}$ as well as the cavity attenuator fundamental mode at $\simeq 7.7\,\text{GHz}$. As a result of the dissipation, the peak appears to be wide, with a $k/2\pi = 0.2\,\text{GHz}$ and a $Q_{tot} = 41$. The attenuation of $-3.6\,\text{dB}$ due to energy dissipation can be seen from the on-resonance power transmission.

look of fig. 4.3.1 it can be tricky to understand why the cavity attenuator behaves like a cavity instead of a waveguide. Some insight of the working principle of cavity attenuators can be found by analizying the concept of impedance in 3D waveguides. Following Pozar [14] let us at first recall the well known formulas for the cutoff frequency ν_c and the propagation constant β for 3D waveguides:

$$\nu_c = \frac{c}{2\pi}\sqrt{\left(\frac{m\pi}{a^2}\right)^2 + \left(\frac{n\pi}{b^2}\right)^2}, \tag{4.3.1}$$

$$\beta(\nu) = \frac{c}{2\pi}\sqrt{\nu^2 - \nu_c^2}, \tag{4.3.2}$$

where a, b represent the internal dimensions of the waveguide (see fig 4.3.2), and m-n represent integer numbers relative to the different propagating modes of the waveguide.

From these equations we can derive two more important parameters, the waveguide impedance Z_w and the impedance of the waveguide port $Z_{waveport}$ as

$$Z_w(\nu) = \frac{\eta k}{\beta(\nu)}, \tag{4.3.3}$$

$$Z_{waveport}(\nu) \simeq \frac{Z_w(\nu)}{ab}, \tag{4.3.4}$$

where η is the impedance of the vacuum ($\simeq 377\,\Omega$) and k is the wave vector relative to the propagating mode of the waveguide. Taking a look at picture 4.3.2 we can figure out the difference between a 3D waveguide and the cavity attenuator: since the cavity attenuator has a smaller height with respect to the waveguide, the *waveport impedances* are very different even if the *waveguide impedance* between the two objects have similar values.

Consequently the high impedance values of the ports of the cavity attenuators ensures a impedance mismatch between the cavity attenuator and the input and output line, with the effect of confining the field inside the object. In other words, the high impedance of the ports has the same role of the semi-reflective mirrors of the optical cavities.

In order to prove if the intuition of the working principle of those objects is correct, a lumped-element simulation combined with an HFSS simulation and a room temperature measurement is performed (see fig 4.3.2). The agreement with the predicted results and the lumped element model seems to confirm the intuition about the physical properties of the system.

As final remarks on the cavity attenuators, we can say that those objects (fig 4.3.1) have the advantage of being well thermalized *dissipative* objects, but have the main drawback to have a limited bandwidth ($\simeq 200\,\mathrm{MHz}$).

Moreover, since the amount of attenuation of this object depends on the surface to volume ratio, if we want to increase the attenuation we have to be able to produce cavities with low heights (i.e. $0.1\,\mathrm{mm}$ for $\simeq 10\,\mathrm{dB}$ of attenuation) which is difficult in fabrication.

4.3.2 Broadband reflective cavity attenuators

As we have described in the previous section, cavity attenuators have the advantage to be *dissipative cold* objects, but their limited bandwidth can cause some difficulties in their implementation with complex architectures.

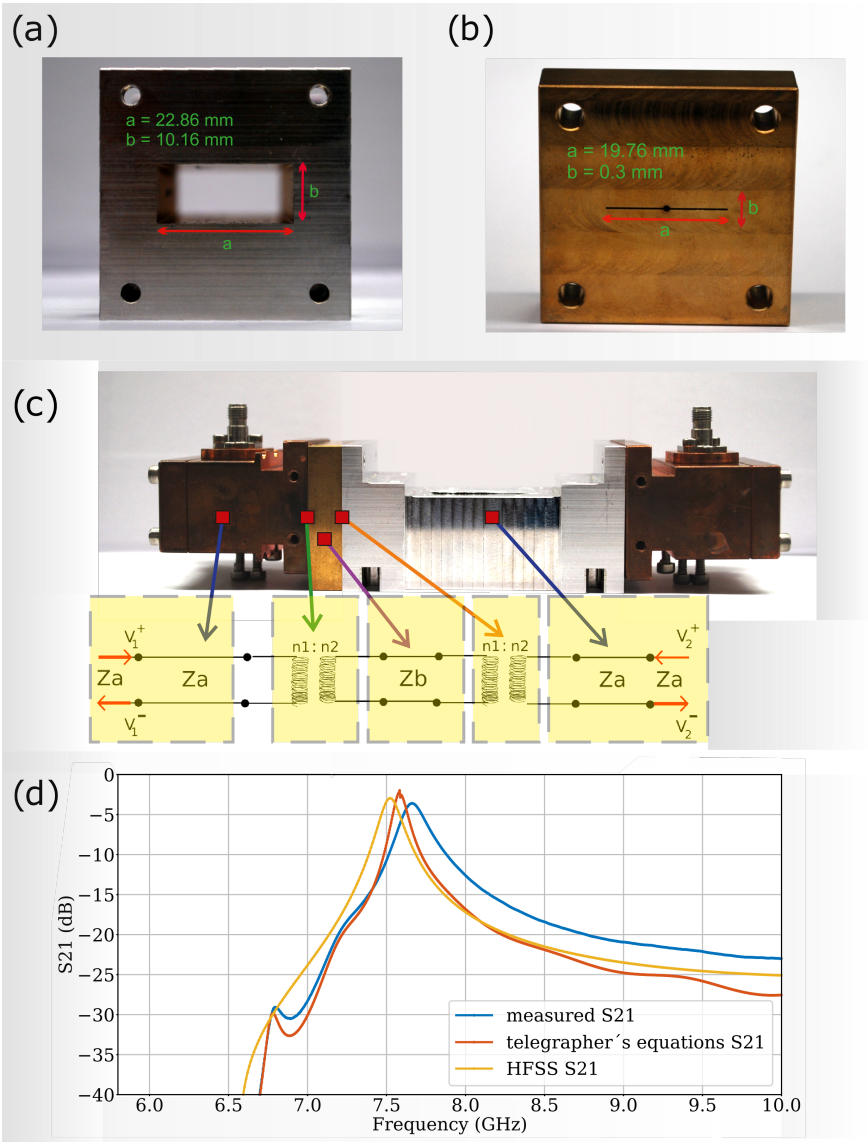

Figure 4.3.2: Measurement and simulation of the cavity attenuator.
(a) Front picture of the 3D waveguide used in the setup of panel **c**. **(b)** Front picture of cavity attenuator used in the setup of panel **c**. **(c)** Picture and lumped element model of a cavity attenuator coupled to a 3D waveguide. The cavity attenuator and the waveguide are represented as sections of transmission line with characteristic impedance Z_a, Z_b calculated through equation 4.3.3. The key idea of the model is to describe the coupling of the cavity attenuator and the waveguide through the impedance mismatch of their waveports impedances (see eq. 4.3.4), represented in the model as ideal transformers. **(d)** Transmission profile (S_{21}) of the setup described in panel **c**. The different curves represent the measured data (blue curve), and the simulations carried out with HFSS [16] (yellow line) and by using the telegrapher equations according to the lumped elements model of panel **c** (red curve). The qualitative agreements between the curves points out that the interpretation on the working principle of the cavity attenuator is appropriate.

Following what we have said in the previous section, the other method to modify the effective temperature of the reservoir coupled to our quantum system is to lower the coupling of the quantum system to the hotter bath. In the present thesis (see fig. 4.1.2

and fig. 4.1.3) the hotter bath is believed to be the input bath, and the quantum system is represented by the readout resonator.

In order to fine tuning the coupling of the readout resonator and the input bath, I have engineered a lossless microwave filter (see eq. 4.2.1) by modifying the design of the cavity attenuator. This object, which has the characteristics of being *broadband* and *lossless*, is called Broadband Reflective Cavity Attenuator (BRCA, see fig. 4.3.3) and attenuates the incoming signal by reflection instead of by dissipation.

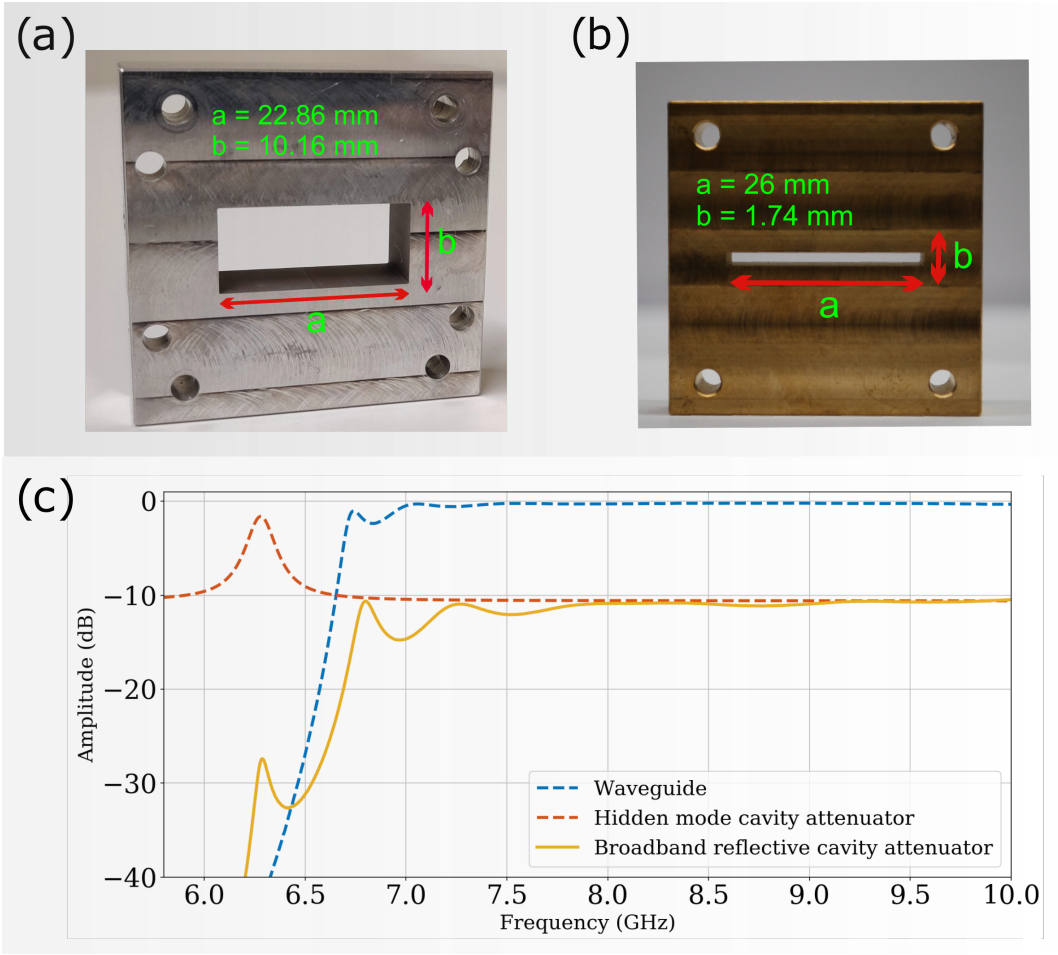

Figure 4.3.3: Assembling the broadband reflective cavity attenuator (BRCA). **(a)** Section of a WR90 waveguide used to assemble the BRCA. The purpose of the waveguide section is to exponentially suppress the mode of the cavity attenuator that results to be *below* the cutoff. **(b)** Cavity attenuator used to assemble the BRCA. The purpose of the cavity attenuator is to attenuate by reflection the signal *above* the cutoff thanks to the "tail" of the resonance. **(c)** Transmission profile of waveguide (dashed blue line, measured data), cavity attenuator (dashed red line, simulated data) and BRCA (yellow line, measured data). The overall transmission profile of the BRCA in the working region (7 GHz to 10 GHz) results to be flat and has the desired amount of attenuation of about $\simeq -10$ dB.

As we have already seen, the main advantage of this object is represented by his broad bandwidth ($\simeq 200$ MHz in the cavity attenuator, $\simeq 3$ GHz in the BRCA) but the drawback is that since the attenuation is provided by reflection, no real dissipation occours, meaning that the change of temperature of the effective thermal bath coupled to our quantum

system depends on which bath (i.e. the “hot” reservoir or the “cold” reservoir) are we acting in order to decrease the coupling. For instance, if we would apply this object to the “cold” bath of our collection of multiple baths attached to the resonator, we would have the effect of increasing the temperature of the effective thermal bath.

Chapter 5

Experimental techniques

In this chapter we can find the description of the techniques used to measure and manipulate the qubit and the readout resonator.

5.1 Pulse generation

We have already seen in section 2.1.2 and section 2.2.3 that in order to manipulate the state of the qubit we use microwave pulses. The general scheme of the pulse generation can be seen in fig. 5.1.1.

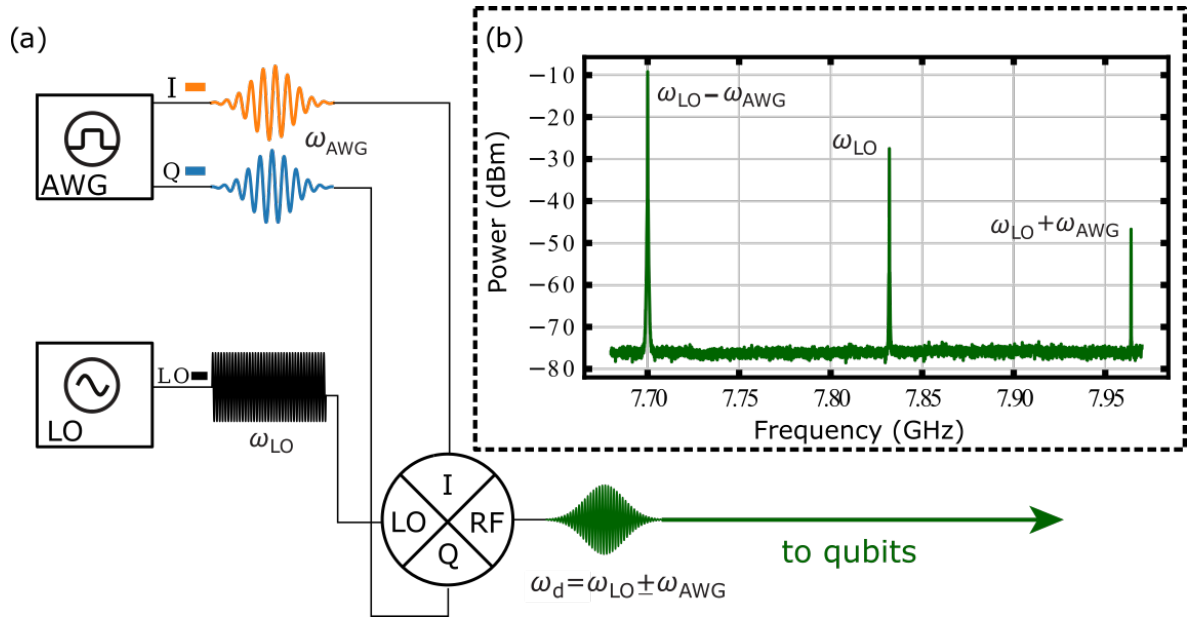

Figure 5.1.1: Setup and spectrum of the qubit drive.
(a) Schematic diagram of the experimental apparatus used to produce the microwave pulse for driving the qubit. **(b)** Frequency spectrum of the drive from the uncalibrated IQ mixer. Usually, one of the sidebands of the microwave pulse is used to drive the qubit, while the LO leakage and the other sideband are minimized through IQ mixer calibration and additional filtering.

An Arbitrary Wave Generator (AWG) is used to produce a signal with a gaussian envelope modulated with a low frequency component ($\omega_{AWG} \simeq$ MHz). As we can see from

panel **b** of figure 5.1.1, the upmixed signal presents three main frequency components: ω_d (LO leakage) , $\omega_d + \omega_{LO}$ (parasitic sideband) and $\omega_d - \omega_{LO}$ (qubit drive). The amplitude of the LO leakage and the parasitic sideband can be minimized through the mixer calibration procedures. The resulting signal, used to drive qubit transitions, is a gaussian microwave pulse with frequency $\omega_d = \omega_{LO} \pm \omega_{AWG}$.

It is important to note that since the envelope of the pulse is gaussian, the spectral shape of the sidbebands produced in the upmixing process will be gaussian too. The relation between the sigma of the gaussians in time and frequency domain is

$$\sigma_\nu = \frac{1}{2\pi\sigma_t}. \tag{5.1.1}$$

Since the transmon qubit is a weakly harmonic oscillator we have to pay attention to the FWHM of the pulse, in order to be sure to not have leakage errors (i.e. to drive some population of the qubit into higher levels out of the computational subspace).

In the present thesis we have used at minimum pulse lengths around $P_l \simeq 100$ ns with a sigma of the pulse equal to $\sigma_t = P_l/6$. Using equation 5.1.1 we find $\sigma_\nu \simeq 10\,\text{MHz}$, meaning that the transition between the e to f state (taking in to account the anharmonicity of $\alpha \simeq 300\,\text{MHz}$) is far away from the spectral components of the gaussian pulse. ($\simeq 30\,\sigma_\nu$ distance.

5.2 Heterodyne detection

The ability to read the state of the qubit is a fundamental ability required in order to perform qubit experiments. As we have already seen in section 2.2.6, in the dispersive regime the resonant frequency of the readout resonator is dependent on the state of the qubit. Moreover, we have also seen that this frequency shift can be mapped trough transmission (S_{21}) measurement, in which the amplitude and phase of the resonator contains information about the state of the qubit (see fig. 2.2.6).

The general scheme used in order to extract the qubit state information from the transmission measurement of the readout resonator can be found in fig. 5.2.1.

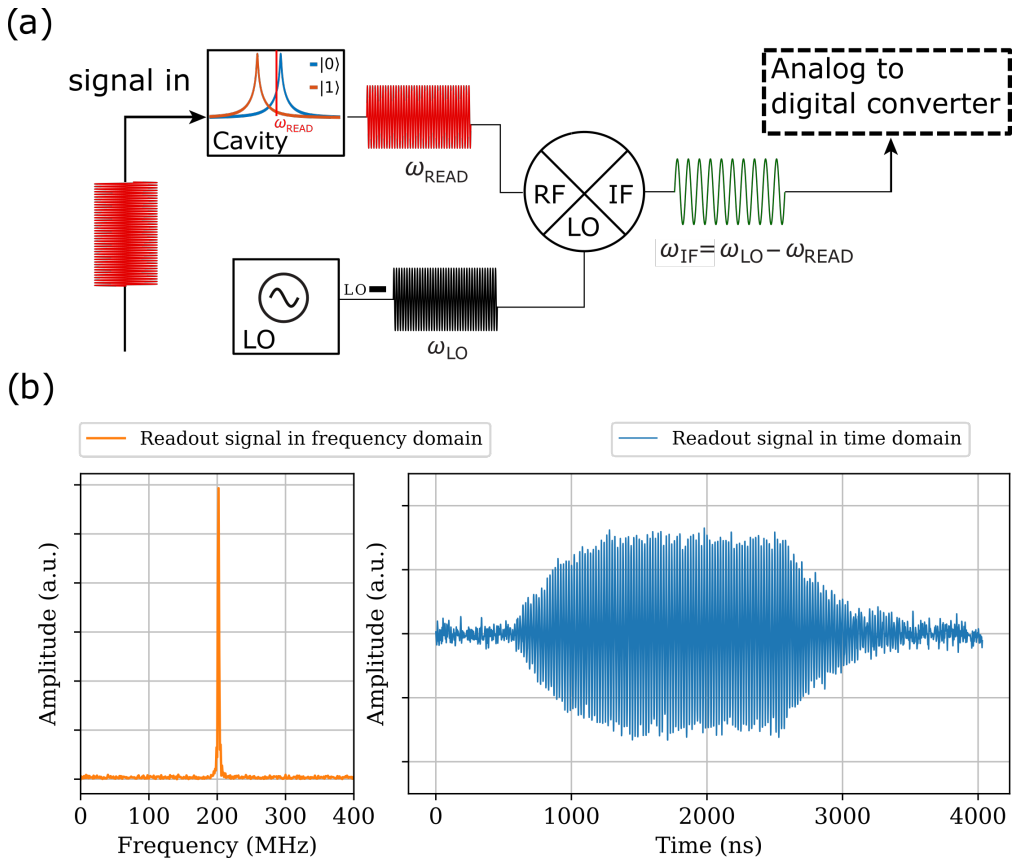

Figure 5.2.1: Heterodyne detection of the readout signal
(a) Schematic diagram of the experimental apparatus used to demodulate the readout signal. A readout pulse with frequency ω_{read} is shined on the readout cavity. As we have already seen in fig. 2.2.6, the readout signal acquires an amplitude/phase dependency with respect to the qubit state. The signal is then downmixed with a 3 port mixer into a low frequency pulse ω_{IF} and sent to an analog to digital converter. **(b)** Digitized signal in frequency and time domain. As we can see, the time domain trace of the downmixed signal (blue line) exibits the characteristics charge/decay times of an LC resonator on top of the ω_{IF} microwave pulse. The frequency domain of the signal (orange line) shows a high signal to noise ratio typical of the heterodyne detection.

As final remarks, is interesting to note two facts. First of all, for the sake of simplicity just the amplitude information of the readout pulse is extracted in order to obtain the information about the qubit state.

In the second instance, it is interesting to note that since the readout pulse is detected through a *Heterodyne* detection scheme (i.e. the readout pulse ω_{READ} is not downmixed to a DC signal, but to a low frequency pulse ω_{IF}) the downmixed signal presents low noise (with respect to the DC noise).As a matter of principle multiple readout resonators at different frequency could be interrogated with a single pulse containing multiple frequency components (see frequency multiplexing in [1]).

5.3 Qubit spectroscopy

The qubit spectroscopy measurements consist of applying microwave radiation at different frequency to the qubit in order to investigate its internal energy structure. The main parameter extracted through qubit spectroscopy is the frequency of the qubit ω_{ge} and the anharmonicity α (see fig. 5.3.1).

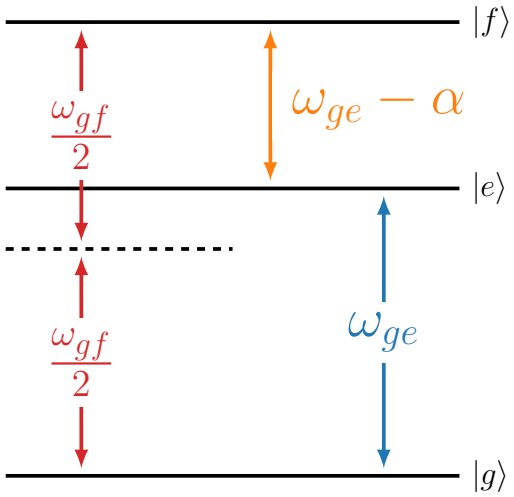

Figure 5.3.1: Schematic diagram of the first three energy levesl of the transmon qubit. The first two energy levels ($|g\rangle$, $|e\rangle$) with energy difference ω_{ge} represent the computational space of the qubit. The energy difference between the $|e\rangle$ and $|f\rangle$ level is equal to the difference between the qubit frequency ω_{ge} and the anharmonicity α. $\omega_{gf}/2$ represents the frequency of the two photon transition used to drive the qubit from the $|g\rangle$ state to the $|f\rangle$ state.

Qubit spectroscopy is performed by sending a long *saturation* pulse (see fig 5.3.2) to the qubit followed by a readout pulse in resonance with the readout resonator. The sequence is repeated by changing the frequency of the saturation pulse: when the probe pulse becomes resonant with the two photon transition $\omega_{gf}/2$ or single photon transition ω_{ge} the qubit is excited. This then causes a shift of the readout resonator peak which result in as a reduction of the transmission amplitude of the readout pulse.

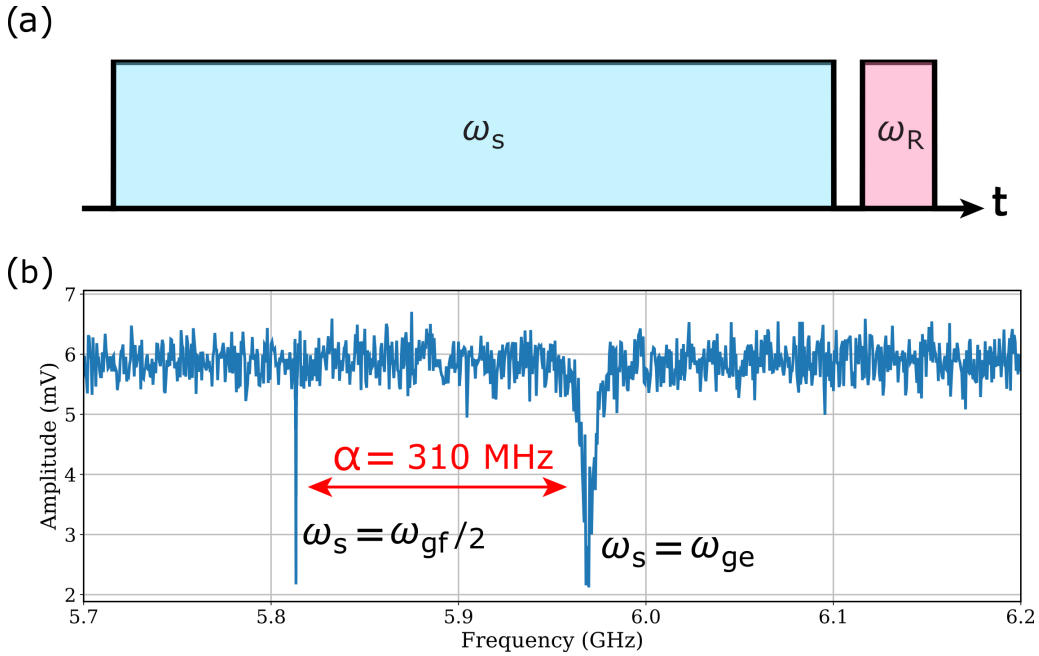

Figure 5.3.2: Qubit spectroscopy
(a) Pulse sequence used to perform spectroscopy on the qubit. The pulse sequence is composed of a long *saturation* pulse with variable frequency ω_s applied to the qubit (light blue pulse) followed by a readout pulse with frequency ω_R applied to the cavity (light pink pulse). **(b)** Spectrum of the qubit. In this plot we can see the transitions with respect to to the first three energy levels of the qubit (see fig. 5.3.1). The two photon transition from $|g\rangle$ to $|f\rangle$ appears as a sharp peak at frequency ω_p while the $|g\rangle$ to $|e\rangle$ transition appears as the power broadened peak at frequency ω_q.

5.4 Cavity spectroscopy

As we have seen in figure 2.2.6, the readout presents different frequency profiles with respect to the qubit state. In order to measure the dispersive shift χ (see section 2.2.6) and the coupling rate κ (see section 2.2.4) we perform a *cavity spectroscopy* measurement. The pulse sequence along with a cavity spectroscopy measurement can be found in fig-5.4.1.

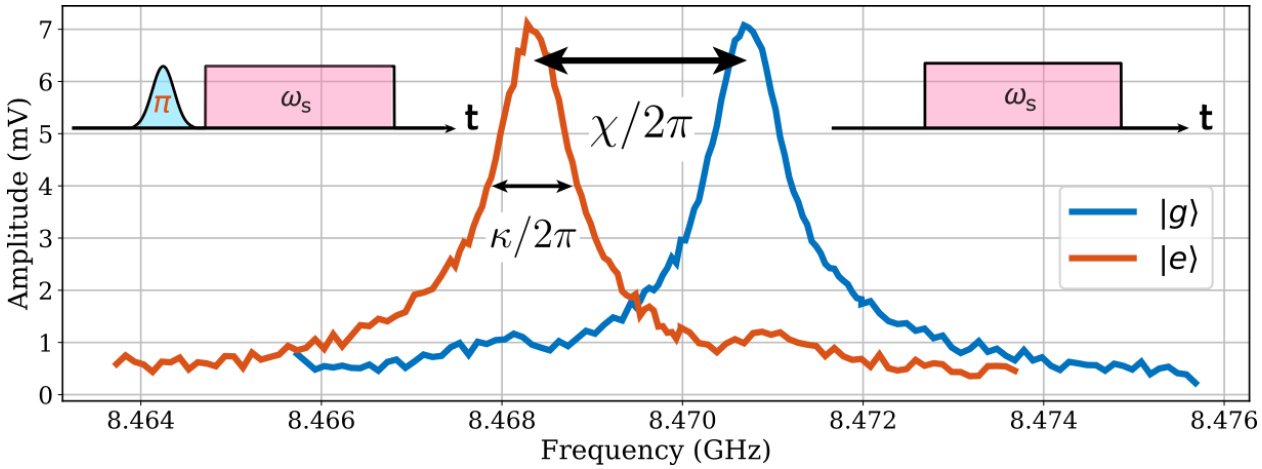

Figure 5.4.1: Cavity spectroscopy
In the figure above we can see the transmission profile of the readout resonator with respect to the qubit in the ground state (blue line) or in the excited state (orange line) along with the respective pulse sequences. The blue trace is recorded by sweeping the frequency ω_s of the readout pulse applied to the cavity (light pink pulse). The orange trace is recorded by first exciting the qubit with a gaussian π pulse (light blue pulse) and then by sweeping the frequency ω_s of the readout pulse applied to the cavity (light pink pulse).

5.5 Rabi measurement

We have already seen in section 2.1.2 that in order to manipulate the state of the qubit we use microwave pulses. Moreover, in section 2.2.3 we have seen that this state manipulation in the context of a single qubit experiment is described by a collection of single qubit gates, which can be visualized on the Bloch sphere as a composition of rotation operators.

The dependence on the rotation angle θ of the state vector with respect to the amplitude of the pulse A and the length of the pulse P_l is described through equation 2.2.11. The purpose of the *Rabi Measurement* (see fig 5.5.1) is to calibrate the amplitude and length of the pulses in order to be able to rotate the state vector of the qubit by a desired angle (i.e. obtaining $\pi/2$ pulses, π pulses, ...).

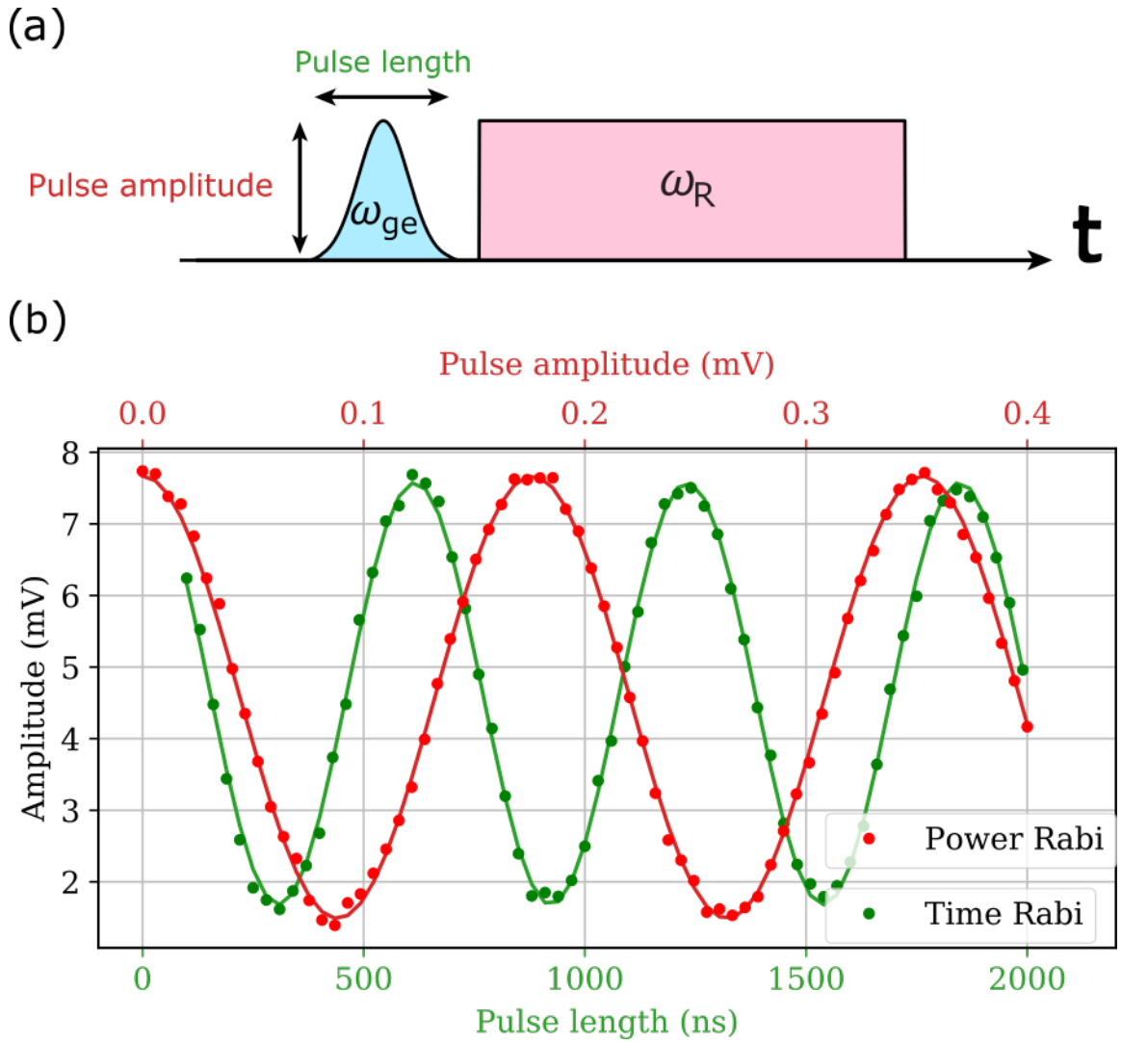

Figure 5.5.1: Rabi oscillations
(a) Pulse sequence used to Rabi drive the qubit. The sequence is composed of a drive pulse (light blue pulse) with variable length (*Time Rabi*) and fixed amplitude (Pulse amplitude=0.06 mV) or variable amplitude (*Power Rabi*) and fixed length (Pulse length=300 ns). The drive pulse has frequency ω_{ge}, and is followed by a readout pulse (light pink pulse) applied to the cavity with frequency ω_R. The shape of the envelope of the drive pulse is chosen to be gaussian in order to minimize unwanted frequency components due to the finite length of the pulse that could excite the qubit in higher electronic levels out of the computational subspace. **(b)** Rabi oscillations induced by sweeping the amplitude of the pulse (Power Rabi, red line) or by changing the length of the pulse (Time Rabi, green line).

5.6 T1 measurement

As we have seen in section 3.1.1, the process of depolarization induced by the energy transfer between the qubit and the environment is quantified through the measurement of the *relaxation time* T_1.

The pulse sequence for the T_1 measurement along with the experimental data can be found in figure 5.6.1.

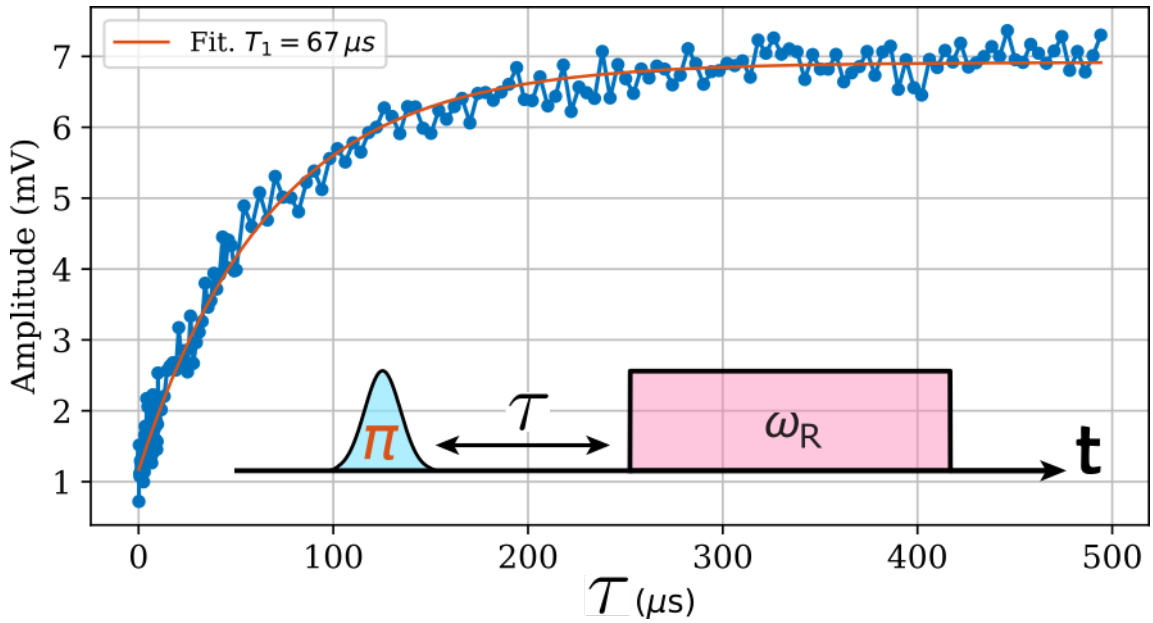

Figure 5.6.1: In the figure above we can see the longitudinal (T_1) decay of the qubit along with the respective pulse sequence. At first the qubit is driven into the excited state by a gaussian π pulse (light blue pulse), then, after a waiting time τ, the state of the qubit is read with a readout pulse (light pink pulse) with a frequency ω_R in resonance with the cavity peak relative to the qubit in the ground state. Since the energy of the thermal bath is much smaller than the energy separation of the ground state and the excited state of the qubit ($k_bT << \hbar\omega_{qb}$), in the long time limit (i.e. $\tau >> 1/\Gamma_1$) the qubit decays into the ground state ($p = 1$), which corresponds to the maximum amplitude of the readout signal.

5.7 T2 measurement

We have seen in section 3.1.2, that the process of decoherence is characterized by a loss of information about the off diagonal element of the density matrix, i.e. a loss of information about $\langle\sigma_x(t)\rangle$. Moreover, we have seen that this loss is quantified through the measurement of the *coherence time* T_2.

The pulse sequence for the T_2 measurement along with the experimental data can be found in figure 5.8.1. As we can see, the pulse sequences for measuring T_2 are composed of a $\pi/2$ pulse at the beginning and at the end of the sequence after some waiting time in which the state undergoes a free evolution.

The purpose of the first $\pi/2$ pulse is easy to justify: it creates the coherent superposition between the ground and excited state of the qubit, which is an eigenstate of the σ_x operator.

This is verified easily by the following equations

$$(\theta_{in}, \phi_{in}) = (0, 0)\,, \tag{5.7.1}$$

$$(|g\rangle\,, |e\rangle) = \begin{pmatrix}0\\1\end{pmatrix}, \begin{pmatrix}1\\0\end{pmatrix}, \tag{5.7.2}$$

$$|\psi_{in}\rangle = \cos\frac{\theta_{in}}{2}\,|g\rangle + \exp\{i\phi_{in}\}\sin\frac{\theta_{in}}{2}\,|e\rangle\,, \tag{5.7.3}$$

$$|\psi(\tau=0)\rangle = \mathrm{R_y}(\theta=\pi/2)\,|\psi_{in}\rangle\,, \tag{5.7.4}$$

$$|\psi(\tau=0)\rangle = \frac{1}{\sqrt{2}}\,(|g\rangle + |e\rangle)\,, \tag{5.7.5}$$

$$\rho\,(\tau=0)) = \frac{1}{2}\begin{pmatrix}1 & 1\\ 1 & 1\end{pmatrix}, \tag{5.7.6}$$

where ($|g\rangle$, $|e\rangle$) represent the ground and excited state of the qubit, $|\psi_{in}\rangle$ is the state vector of the qubit in steady state condition, (θ, ϕ) are the zenithal and azimuthal angle for the state vector expressed in polar coordinates (see fig 2.1.1), τ is the free evolution time of the qubit (i.e. the time between the first and the last $\pi/2$ pulses).

The time evolution of the density matrix under decoherence processes has been already calculated in the general case (see equation 3.1.20). For the initial conditions expressed in eq. 5.7.6, the time evolution of the density matrix is

$$\rho\,(\tau) = \frac{1}{2}\begin{pmatrix}e^{-\Gamma_1\tau} & e^{-\Gamma_2\tau}\\ e^{-\Gamma_2\tau} & e^{-\Gamma_1\tau}\end{pmatrix}.$$

We are interested to measure the decay of the coherences of the density matrix, i.e. the elements that decay with the transverse rate $\Gamma_2 \equiv 1/T_2$. The most intuitive way would be to measure the expectation value of $\langle\sigma_x(\tau)\rangle$:

$$\begin{aligned}\langle\sigma_x(\tau)\rangle &= \mathrm{Tr}\,[\rho\sigma_x]\\ &= \mathrm{Tr}\left[\frac{1}{2}\begin{pmatrix}e^{-\Gamma_1\tau} & e^{-\Gamma_2\tau}\\ e^{-\Gamma_2\tau} & e^{-\Gamma_1\tau}\end{pmatrix}\begin{pmatrix}0 & 1\\ 1 & 0\end{pmatrix}\right]\\ &= \mathrm{Tr}\left[\frac{1}{2}\begin{pmatrix}-\Gamma_2\tau & e^{-\Gamma_1\tau}\\ e^{-\Gamma_1\tau} & e^{-\Gamma_2\tau}\end{pmatrix}\right]\\ &= e^{-\Gamma_2\tau}\end{aligned}$$

In the experiment, we are able to measure the eigenvalues of the qubit along the quantization axis z, i.e. $\langle\sigma_z(\tau)\rangle$. The purpose of the last $\pi/2$ pulse essentially is to transform the qubit density matrix into the σ_x measurement basis. Essentially one can measure the eigenvalues of σ_x by measuring the eigenvalues of σ_z. With a little calculation,

we can see that

$$
\begin{aligned}
\left[|g\rangle\right]_x &= \mathrm{R_y}\left(\theta = \pi/2\right)|g\rangle = \frac{1}{\sqrt{2}}\begin{pmatrix}1\\1\end{pmatrix} \\
\left[|e\rangle\right]_x &= \mathrm{R_y}\left(\theta = \pi/2\right)|e\rangle = \frac{1}{\sqrt{2}}\begin{pmatrix}1\\-1\end{pmatrix} \\
\left[\rho\right]_x &= \mathcal{S}_{x\to z}^{-1}\left[\rho\right]_z \mathcal{S}_{x\to z} \\
\mathcal{S}_{x\to z}^{-1} &= \mathcal{S}_{x\to z} = \frac{1}{\sqrt{2}}\begin{pmatrix}1 & 1\\1 & -1\end{pmatrix} \\
\left[\rho\left(\tau\right)\right]_x &= \frac{1}{2}\begin{pmatrix}1 & 1\\1 & -1\end{pmatrix}\begin{pmatrix}1/2\, e^{-\Gamma_2\tau} & 1/2\, e^{-\Gamma_1\tau}\\1/2\, e^{-\Gamma_1\tau} & 1/2\, e^{-\Gamma_2\tau}\end{pmatrix}\begin{pmatrix}1 & 1\\1 & -1\end{pmatrix} \\
&= \frac{1}{2}\begin{pmatrix}e^{-\Gamma_1\tau} + e^{-\Gamma_2\tau} & 0\\0 & e^{-\Gamma_1\tau} - e^{-\Gamma_2\tau}\end{pmatrix} \\
\left[\langle\sigma_z\left(\tau\right)\rangle\right]_x &= \mathrm{Tr}\left[\left[\rho\right]_x\sigma_z\right] = \frac{1}{2}\left(e^{-\Gamma_1\tau} - e^{-\Gamma_1\tau} + 2e^{-\Gamma_2\tau}\right) \\
&= e^{-\Gamma_2\tau} \\
\left[\langle\sigma_z\left(\tau\right)\rangle\right]_x &\equiv \langle\sigma_x(\tau)\rangle
\end{aligned}
$$

where ($\left[|g\rangle\right]_x$, $\left[|e\rangle\right]_x$) represent the ground and excited state of the qubit transformed in the x basis by the $\pi/2$ pulse, $\mathcal{S}_{x\to z}$ is the usual basis transformation matrix and $\left[\rho\left(\tau\right)\right]_x$ is the density matrix in the x basis.

5.8 T_{echo} measurement

In the previous chapter we have defined the transverse relaxation rate Γ_2 as the decoherence rate of the off diagonal elements of the density matrix. In section 3.1.2 we have calculated the rate of this process for some quantum systems by solving the master equation in the Linblad formalism.

As we have already described in the introduction of chapter 3.1 the solution of the master equation in the Linblad formalism requires several approximations. The Markov approximation, for example, requires that the environmental correlation functions decay on a time scale fast compared to those of the system [26], i.e. the environmental noise has to be described by white noise with high frequency cutoff [1]. The thermal noise, for example, falls within the Markov approximation and as a result the coherence decay is exponential as described in the previous chapters. On the other hand, one archetipal form of noise that is always present in the Circuit QED architecture is represented by $1/f$ noise, which is singular near $\omega = 0$, has long coherence times and does not fall within the Markov approximation.

In order to decouple the qubit from this source of noise we use the very well known Hahn echo sequence in which a π pulse is inserted at midway with respect to the two $\pi/2$ pulses (see fig. 5.8.1). The additional pulse (see [8] for details) has the effect of frequency filtering the noise at low frequency and therefore is very effective fot 1/f noise components. The measurement of T_{echo} along with the relative pulse sequence is described in fig 5.8.1.

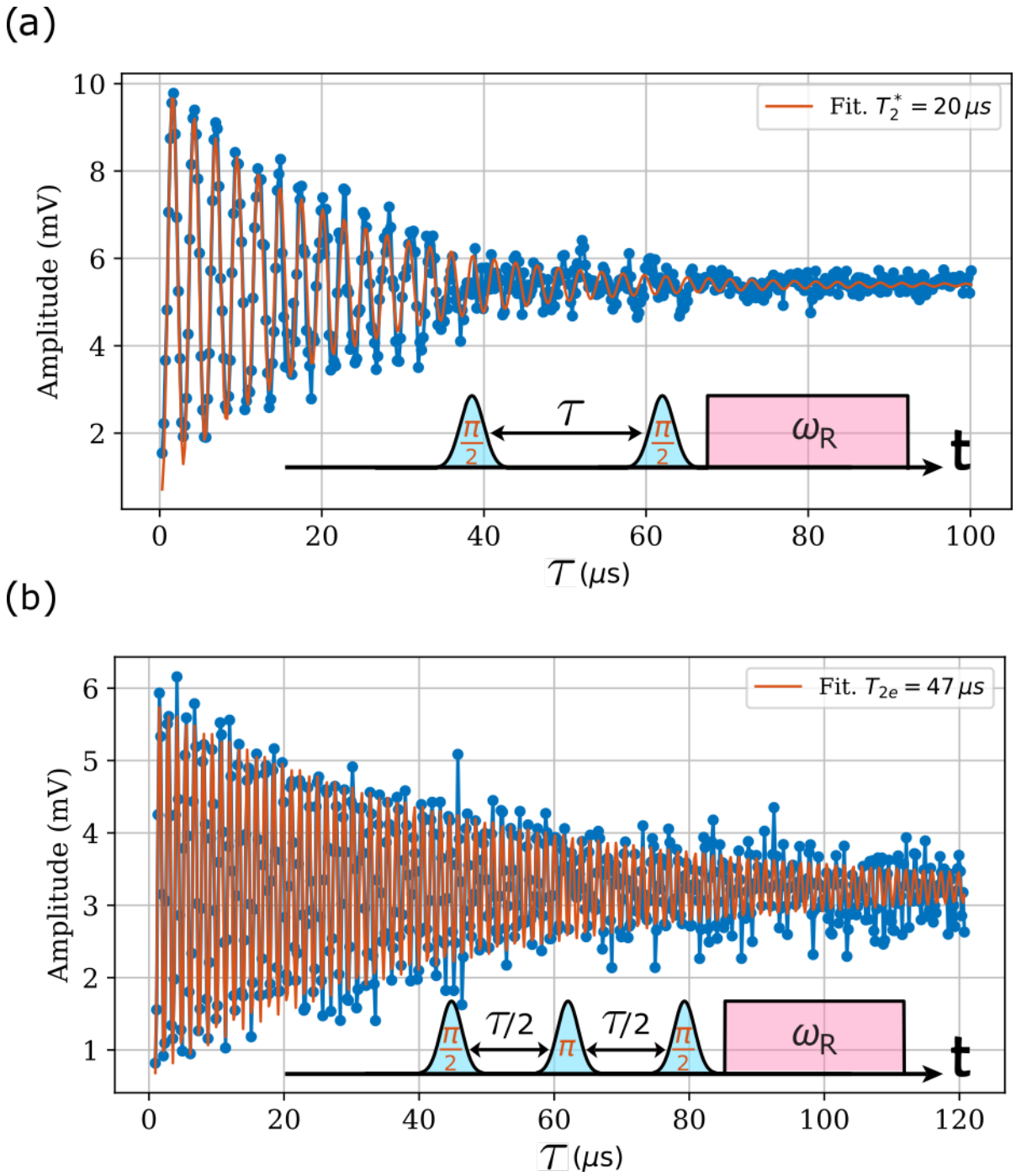

Figure 5.8.1: Transverse relaxation
(a) Decoherence measurement via Ramsey interferometry. At first the qubit is prepared in a coherent state $|\psi\rangle = \frac{1}{\sqrt{2}}(|g\rangle + |e\rangle)$ by applying a $\pi/2$ gaussian pulse (light blue pulse) on the qubit. After a time τ, a second $\pi/2$ pulse is sent in order to transform the qubit density matrix onto the σ_x measurement basis, where the qubit state is read with a readout pulse (light pink pulse) applied to the cavity. In the long time limit (i.e. $\tau >> \Gamma_2$) the qubit state decays into a complete depolarized state $p = 0$ corresponding to a readout amplitude of $\simeq 5.8\,\text{mV}$. **(b)** Decoherence measurement using a Hahn echo experiment. The qubit state is prepared and measured in the same way as the Ramsey experiment. The difference is that a π pulse is applied at midway respect to the two $\pi/2$ pulses, which makes the qubit less sensitive to dephasing noise at low frequencies. Consequently, the relaxation time T_{2e} measured with the Hahn echo pulse sequence is much higher than the relaxation time T_2^* measured with the Ramsey pulse sequence ($T_{2e} \simeq 47\,\mu s$, $T_2^* \simeq 20\,\mu s$)
.

5.9 Qubit temperature measurement

As we have seen in section 3.1.1.1 the steady state of the qubit (i.e. the population of the state $|g\rangle$ and $|e\rangle$) carries information about the qubit temperature which in turn reflects the temperature of the effective bath at the qubit frequency.

One way to determine the excited state population of the qubit is through qubit spectroscopy measurements (see 5.3) in which the ratio of the peak heights with respect to the $|g\rangle$ to $|e\rangle$ transition and $|e\rangle$ to $|f\rangle$ transition reflects the ratio of population of the relative states. However, this method does not take into account the variation of readout efficiency with qubit state and it is therefore not quantitative without further corrections [39].

Another measurement method which is independent of the readout efficiency is the Rabi Population Measurement (RPM, see [39] [40]). The basic idea of RPM is to measure two Rabi oscillations whose amplitude ratio corresponds directly to the ratio of initial excited state (P_e) to ground state population (P_g).

The first assumption is that the population above the $|e\rangle$ state is negligible (that is usually true for the range of temperature of the experiment, $40 - 130\,\mathrm{mK}$), so $P_e + P_g = 1$. An example of the pulse sequence along with a typical measurement is shown in fig 5.9.1. Following the initial assumption we can see that

$$P_{|g\rangle} + P_{|e\rangle} = 1 \tag{5.9.1}$$

$$P_{|f\rangle} = 0 \tag{5.9.2}$$

$$A_e = A_0\, P_{|e\rangle} \tag{5.9.3}$$

$$A_g = A_0\, P_{|g\rangle} \tag{5.9.4}$$

Where $P_{|g\rangle}$, $P_{|e\rangle}$, $P_{|f\rangle}$ represent the probability of the qubit to be in the $|g\rangle$, $|e\rangle$, $|f\rangle$ state. For low temperatures the population $P_{|f\rangle}$ is approximated to zero. A_e and A_g are the Rabi amplitudes measured with the RPM technique, and A_0 is a factor converting the qubit state occupation probability to the readout voltage [40].

$$P_{|e\rangle} = \frac{A_e}{A_0} = \frac{A_e}{A_e + A_g}$$

The excited state population is then used to calculate the temperature of the qubit following a Boltzmann distribution of a two level system (see eq. 4.1.11).

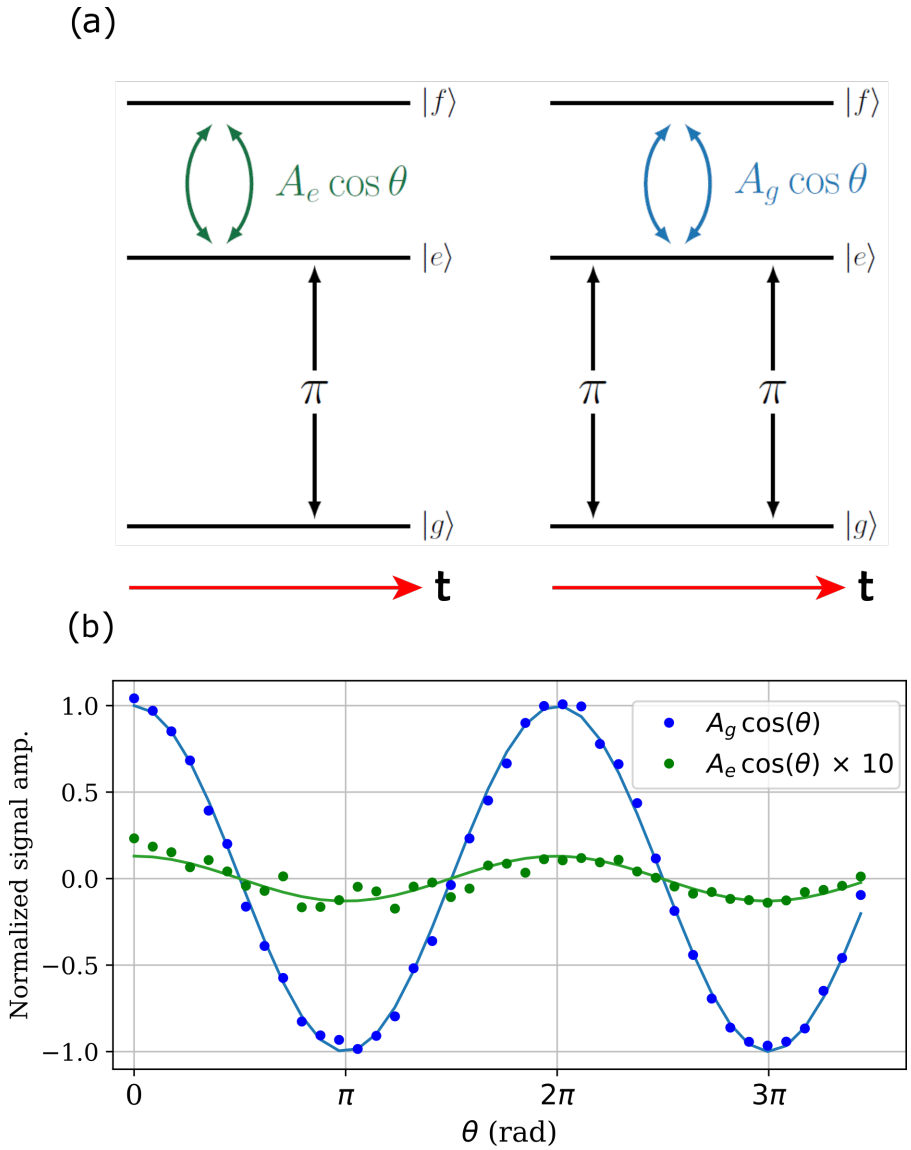

Figure 5.9.1: Rabi Population Measurement
(a) Schematic diagram of the Rabi Population Measurement (RPM) technique used for measuring the Rabi amplitudes A_g and A_e. The Rabi amplitude A_e is measured by first Rabi driving the $|e\rangle$ to $|f\rangle$ transition, then by swapping the populations between the $|e\rangle$ to $|g\rangle$ state with a π pulse and at last by performing qubit readout on the cavity peak corresponding to the $|g\rangle$ state. The Rabi amplitude A_g is measured in the same manner as A_e, with the exception that initially the populations between the $|g\rangle$ state and the $|e\rangle$ state are swapped with a π pulse. **(b)** Example of A_e and A_g measurement for a qubit with a $P_{|e\rangle} = 1.3\,\%$, corresponding to a qubit temperature of about $T = 66\,\mathrm{mK}$.

5.10 Cavity temperature measurement

We have seen in section 3.2 that the mean number of photons in the readout resonator reflects the temperature of the effective thermal bath at the resonator frequency. Moreover, we know that the steady state of the resonator is described by a thermal state, with the relative population of the levels described by the well known equation 3.2.4.

As a result, one way to determine the temperature of the cavity is through qubit spectroscopy measurements (see 5.3) in which the height ratio of the photon number peaks (each photon produces a qubit stark shift of χ, see eq. 2.2.16) is used to gather information about the population of the photon number states of the readout resonator (see [20] [18]). However, in order to perform this experiment it is necessary to be in the strong dispersive regime (where the Stark shift per photon is much larger than the decoherence rates [18] $\chi >> \gamma$, κ, $1/T$) whereas in this thesis the experiment is performed in the intermediate dispersive regime (where $\kappa \simeq \chi$, for which the optimal readout condition can be achieved [41]).

Another way in which we can infer information about the temperature of the readout resonator is through the measurement of the dephasing Γ_ϕ^{th} induced by the thermal photon in the resonator. Following the work of [8], an engineered thermal noise (see fig. 5.10.1) is used to sweep the mean number of photons in the readout resonator $n_{th} = n_0 + n_{added}$ while for each point the qubit dephasing $\Gamma_\phi = 1/2T_1 - 1/T_{2echo}$ is measured with consecutive T_1 (see section 5.6) and T_{2echo} (see section 5.7) measurements. It is important to note that for the decoherence measurement of the qubit we use the Hann echo sequence (see section 5.8) which ensures a decoupling from $1/f$ noise sources and keeps the approximation $\Gamma_\phi \simeq \Gamma_\phi^{th}$ reliable.

Since the relation of Γ_ϕ^{th} and n_{th} is linear (see fig. 3.3.1), by performing a linear regression it is possible to extract the photon population n_0 with respect to the temperature of the mode of the readout resonator.

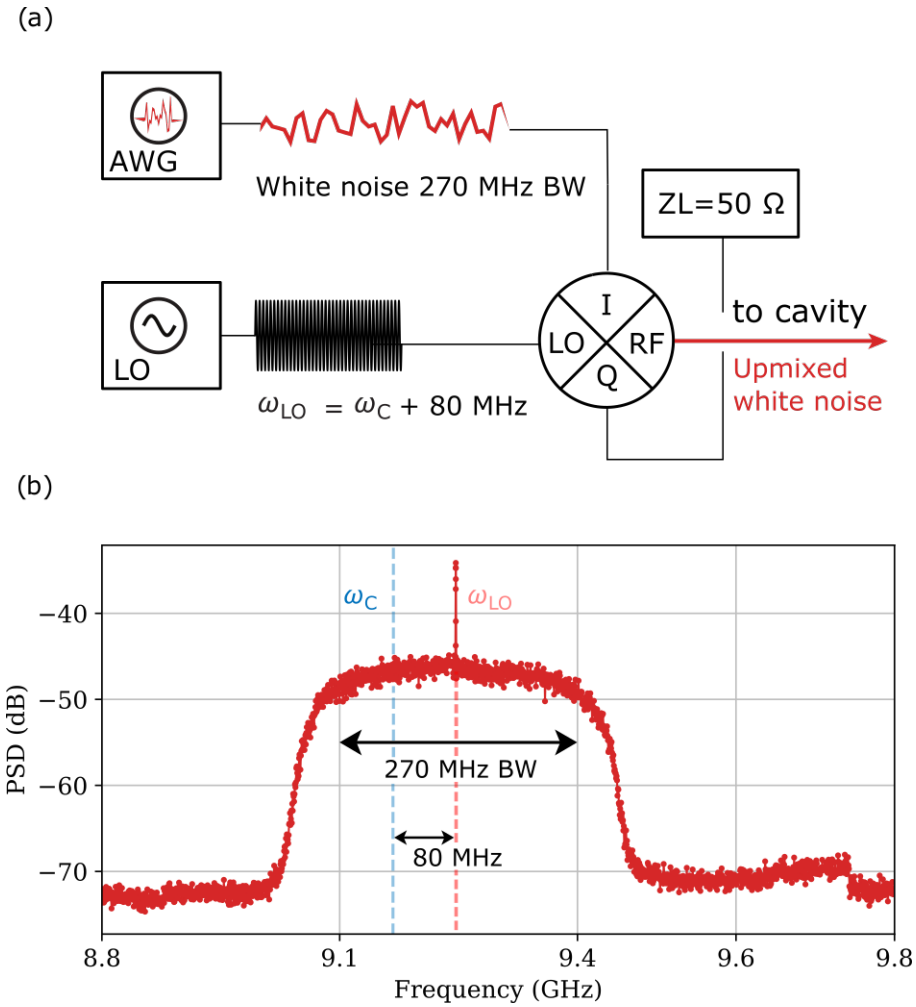

Figure 5.10.1: White noise upmixing
(a) Schematic diagram of the experimental apparatus used to engineer artificial thermal noise. A 270 MHz bandwidth white noise generated by a BK Precision 4063 Arbitrary Waveform Generator is upmixed with a continuous microwave tone ω_{LO} by means of a one port terminated IQ mixer. The upmixed white noise is sent to the readout cavity to form a thermal state with mean number of photons $n_{th} = n_0 + n_{added}$. **(b)** Spectral profile of the engineered thermal noise measured at the spectrum analyzer. As we can see, the artificial photon source exhibits a white noise behavior over a wide frequency range, centered around the frequency ω_{LO} used for the upmixing process. The frequency of the local oscillator is detuned by 80 MHz with respect to the cavity frequency in order to avoid dephasing backaction from coherent photons in the readout resonator.

Chapter 6

Experimental setup

This chapter contains the general information on the experimental apparatus used for the measurements performed in the two cooldowns. In the first section the general wiring scheme of the experimental apparatus (see fig. 6.1.1) along with the theoretical predictions of the mean number of photons and temperature (see fig. 6.1.2) are shown. The following sections describe the key components used in the experimental apparatus: the transmon qubit, the Readout resonator, the Input bath couplers.

6.1 From room temperature to 20 mK

The general scheme of the experimental setup for the measurements performed in the two cooldowns is shown in fig. 6.1.1.

As we can see in both of the cases the structure of the input and output line is maintained fixed but two different "input couplers" (see section 6.4) are used: an aluminium section (WG 90 in panel **a** of fig. 6.1.1) or a BRCA (cavity attenuator + WG90 in panel **a** of fig. 6.1.1).

Moreover, using equations eq. 4.1.4 and eq. 4.1.5 is possible to model the expected temperature and mean number of photons relative to the input and output bath for the wiring configuration of fig. 6.1.1. The predictions are plotted in figure 6.1.2.

We have seen in section 4.1.3 that the interaction between a quantum system -qubit or resonator- with multiple baths can be described as an interaction between the quantum system and one fictious effective thermal bath.

Moreover, we have seen that the mean number of photons and the temperature of the effective thermal bath depends on the relative coupling between the quantum system and the baths. In the approximation of low internal losses the only two baths that interact with the quantum system are the input bath and the output bath.

Following eq. 4.1.7 and eq. 4.1.8, it is easy to convince ourselves that the temperature and mean number of photons of the effective thermal bath will be bounded by the values of the input and output bath, shown in panel **c** of fig. 6.1.2.

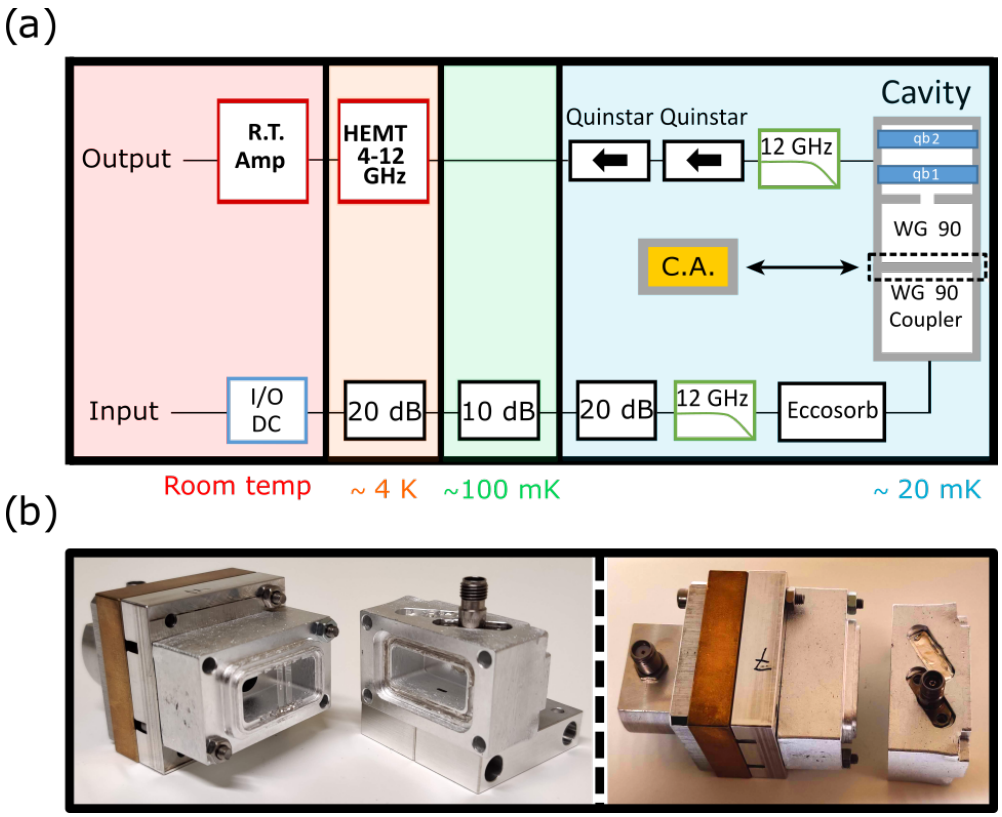

Figure 6.1.1: Experimental apparatus
(a) Schematic diagram describing how the Circuit QED architecture (cavity and qubits) is wired to the input and output line of the Cryostat. The input line consists of a DC block at room temperatures, attenuators at different temperature stages, a high pass filter and an Eccosorb [42] filter. In the first experiment the cavity is connected to the input with a waveguide aluminium section through a hole (see fig. 6.3.1); in the second experiment a cavity attenuator (see panel **b** of fig. 6.4.1) is added in series to the waveguide section forming the BRCA (see section 4.3.2). On the output side, the cavity (see fig. 6.3.1) is coupled through a low pass filter, two isolators of $\simeq 20\,\mathrm{dB}$ of isolation each and the amplification chain (the HEMT amplifier and the room temperature amplifiers). **(b)** Pictures of the Circuit QED architecture used in the second cooldown. From left to right: Waveguide coupler, cavity attenuator + waveguide section (BRCA), first half of the cavity, qubits, second half of the cavity, sma connector.

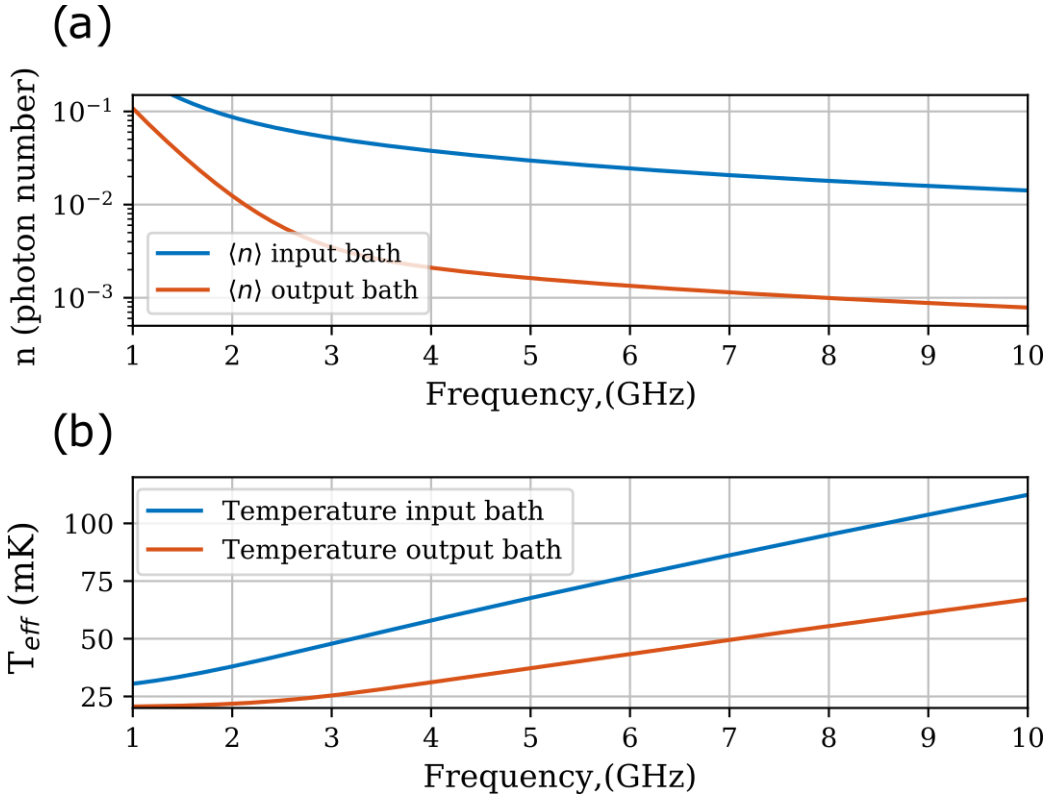

Figure 6.1.2: Input/output thermal bath
(a) Mean number of photons describing the input bath reservoir (see eq. 4.1.4) and the output bath reservoir (see eq. 4.1.5) with respect to the setup described in fig. 6.1.1. **(b)** Effective temperature of the input and output bath.

6.2 transmon qubit

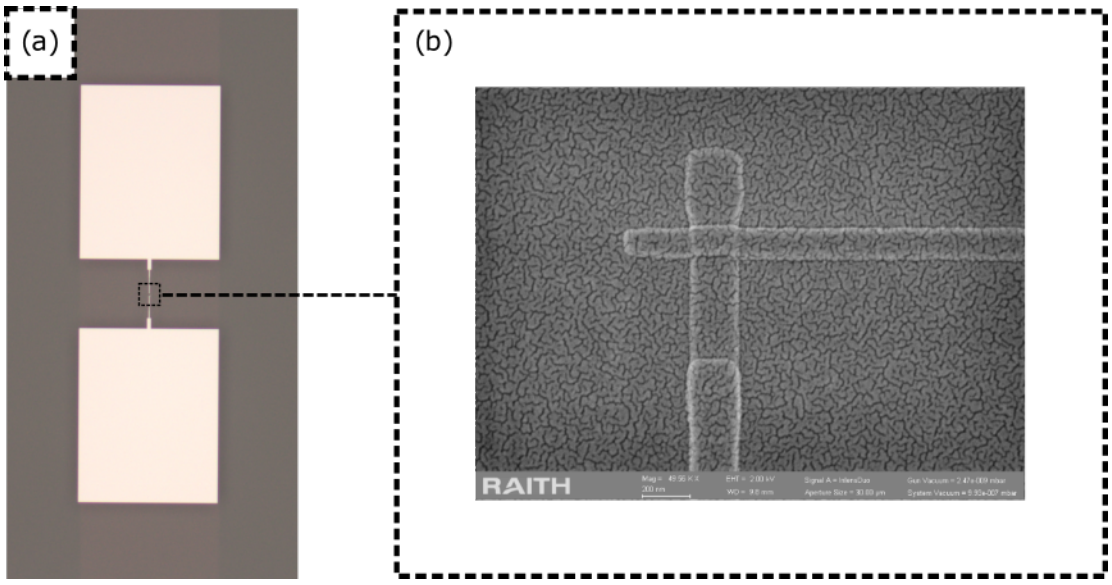

Figure 6.2.1: transmon qubit
(a) Microscope picture of the transmon qubit. **(b)** E-beam picture of the cross-type junction.

The transmon qubit (see panel **a** of fig. 6.2.1) consists of two aluminium pads (which have the double purpose of coupling the qubit to the resonator and to capacitively shunt the Josephson Junction) connected through a Josephson junction.

The junction (see panel **b** of fig. 6.2.1) is a cross-type junction fabricated using standard electron beam litography with double angle evaporation technique. The junction consists of two films of aluminium layers with a thickness of 25 nm and 30 nm separated by an AlOx barrier grown through thermal oxidation for 1 min/1 mbar static pressure of 100 % oxygen.

The area of the junction along with the insulator thickness determines the critical current of the Josephson junction, which in turn, determines the frequency of the qubit. The important fabrication parameters of the transmon qubits used in the experiment are shown in tab 7.1.1.

	Junction area	**Oxidation time / Pressure**	**Pad dimensions**
$\mathbf{qb}_1$	240 nm X 160 nm	1 min / 1 mbar	500 μm X 400 μm
$\mathbf{qb}_2$	300 nm X 160 nm	1 min / 1 mbar	500 μm X 400 μm

Table 6.2.1: Collection of important fabrication parameters of the transmon qubit design.

6.3 Readout resonator

The readout resonator (see fig 6.3.1) consists of two halves of a waveguide aluminium cavity. Between the interface of the two halves some slots are machined in order to host the transmon qubits.

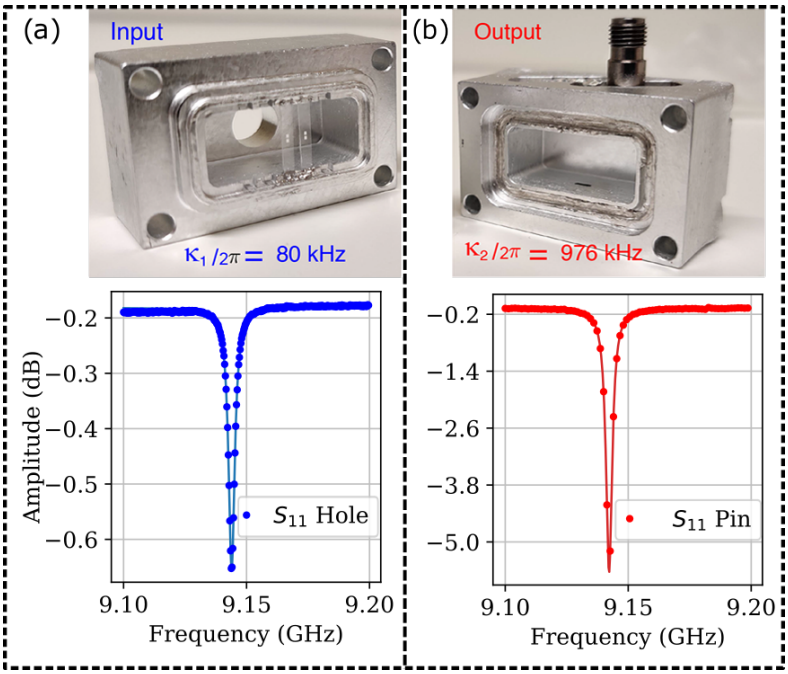

Figure 6.3.1: Readout resonator
Aluminium waveguide cavity used as a readout resonator. The microwave radiation enters the first half of the cavity from a hole (see panel **a**) and exits from the second half through a pin in the sma connector (see panel **b.**) The coupling of the resonator to the input line (κ_1) and output line (κ_2) are tuned respectively by changing the dimension of the aperture and the length of the pin. The measurements of the coupling rates κ_1, κ_2 are carried out by measuring the cavity in reflection through one of the ports while creating a short on the other port (i.e. closing the hole with aluminium tape).

As we have seen in section 2.2.4 the important parameters for the readout resonator are represented by the frequency ω_c, the input coupling κ_1, the output coupling κ_2 and the coupling relative to the internal loss κ_{loss}. In the readout resonator used in this thesis κ_{loss} is approximated to zero. This approximation comes from the fact that the cavity is made of aluminium, and aluminium presents extremely low losses at mK temperature.

The important fabrication parameters of the readout resonator used in the experiment along with the depending physical variables to which they are linked are shown in tab. 6.3.1.

Cavity inner dimensions	22 mm X 22 mm X 10 mm	$\omega_c/2\pi$	9.204 GHz
Hole diameter	7.64 mm	$\kappa_1/2\pi$	80 kHz
Pin gap	-4.7 mm	$\kappa_2/2\pi$	976 kHz

Table 6.3.1: In the table above we can see the important parameters for the cavity design along with the physical variable to which they are linked. As we have already seen, the cavity inner dimension are linked to the frequency of the fundamental mode ω_c by eq. 2.2.13. The diameter of the aperture (see panel **a** of fig. 6.3.1) is directly proportional to the input coupling rate κ_1, while the pin gap (distance between the internal wall of the cavity and the tip of the pin) determines the output coupling rate κ_2.

6.4 Input bath couplers

The lossless objects used to change the coupling between the readout resonator and the input bath are a waveguide section (see panel **a** of fig. 6.4.1) and the BRCA (see section 4.3.2). The BRCA is composed of an aluminium waveguide section and a cavity attenuator (panel **a** and **b** of fig 6.4.1). The Transmission profile of the waveguide section and the BRCA can be found in panel **c** of fig. 6.4.1.

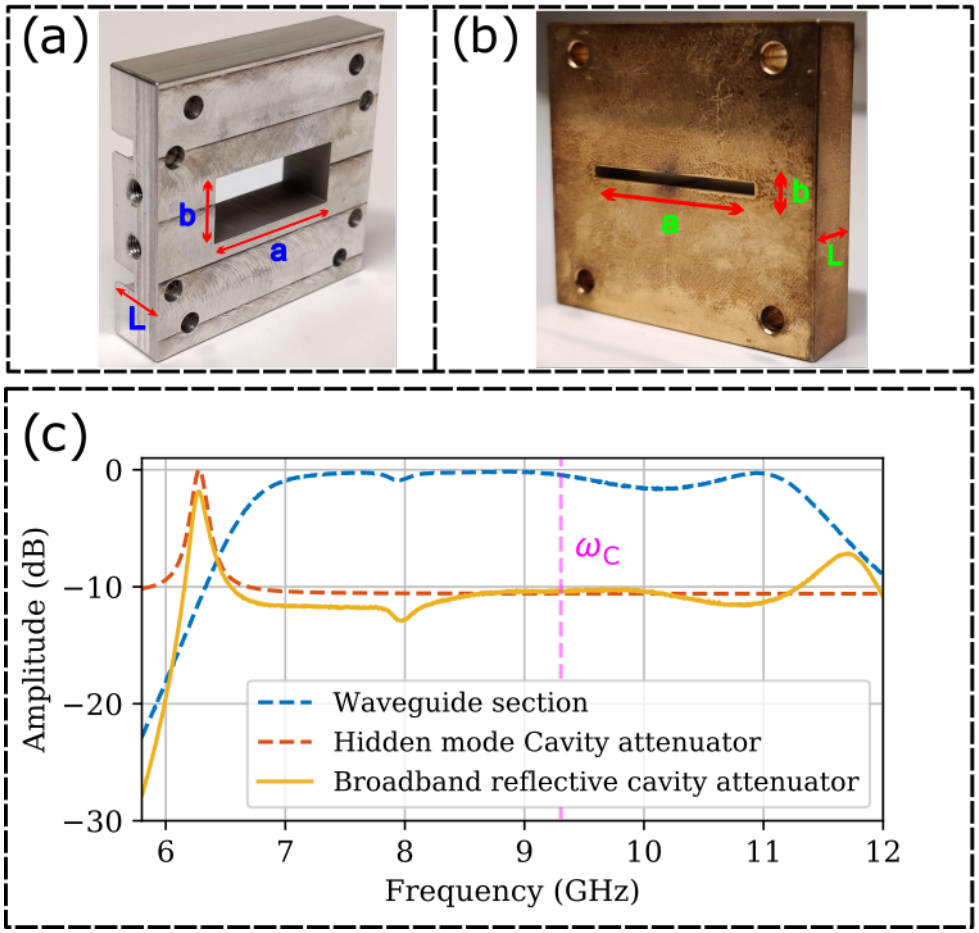

Figure 6.4.1: Input bath couplers
(a) Section of a WR90 aluminium waveguide used to couple directly the readout resonator in the first cooldown and as a component of the BRCA in the second cooldown. The dimensions a, b, d are described in tab. 6.4.1. **(b)** Home made cavity attenuator used with the aluminium section of panel **a** in order to form the BRCA. The dimension of the block can be found in tab. 6.4.1. **(c)** S_{21} Transmission profile of the waveguide section (blue dashed line, measured values) the hidden mode of the cavity attenuator (red dashed line, simulated values) and the BRCA (yellow solid line, measured values). The values of $|S_{21}|^2$ at the frequencies of the cavity and qubits will modify the coupling between the quantum objects and the input bath according to equation 4.2.1.

The waveguide section consists of a 1 cm section of aluminium WR 90 waveguide, which couples to the cavity through the cavity hole (see panel **a** of figure 6.3.1). The

internal dimensions of the waveguide along with the power transmission at the important frequencies can be found in tab. 6.4.1.

The BRCA consists of a cavity attenuator made of brass in series with an aluminium section. The internal dimensions of the cavity attenuator along with the power transmission of the BRCA at the important frequencies can be found in tab. 6.4.1.

	(a, b, l)	$S_{21}(\omega_{qb1}/2\pi)$	$S_{21}(\omega_{qb2}/2\pi)$	$S_{21}(\omega_{cav}/2\pi)$
Waveguide section	(22.86 mm, 10.16 mm, 10 mm)	−30.8 dB	−1.6 dB	−0.3 dB
Cavity attenuator	(26 mm, 1.74 mm, 10 mm)			
BRCA		−39.8 dB	−11.5 dB	−10.4 dB

Table 6.4.1: In the table above we can see the important parameters for the input couplers design along with the physical variable to which they are linked. The waveguide section internal dimension determines both the cutoff frequency (see eq. 4.3.1) and the amount of reflection below the cutoff (the "steepness" of the S_{21} profile in panel **c** of figure 6.4.1). The internal dimensions of the cavity attenuator determine the frequency of the mode (see the hidden mode in panel **c** of figure 6.4.1) and the amount of reflection out of resonance. The S_{21} profiles at qubit and cavity frequency of the input couplers (waveguide section and BRCA) are used to calculate the modified coupling of the quantum system to the input bath (see section 4.2).

Chapter 7

Experimental results

This chapter summarizes the key measurements performed in two consecutive cooldowns (respectively section 7.1 and section 7.2) in order to obtain the temperature values of the qubits and the readout resonator (discussed in section 7.3).

The structure of the first two sections that constitute this chapter is indeed the same. At first, a set of measurements are carried out on the Circuit QED architecture in order to benchmark the system, then the temperature measurements on qubit and readout resonator are performed.

The difference between the configurations of the first and second cooldown is represented by the use of different lossless elements between the Circuit QED architecture and the input bath ("input couplers") which modifies the coupling between the quantum systems and the input bath. It is important to recall that the coupling rates between the quantum system and the thermal baths determine the temperature of the effective thermal bath at which the quantum system thermalizes (see section 3.1, section 3.2 and section 4.1.3).

The third section is dedicated to the comparison between the temperature measurements in the different configurations and the theoretical model.

7.1 First cooldown: waveguide section as input coupler

The main feature of the experimental apparatus in the first cooldown (see fig. 6.1.1) is represented by the presence of a section of aluminium waveguide between the qubit-cavity system and the input bath (see figure 6.4.1, point **(a)**).

This section is divided in two parts: subsection 7.1.1 deals with benchmarking of qubit-cavity system while subsection 7.1.2 deals with the temperature measurements.

7.1.1 Characterization

The first set of measurements performed on the Circuit QED architecture are displayed in fig. 7.1.1 and fig. 7.1.2. As we can see, a collection of techniques described in chapter 5 is used in order to benchmark the qubit-cavity system.

Panels **a** of figs. 7.1.1-7.1.2 are associated witn the Qubit spectroscopy measurements. As we have seen in section 5.3, from the spectroscopic peaks related to the one photon transition ω_{ge} and two photons transition $\omega_{ef}/2$ we can recover the qubit frequency $\omega/2\pi$ and anharmonicity α. Table 7.1.1 summarizes the parameters of both the qubits. It is interesting to note that the spectroscopy measurement relative to the $|e\rangle \rightarrow |f\rangle$ reveals a double peak, which is a signature of a Two Level System (TLS) coupled resonantly to the qubit at that frequency.

	$\omega/2\pi$ (GHz)	α (MHz)	$g/2\pi$ (MHz)	$\chi/2\pi$ (MHz)
qb_1	5.425918(2)	322.61(4)	183.37(7)	1.669(2)
qb_2	6.842493(2)	287.07(9)	177.87(3)	3.732(2)

	T_1 (μs)	T_2 (μs)	T_E (μs)	$T_{purcell}$ (μs)
qb_1	47.7(6)	20.1(8)	35.2(8)	61.7(5)
qb_2	20.9(3)	22.4(5)	25.3(6)	25.5(3)

	$\omega_c/2\pi$ (GHz)	$\kappa/2\pi$(MHz)
Cav	9.196693(5)	1.09(1)

Table 7.1.1: In the table above we summarize the parameters of the qubits extracted from the measurements shown respectively in fig. 7.1.1 and fig. 7.1.2.

Panels **b** of figs. 7.1.1-7.1.2 show the Cavity spectroscopy measurements. As we have seen in section 5.4, from the distance between the peaks of the cavity for the qubit in ground state $|g\rangle$ or in the excited state $|e\rangle$ we can obtain the value of the dispersive shift χ and calculate the qubit-cavity coupling g. As expected, the values of the dispersive shift for the different qubits varies following the different values of the detuning Δ between the qubit frequencies and the cavity frequency.

Panels **c** of figs. 7.1.1-7.1.2 are associated with the Power Rabi measurements. As we have seen in section 5.5, from the generated Rabi oscillations is possible to calibrate the pulses in order to rotate the state vector of the qubit of a desired angle. It is possible to

see that the period of the oscillation with respect to the amplitude of the pulse is very different from qb1 and qb2: that feature reflects the difference in coupling with respect to the input line. This difference in coupling is given by the detuning difference of qb1 and qb2 with respect to the readout cavity mode and by the decoupling effect of the waveguide aluminium section, which is 100 times higher for qb1 with respect to qb2 (see tab. 6.4.1).

Panels **d** of figs. 7.1.1-7.1.2 show the T_1 measurements. As we have seen in section 5.6, the measurement of the relaxation time T_1 gives information about the qubit *depolarization* mechanism and about the noise coupled transversally to the qubit. It is important to note that the "low" values of T_1 (good transmon qubits can have T_1 on the order of $\simeq 100\,\mu$s) are determined mostly by the Purcell decay to the output line. Actually, comparing T_1 and $T_{purcell}$ in table 7.1.1 we can see that the Purcell contribution to the energy relaxation time represents 77% of the total for qb1 and the 81% for qb2.

Panels **e** of figs. 7.1.1-7.1.2 are related to the T_2 measurements. As we have seen in section 5.7, the measurement of the relaxation time T_2 gives information about the qubit *decoherence* mechanism induced by the low frequency noise (DC to tens of KHz) coupled longitudinally to the qubit. It is interesting to note that the T_2 measurement of the qb1 presents a *revival* in the decay trace, which is a typical signature of a TLS coupled to the qubit.

Panels **f** of figs. 7.1.1-7.1.2 are associated with the T_{echo} measurements. As we have seen in section 5.8, the measurement of the relaxation time T_{echo} gives information about the decoherence process carried out by noise coupled longitudinally to the qubit at higher frequencies with respect to the T_2 measurement (100 kHz to several MHz). As we can see, as a results of the dynamical decoupling techniques, the values of the coherence measured improved substantially in both of the qubits.

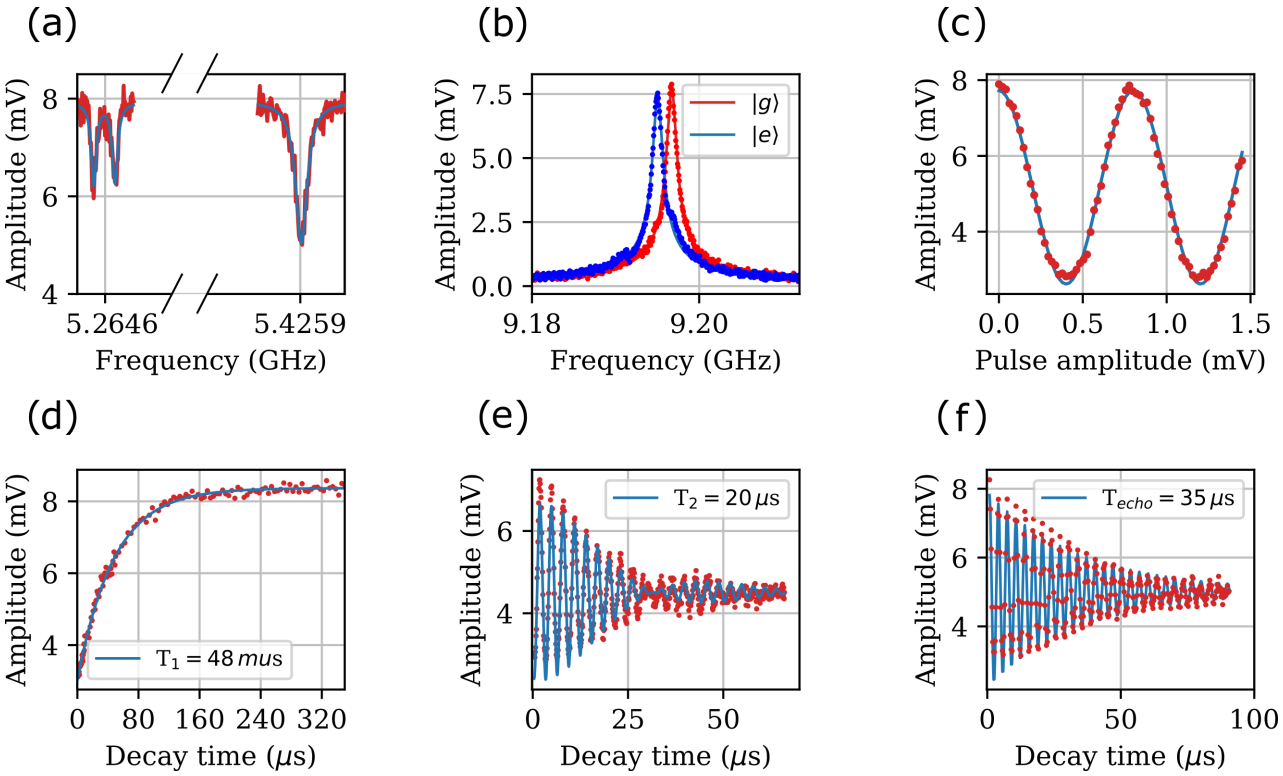

Figure 7.1.1: Qubit 1 characterization
(a) Qubit spectroscopy. **(b)** Cavity spectroscopy. **(c)** Pulse calibration. **(d)** T_1 measurement. **(e)** T_2 measurement. **(f)** T_{echo} measurement.

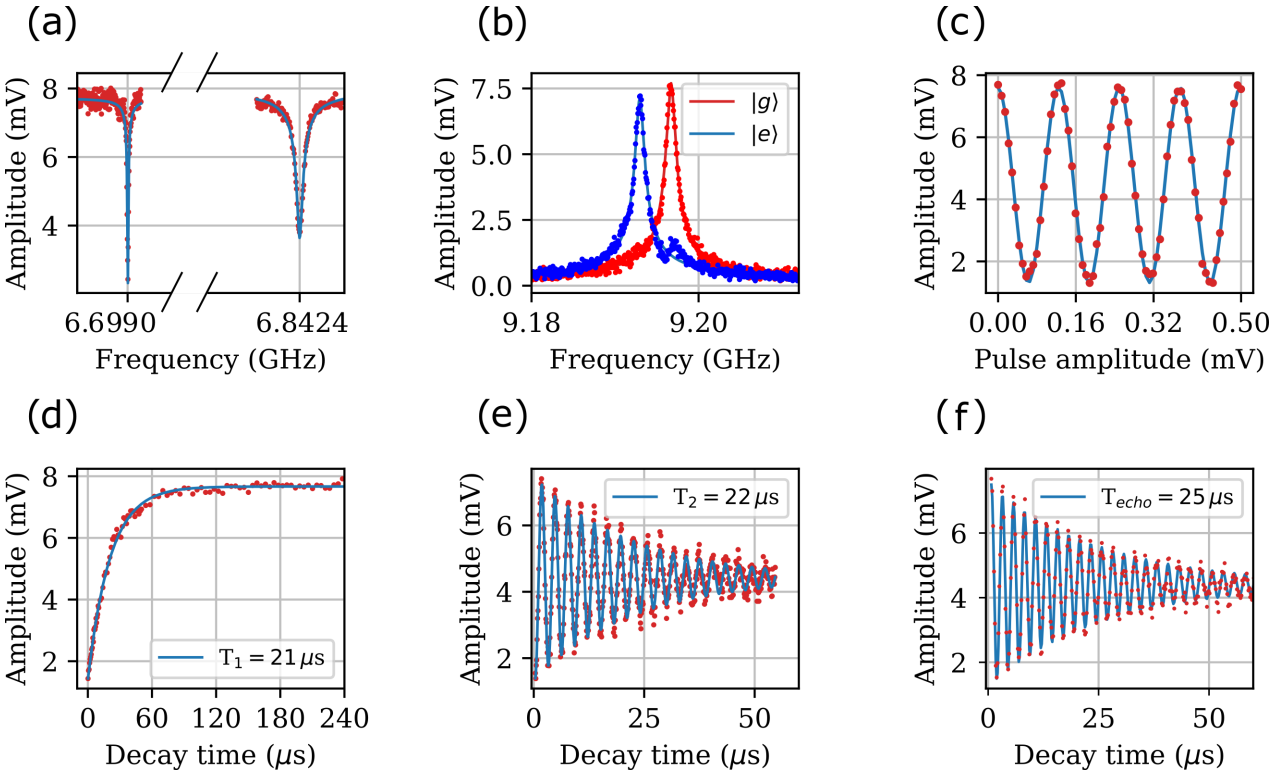

Figure 7.1.2: Qubit 2 characterization
(a) Qubit spectroscopy. **(b)** Cavity spectroscopy. **(c)** Pulse calibration. **(d)** T_1 measurement. **(e)** T_2 measurement. **(f)** T_{echo} measurement.

7.1.2 Temperature measurements

The qubits temperature measurements and the cavity temperature measurements are shown in fig. 7.1.3 and fig. 7.1.4.

Panels **a** and **b** of fig. 7.1.3 show the Rabi Population Measurement (RPM) of qubit 1 and qubit 2. As we have seen in section 5.9, from the amplitude ratio of the Rabi oscillation induced from the $|e\rangle \leftrightarrow |f\rangle$ transition (green points) to the $|g\rangle \leftrightarrow |e\rangle$ transition (blue points) it is possible to address the steady state population of the qubit in the excited state. The steady state solutions of the qubits in the excited state ρ_{11} $(t >> 1/T_1)$ and the relative qubits temperatures $T_{eff}(\omega_{qb})$ are displayed in tab. 7.1.2.

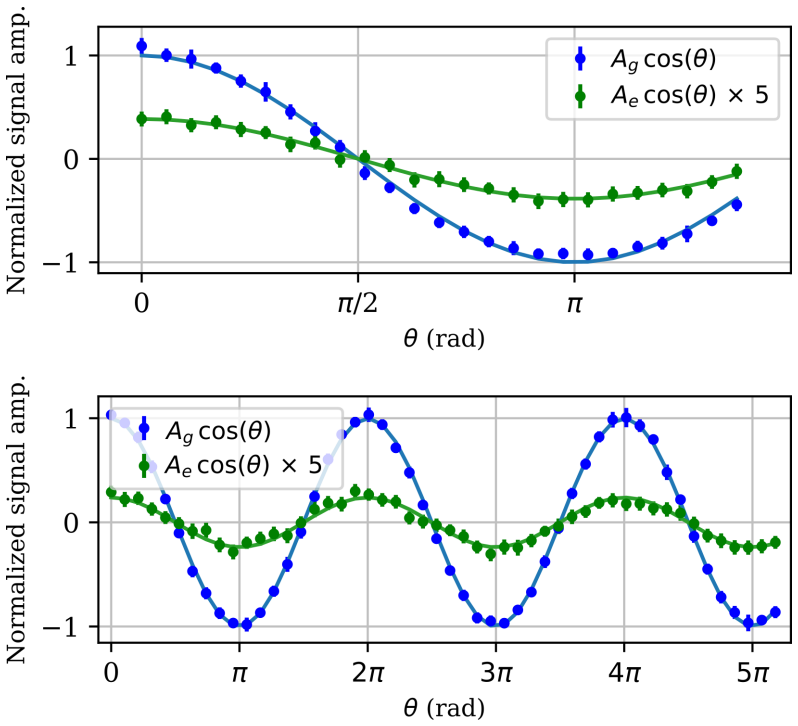

Figure 7.1.3: Qubits temperature measurements
(a) Rabi population measurement performed on qubit 1. **(b)** Rabi population measurement performed on qubit 2.

	ρ_{11} $(t >> 1/T_1)$	T_{eff} (ω_{qb})
qb$_1$	7.2 (3) %	102 (2) mK
qb$_2$	4.5 (2) %	108 (1) mK
	n_{th} $(t >> 1/\kappa)$	T_{eff} (ω_{cav})
Cav (qb$_1$)	0.0044(1)	81(1)
Cav (qb$_2$)	0.0030(1)	76(1)

Table 7.1.2: In the table above we can see the results of the temperature measurements shown respectively in fig. 7.1.3 and fig. 7.1.4. It is important to note that the values of temperature of the cavity $T_{eff}(\omega_{cav})$ and the mean number of photons in the cavity n_{th} have to be intended as upper limits. This feature comes from the fact that these quantities are evaluated from the qubit dephasing in the approximation of $\Gamma_\phi \simeq \Gamma_\phi^{th}$

The measurements of the cavity temperature are shown in fig. 7.1.4. As we have seen in section 5.10, through the injection of engineered thermal photons (panels **a** and **c**) and consecutive qubits dephasing measurements (panels **b** and **d**) it is possible to recover the mean number of photons in the steady state that populates the readout resonator. It is interesting to note how the dephasing behavior of the qubits with respect to the added photons follows the simulations shown in fig. 4.3.2.

From a quantitative point of view, we can see in tab. 7.1.2 that the mean number of photons in the readout resonator for the steady state n_{th} ($t >> 1/\kappa$) measured through qubit 1 does not agree in the range of error with the values measured through qubit 2 (and as a consequence the temperatures too).

One possible explanation about this discrepancy is that the errors in the mean number of photons and temperature are underestimated. Indeed, the temperature of the cavity measured through the qubit 1 have been taken 2 days before the temperature of the cavity recorded through qubit 2, and slow variation of the experiment parameters could have affected the measurements. In any case, it is important to remember that even if these values are different out of the range of error, they are anyway consistent because the cavity temperature values measured through qubit dephasing have always to be intended as upper limits (see [36, 9]). This can be explained from the fact that the qubit dephasing present always an unknown offset (i.e. $\Gamma_\phi = \Gamma_\phi^{th} + \Gamma^{others}$).

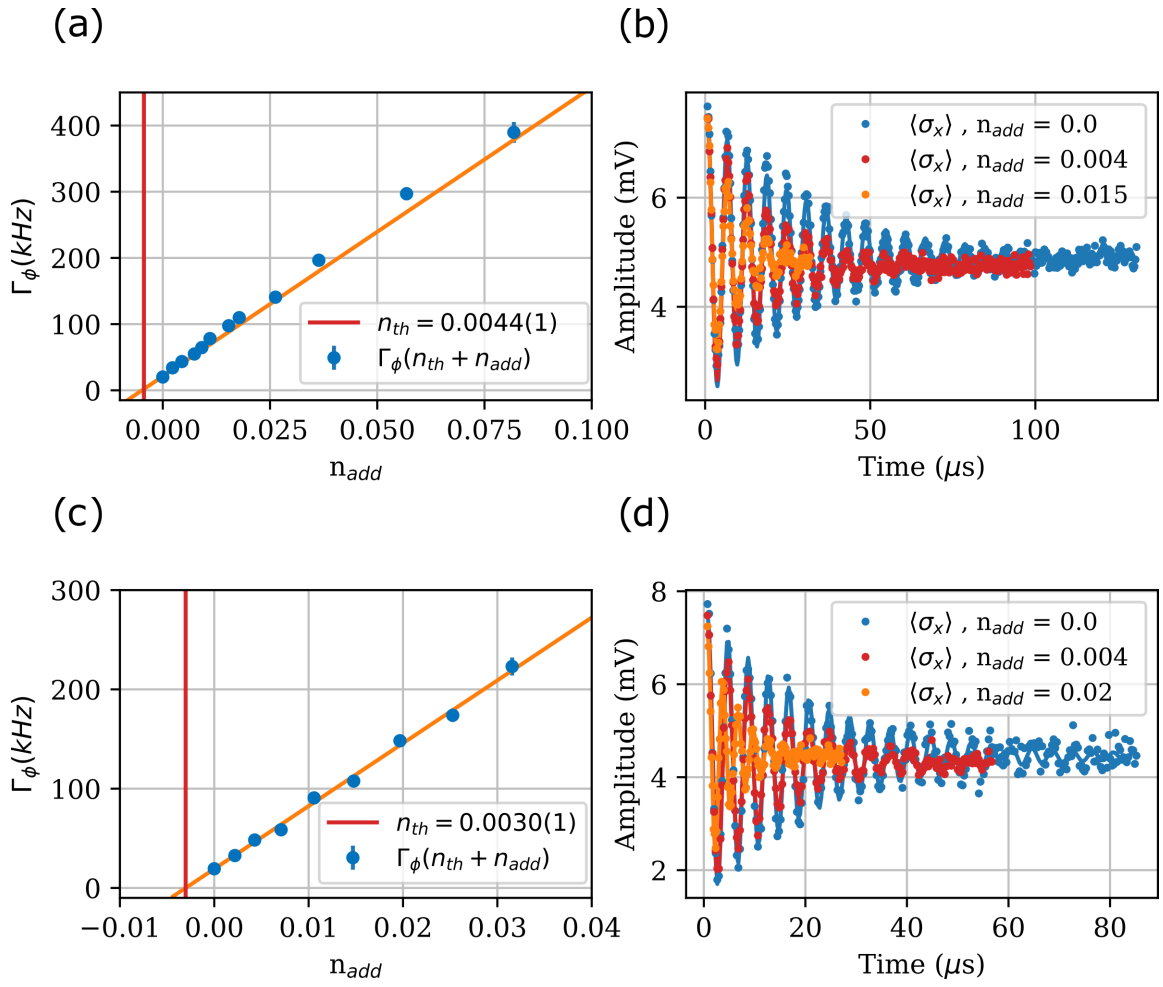

Figure 7.1.4: Cavity temperature measurement
(a) Dephasing rate Γ_ϕ of qubit 1 with respect to the injected noise n_{add} at cavity frequency. The intercept of the line represents the mean number of photons relative to the temperature of the cavity. **(b)** T_{echo} measurements of qubit 1 performed at different injected number of photons n_{add}. **(c, d)** Dephasing rate Γ_ϕ and relative T_{echo} measurements performed with qubit 2 .

7.2 Second cooldown: BRCA on input

The main feature of the experimental apparatus in the second cooldown (see fig. 6.1.1) is represented by the presence of the Broadband Reflective Cavity attenuator (BRCA) between the qubit-cavity system and the input bath. We recall here that the BRCA is nothing else than a home made cavity attenuator in series with a section of a 3D aluminium waveguide (see figure 6.4.1, panel **a** and **b**).

In the same way as the previous section, the experimental results of to the second cooldown are divided in two parts: subsection 7.2.1 deals with the benchmarking of the qubits-cavity system while subsection 7.2.2 deals with the temperature measurements.

7.2.1 Characterization

As usual, the first step of the second cooldown experiments is a set of measurements performed in order to characterize the qubit-cavity system, which are displayed in fig. 7.2.1. The first thing that we can note is that the measurements for qubit 1 are not present, as it has been shortened during the warm-up/ cool-down procedures. The parameters for the qubit 2 -cavity system extracted through the measurements shown in fig. 7.2.1 are displayed in tab. 7.2.1.

It is interesting to discuss how the qubit 2 parameters changed between the second cooldown and the first cooldown (respectively tab. 7.2.1 and tab. 7.1.1). First of all, the frequency of the qubit ω decreased by about 11 MHz, which is expected from the usual aging of the Josephson Junctions. The anharmonicity α remained the same within the range of error while the dispersive shift χ slightly changes due to the change of frequency of the qubit. The qubit-cavity coupling calculated results to be changed slightly out of the range of error ($\simeq 6\,\sigma$). The relaxation times T_1, T_2 and T_{echo} experienced a general decreasing with respect to the former values. For T_1 and T_{echo} those differences are almost in the range of error, while for T_2 the variation change is about the 30 % of the former value.

	$\omega/2\pi$ (GHz)	α (MHz)	$g/2\pi$ (MHz)	$\chi/2\pi$ (MHz)
qb_2	6.831202(5)	287.03(2)	178.18(5)	3.684(3)

	T_1 (μs)	T_2 (μs)	T_E (μs)	$T_{purcell}$ (μs)
qb_2	18.6(3)	14.8(6)	23.8(5)	27.0(3)

	$\omega/2\pi$ (GHz)	$\kappa/2\pi$(MHz)
Cav	9.203666(3)	1.05(1)

Table 7.2.1: In the table above we can see results of the characterization measurement of qubit 2 shown in fig. 7.2.1

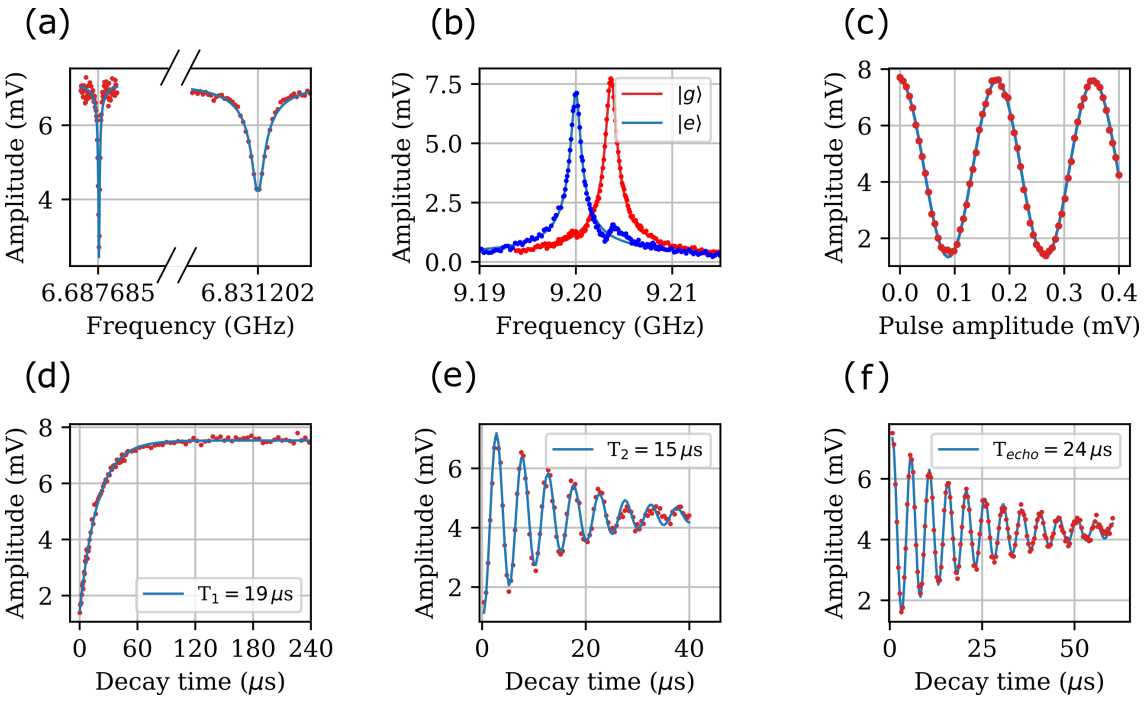

Figure 7.2.1: Qubit 2 characterization- second cooldown
(a) Qubit spectroscopy. **(b)** Cavity spectroscopy. **(c)** Pulse calibration. **(d)** T_1 measurement. **(e)** T_2 measurement. **(f)** T_{echo} measurement.

7.2.2 Temperature measurements

The cavity temperature measurements and the qubit 2 temperature measurements are shown respectively in panel **(a)** and **(b)** of fig. 7.2.2 and panel **(c)** of fig. 7.2.2.

The steady state solutions of the qubits in the excited state ρ_{11} $(t >> 1/T_1)$, the qubit 2 temperature $T_{eff}(\omega_{qb})$, the mean number of photons in the readout resonator for the steady state n_{th} $(t >> 1/\kappa)$ and the relative cavity temperature $T_{eff}\,(\omega_{cav})$ are summarized in tab. 7.1.2.

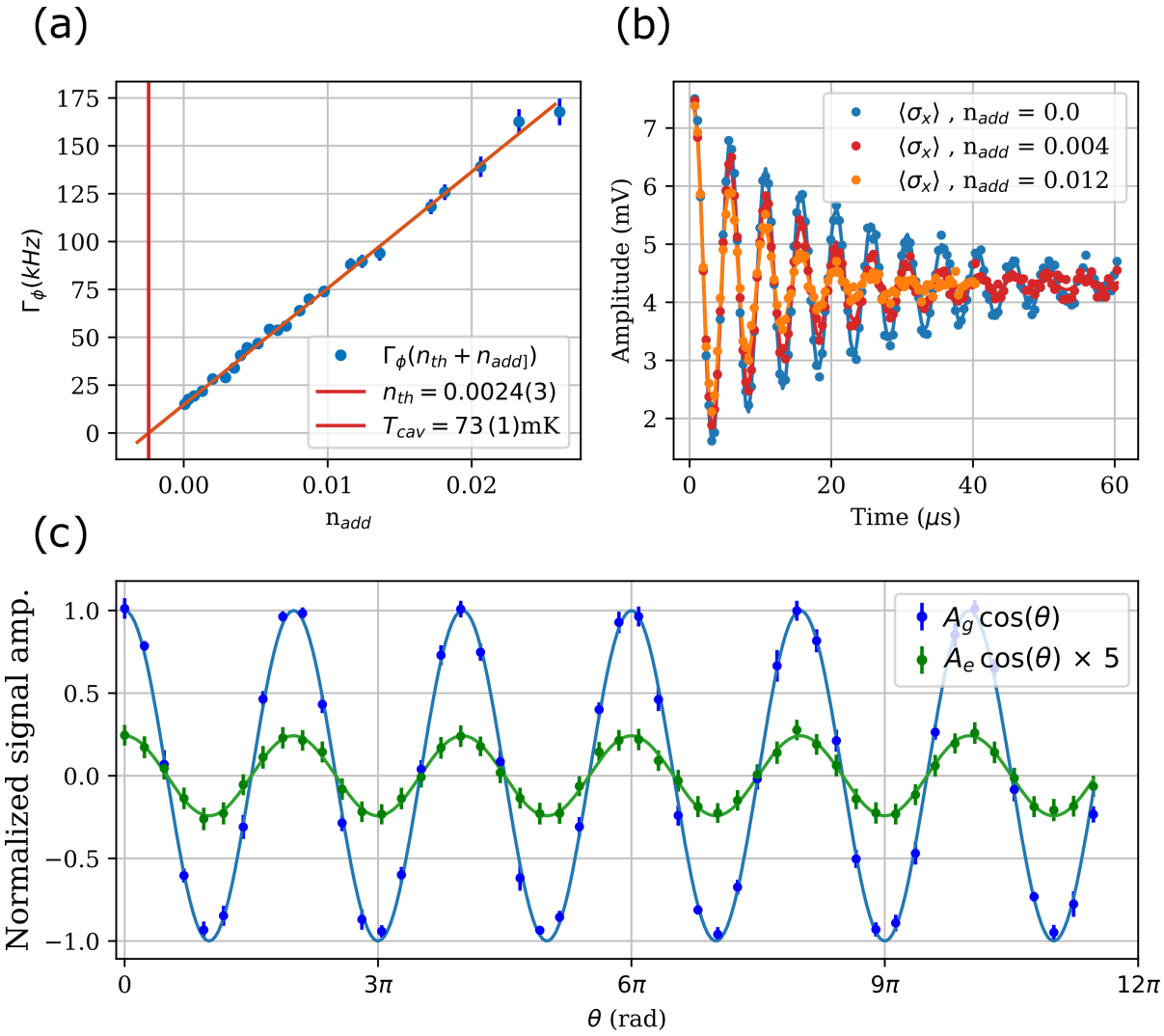

Figure 7.2.2: Temperature measurement- Qubit 2 and cavity-
(a) Dephasing rate Γ_ϕ of qubit 2 with respect to the injected noise n_{add} at the cavity frequency. The intercept of the line represents the mean number of photons relative to the temperature of the cavity. **(b)** T_{echo} measurements of qubit 2 performed at different injected number of photons n_{add}. **(c)** Rabi population measurement performed on qubit 2.

	ρ_{11} $(t >> 1/T_1)$	T_{eff} (ω_{qb})
$\mathbf{qb_2}$	4.6 (1) %	108 (1) mK
	n_{th} $(t >> 1/\kappa)$	T_{eff} (ω_{cav})
Cav	0.0024(3)	73(1)

Table 7.2.2: In the table above we can see the results of the temperature measurements shown in fig. 7.2.2

7.3 Temperature: theoretical model and results

The temperature measurements performed in previous sections are plotted along with the theoretical predictions in fig. 7.3.1. The solid lines represent the expected temperature distribution of the reservoirs relative to the input line and output line. As we have already seen in chapter 4, the properties of those baths can be recovered from the voltage noise spectral density propagation through the lines (see eq. 4.1.4 and eq. 4.1.5).

The green points represent the theoretical predictions for the qubits and cavity temperature for the first cooldown (dots) and second cooldown (squares). These values have been calculated with eq. 4.1.7 and 4.1.8 in the approximation of low internal losses ($\kappa_{loss}, \gamma_{loss} \simeq 0$). The values of the input coupling κ_{in} used in the equations above are modified from the first to the second cooldown due to the transmission properties of the "input couplers" (i.e. the waveguide section and the BRCA) following eq. 4.2.1. The grey and black dots represent the temperature measurements performed respectively in the first and in the second cooldown.

As we can see, the qubit temperature measured through the RPM technique seems to differ drastically from the theoretical predictions. Indeed, since the qubits were coupled to the environment through the readout resonator, and since the readout resonator was massively overcoupled to the output line, the qubits were expected to thermalize to the temperature of the output bath.

The temperature measurements of the cavity through the qubit dephasing seems to be described reasonably well in the model. As we can see, the temperature measurements of the cavity in the first cooldown is $T_{cav} < 81\,\text{mK}$ and $T_{cav} < 76\,\text{mK}$ (grey points at $\simeq$ 9.1 GHz), which are consistent (taking into account that these values are upper limits) with the theoretical prediction (square green point) of 67 mK. Moreover, it is interesting to note that after having decoupled further the quantum system from the input bath through the use of the BRCA, the theoretical value of the effective thermal bath has been moved to a value $\simeq 4$ mK lower, in agreement with the measurement performed on the second cooldown (black point).

From a general point of view, there are many reasons why the Circuit QED system may turn out hotter than expected: thermalization problems in the attenuators and isolators, underestimation of room temperature noise through the HEMT, backaction from the HEMT, underestimation of the noise coming from the internal losses of the cavity. Nevertheless, the fact that the theoretical model agrees with the cavity temperature but not to the qubits temperature points out that the qubits probably couple to additional "hot" reservoirs through their internal loss channels.

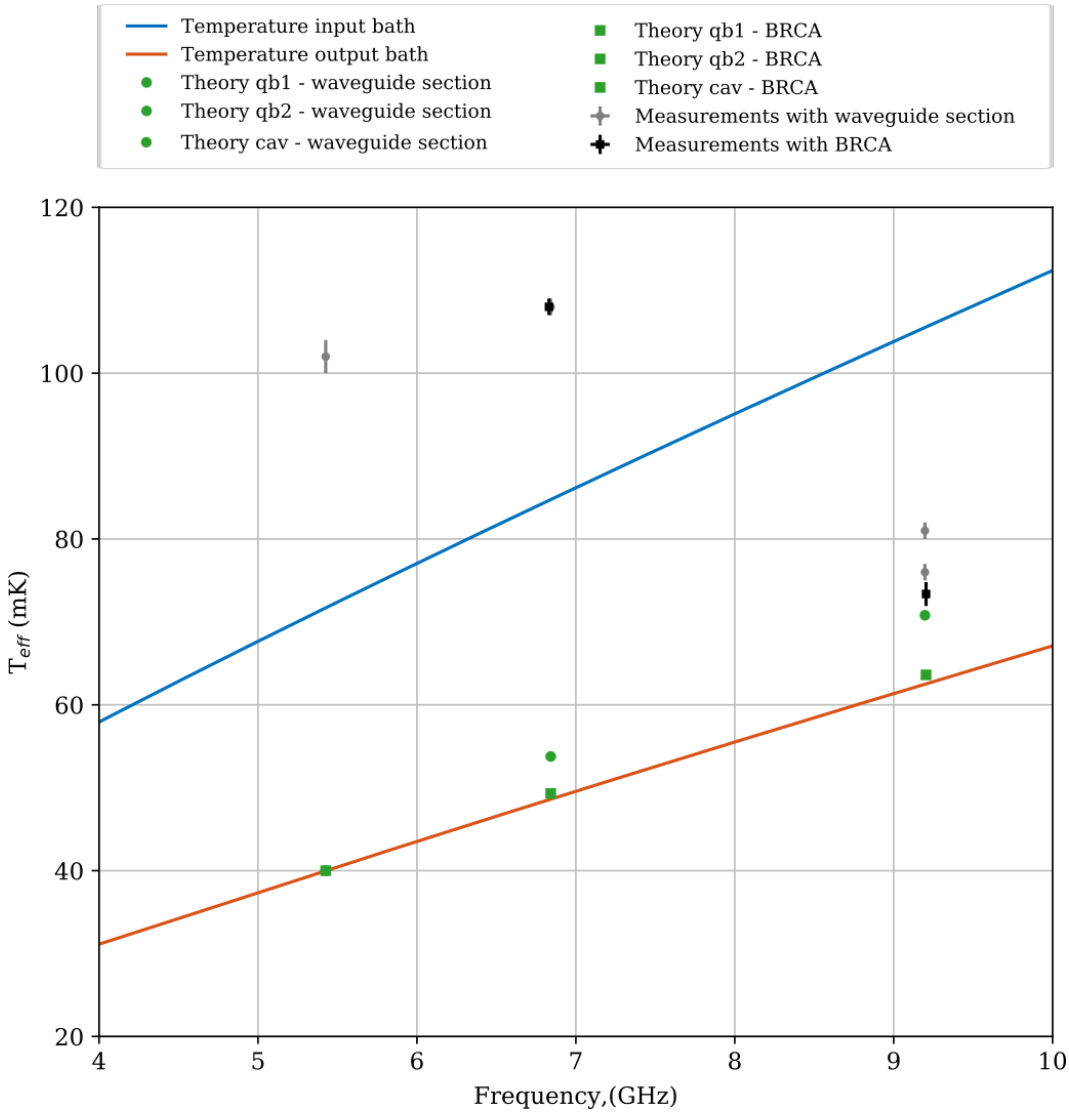

Figure 7.3.1: Theoretical model and experimental results
In the picture above we can see the comparison between the theoretical model that describes the temperature of the qubit and cavity and the measurements performed in the two cooldowns. The orange line and blue lines represent the expected temperature of the input and output baths calculated with eq. 4.1.4 and eq. 4.1.5. The green points represent the theoretical values of temperatures for the qubits and the cavity (see eq. 4.1.7 and eq. 4.1.8) in the approximation of no internal losses. The grey dots and the black dots represent the experimental results shown in section 7.1.2 and section7.2.2.

Chapter 8

Conclusions and outlook

The main objective of this thesis was to characterize the thermal noise which couples to both the qubit and the cavity in our Circuit QED architecture. In order to accomplish this task, the quantum properties of the qubit as the steady state population or the dephasing are measured.

Chapter 3 and chapter 4 describe the interaction between the qubit (or cavity) and multiple baths in terms of an interaction between the quantum system and a fictitious single "effective" thermal bath. Moreover, it was shown how the temperature T^{eff} and mean noise photon occupation number n_{th}^{eff} of the effective thermal baths depend on the relative coupling rates between the quantum system and the thermal baths composing the effective thermal bath.

These features have been investigated through the introduction of different lossless reflective elements (the waveguide section and the BRCA) which modify the coupling of the Circuit QED system to the input bath and the consecutives measurements of the qubits and cavity temperatures.

The comparison between the measured temperatures and the theoretical predictions has been discussed in section 7.3. We have seen that the theoretical model strongly deviates in the prediction of the measured qubit temperatures, while it is consistent with the measured cavity temperatures. This suggests the interpretation that the qubits could have been coupled to additional "hot" reservoirs.

8.1 Improving the experimental apparatus

Future steps that have to be taken to decrease the temperature of the effective thermal bath that couples to the qubits and the readout resonator are described in the following. As we have already seen in section 4.3, there are two main approaches that can be used in order to change the temperature of the effective thermal bath:

- change the mean number of photons n_{th}^{i} relative to the i baths
- change the relative couplings rates κ^{i} between the quantum system and the baths.

As a matter of principle, the first approach can be implemented by increasing the attenuation of every link between the environment and the Circuit QED system. Nevertheless, it is well known that this solution is in general not effective, because of the poor thermalization properties of the attenuators [7] at base temperature. In fact, if the attenuators are not able to dump the hot microwave photons into the cold cryostat

plate, they will inevitably warm up and become a source of hot photons too. Moreover, the temperature of the commercial attenuators is strongly dependent on the amount of power that they are required to dissipate [9] (for example, some commercial attenuators heat up to $\simeq 100\,\mathrm{mK}$ by dissipating $\simeq 10\,\mathrm{nW}$ of power). In order to work in that direction it is very important to use special attenuators with remarkable attenuation properties, as the "Hot electron heatsinks" microwave attenuators (see [36] and [9]) and the cavity attenuators (see [7]).

The second approach can be performed by choosing carefully the coupling between the Circuit QED and the different baths. In fact, if we attach a very cold bath to the quantum system and we maximize the coupling of the qubit to that bath, the mean number of photons of the effective thermal bath would move towards the value of the cold bath. Physically, that means that we would cool the cavity by giving to the cavity the chance to "dump" the hot photons to a cold reservoir. One possible experimental apparatus configuration that could reduce the thermal effects on the quantum system using both principles is shown in figure 8.1.1 . As we can see, on the output line the first approach is used: one isolator is added with the effect of lowering the contribution of thermal noise from the output line by about $\simeq 20\,\mathrm{mK}$.

The work on the input line is based on the second approach. As we can see, in front of the input port of the quantum system a directional coupler is placed. The directional coupler is a lossless object which provides different couplings between its four ports. It forms by itself an "effective" input bath for the quantum system, composed by the input line, the trash line and the $50\,\Omega$ load. The idea in order to create a "cold" effective input bath, is to increase the coupling between the quantum system and the colder reservoir attached to the directional coupler. In the wiring proposal shown in fig. 8.1.1 the cold reservoir is represented by the $50\,\Omega$ load. It is important to stress that this object has to be well thermalized in order to create a "cold" effective input bath: this load would represent a *heat sink* in which the hot photons coming from the quantum system can be dumped in.

The advantage that comes from the present attenuation scheme on the input line with respect to the old one (see 6.1.1) is that, for equal thermalization properties, in the new scheme the load at the base temperature plate is expected to be colder than the attenuator at the base temperature plate in the previous setup. This hypothesis comes from the fact that the power that the load would have to dissipate would be mainly the power of the drive reflected by the cavity, that is much less of the power that an attenuator would have to dissipate in the previous (see fig. 6.1.1) configuration.

For example, let's imagine to send 10 nW of power to the quantum system from an input line in which the last attenuator at base plate attenuates 20 dB. Let's assume also that the quantum system reflects 90 % of the power sent. It is clear that

$$\begin{aligned} P_{qubit} &= 10\,\mathrm{nW} \\ P_{in} &= 1\,\mu\mathrm{W} \\ P_{ref} &= 9\,\mathrm{nW} \\ P_{diss} &= P_{in} - P_{in}/100 + P_{ref} - P_{ref}/100 \\ &\simeq 981\,\mathrm{nW} \end{aligned}$$

with the result that the attenuator at 20 mK has to dissipate 981 nW of power. In the proposed configuration, the input line has an isolation of 20 dB to the quantum system and of 40 dB to the load. For the same power condition of the drive applied to the

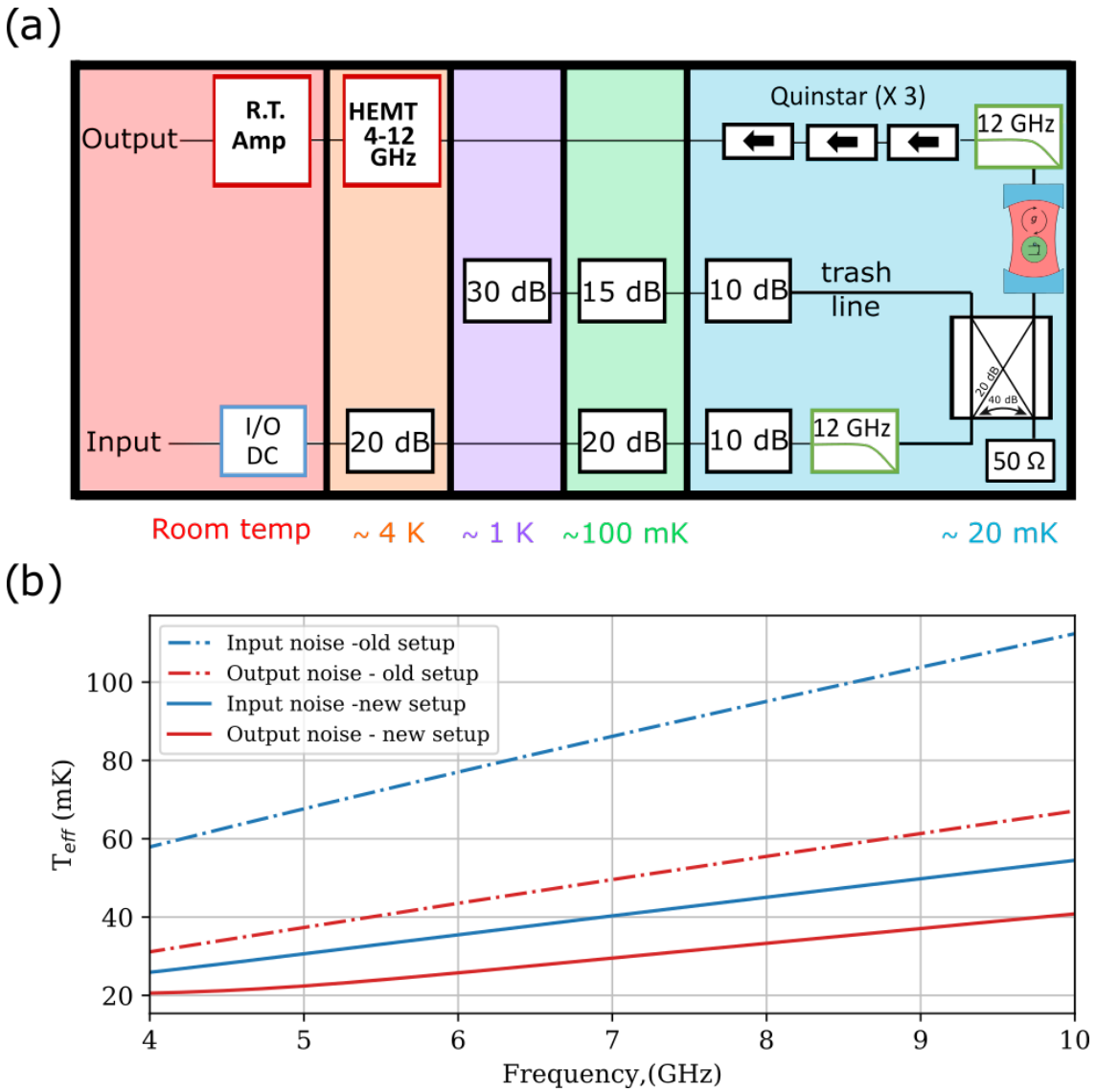

Figure 8.1.1: New wiring proposal
(a) Wiring configuration suggested for minimize thermal noise from input and output line. **(b)** Comparison between the best case scenario input and output bath temperatures for the actual wiring configuration (dashed lines) and the suggested configuration (solid lines) of panel **a**.

quantum system, we would see

$$\begin{aligned} P_{qubit} &= 10\,\mathrm{nW} \\ P_{in} &= 1\,\mu\mathrm{W} \\ P_{in}^{load} &= 0.1\,\mathrm{nW} \\ P_{ref}^{load} &= 9\,\mathrm{nW} \\ P_{diss} &= P_{in}^{load} - P_{in}^{load}/100 + P_{ref}^{load} - P_{ref}^{load}/100 \\ &\simeq 9\,\mathrm{nW} \end{aligned}$$

As we can see, the amount of power that the load would have to dissipate in this configuration is much less, which release the thermalization problem.

Bibliography

[1] Philip Krantz, Morten Kjaergaard, Fei Yan, Terry P Orlando, Simon Gustavsson, and William D Oliver. A quantum engineer's guide to superconducting qubits. *Applied Physics Reviews*, 6(2):021318, 2019.

[2] Frank Arute, Kunal Arya, Ryan Babbush, Dave Bacon, Joseph C Bardin, Rami Barends, Rupak Biswas, Sergio Boixo, Fernando GSL Brandao, David A Buell, et al. Quantum supremacy using a programmable superconducting processor. *Nature*, 574(7779):505–510, 2019.

[3] Long B Nguyen, Yen-Hsiang Lin, Aaron Somoroff, Raymond Mencia, Nicholas Grabon, and Vladimir E Manucharyan. High-coherence fluxonium qubit. *Physical Review X*, 9(4):041041, 2019.

[4] Alex PM Place, Lila VH Rodgers, Pranav Mundada, Basil M Smitham, Mattias Fitzpatrick, Zhaoqi Leng, Anjali Premkumar, Jacob Bryon, Sara Sussman, Guangming Cheng, et al. New material platform for superconducting transmon qubits with coherence times exceeding 0.3 milliseconds. *arXiv preprint arXiv:2003.00024*, 2020.

[5] Yu Nakamura, Yu A Pashkin, and Jaw Shen Tsai. Coherent control of macroscopic quantum states in a single-cooper-pair box. *nature*, 398(6730):786–788, 1999.

[6] Chad Rigetti, Jay M Gambetta, Stefano Poletto, BLT Plourde, Jerry M Chow, AD Córcoles, John A Smolin, Seth T Merkel, JR Rozen, George A Keefe, et al. Superconducting qubit in a waveguide cavity with a coherence time approaching 0.1 ms. *Physical Review B*, 86(10):100506, 2012.

[7] Z Wang, S Shankar, ZK Minev, P Campagne-Ibarcq, A Narla, and Michel H Devoret. Cavity attenuators for superconducting qubits. *Physical Review Applied*, 11(1):014031, 2019.

[8] Fei Yan, Simon Gustavsson, Archana Kamal, Jeffrey Birenbaum, Adam P Sears, David Hover, Ted J Gudmundsen, Danna Rosenberg, Gabriel Samach, Steven Weber, et al. The flux qubit revisited to enhance coherence and reproducibility. *Nature communications*, 7(1):1–9, 2016.

[9] Jen-Hao Yeh, Yizhou Huang, Rui Zhang, Shavindra Premaratne, Jay LeFebvre, FC Wellstood, and BS Palmer. Hot electron heatsinks for microwave attenuators below 100 mk. *Applied Physics Letters*, 114(15):152602, 2019.

[10] David P DiVincenzo. The physical implementation of quantum computation. *Fortschritte der Physik: Progress of Physics*, 48(9-11):771–783, 2000.

[11] Michael A Nielsen and Isaac Chuang. *Quantum computation and quantum information*. American Association of Physics Teachers, 2002.

[12] Jung S.W. Jeong YH. Hirayama Y. Fujisawa T., Hayashi T. *Single-electron charge qubit in a double quantum dot*. Springer, 2006.

[13] David Deutsch. Quantum theory as a universal physical theory. *International Journal of Theoretical Physics*, 24(1):1–41, 1985.

[14] David M Pozar. *Microwave Engineering 3e*. Wiley, 2006.

[15] Jens Koch, M Yu Terri, Jay Gambetta, Andrew A Houck, DI Schuster, J Majer, Alexandre Blais, Michel H Devoret, Steven M Girvin, and Robert J Schoelkopf. Charge-insensitive qubit design derived from the cooper pair box. *Physical Review A*, 76(4):042319, 2007.

[16] HFSS Ansoft. 3-d electromagnetic simulation software. *Ansoft corp., Pittsburgh, PA*, 2009.

[17] Alexandre Blais, Ren-Shou Huang, Andreas Wallraff, Steven M Girvin, and R Jun Schoelkopf. Cavity quantum electrodynamics for superconducting electrical circuits: An architecture for quantum computation. *Physical Review A*, 69(6):062320, 2004.

[18] DI Schuster, Andrew Addison Houck, JA Schreier, A Wallraff, JM Gambetta, A Blais, L Frunzio, J Majer, B Johnson, MH Devoret, et al. Resolving photon number states in a superconducting circuit. *Nature*, 445(7127):515–518, 2007.

[19] RJ Schoelkopf and SM Girvin. Wiring up quantum systems. *Nature*, 451(7179):664–669, 2008.

[20] Jay Gambetta, Alexandre Blais, David I Schuster, Andreas Wallraff, L Frunzio, J Majer, Michel H Devoret, Steven M Girvin, and Robert J Schoelkopf. Qubit-photon interactions in a cavity: Measurement-induced dephasing and number splitting. *Physical Review A*, 74(4):042318, 2006.

[21] Sigmund Kohler. Dispersive readout: Universal theory beyond the rotating-wave approximation. *Physical Review A*, 98(2):023849, 2018.

[22] Vladimir B Braginsky and F Ya Khalili. Quantum nondemolition measurements: the route from toys to tools. *Reviews of Modern Physics*, 68(1):1, 1996.

[23] Grégoire Ithier. *Manipulation, readout and analysis of the decoherence of a superconducting quantum bit*. PhD thesis, 2005.

[24] Wojciech H Zurek. Pointer basis of quantum apparatus: Into what mixture does the wave packet collapse? *Physical review D*, 24(6):1516, 1981.

[25] Wojciech H Zurek. Environment-induced superselection rules. *Physical review D*, 26(8):1862, 1982.

[26] J Robert Johansson, Paul D Nation, and Franco Nori. Qutip 2: A python framework for the dynamics of open quantum systems. *Computer Physics Communications*, 184(4):1234–1240, 2013.

[27] Daniel F Walls and Gerard J Milburn. *Quantum optics*. Springer Science & Business Media, 2007.

[28] Zbigniew Ficek and Mohamed Ridza Wahiddin. *Quantum optics for beginners*. CRC Press, 2014.

[29] André Xuereb, Alberto Imparato, and Aurélien Dantan. Heat transport in harmonic oscillator systems with thermal baths: application to optomechanical arrays. *New Journal of Physics*, 17(5):055013, 2015.

[30] AA Clerk and D Wahyu Utami. Using a qubit to measure photon-number statistics of a driven thermal oscillator. *Physical Review A*, 75(4):042302, 2007.

[31] Sebastian Krinner, Simon Storz, Philipp Kurpiers, Paul Magnard, Johannes Heinsoo, Raphael Keller, Janis Luetolf, Christopher Eichler, and Andreas Wallraff. Engineering cryogenic setups for 100-qubit scale superconducting circuit systems. *EPJ Quantum Technology*, 6(1):2, 2019.

[32] Fei Yan, Dan Campbell, Philip Krantz, Morten Kjaergaard, David Kim, Jonilyn L Yoder, David Hover, Adam Sears, Andrew J Kerman, Terry P Orlando, et al. Distinguishing coherent and thermal photon noise in a circuit quantum electrodynamical system. *Physical review letters*, 120(26):260504, 2018.

[33] C Tannous and J Langlois. Classical noise, quantum noise and secure communication. *European Journal of Physics*, 37(1):013001, 2015.

[34] Eyob A Sete, Jay M Gambetta, and Alexander N Korotkov. Purcell effect with microwave drive: Suppression of qubit relaxation rate. *Physical Review B*, 89(10):104516, 2014.

[35] Evan Jeffrey, Daniel Sank, JY Mutus, TC White, J Kelly, R Barends, Y Chen, Z Chen, B Chiaro, A Dunsworth, et al. Fast accurate state measurement with superconducting qubits. *Physical review letters*, 112(19):190504, 2014.

[36] Jen-Hao Yeh, Jay LeFebvre, Shavindra Premaratne, FC Wellstood, and BS Palmer. Microwave attenuators for use with quantum devices below 100 mk. *Journal of Applied Physics*, 121(22):224501, 2017.

[37] Michael Lee Roukes, MR Freeman, RS Germain, RC Richardson, and MB Ketchen. Hot electrons and energy transport in metals at millikelvin temperatures. *Physical review letters*, 55(4):422, 1985.

[38] FC Wellstood, C Urbina, and John Clarke. Hot-electron effects in metals. *Physical Review B*, 49(9):5942, 1994.

[39] Kurtis Geerlings, Zaki Leghtas, Ioan M Pop, Shyam Shankar, Luigi Frunzio, Robert J Schoelkopf, Mazyar Mirrahimi, and Michel H Devoret. Demonstrating a driven reset protocol for a superconducting qubit. *Physical review letters*, 110(12):120501, 2013.

[40] XY Jin, A Kamal, AP Sears, T Gudmundsen, D Hover, J Miloshi, R Slattery, F Yan, J Yoder, TP Orlando, et al. Thermal and residual excited-state population in a 3d transmon qubit. *Physical review letters*, 114(24):240501, 2015.

[41] Theodore Walter, Philipp Kurpiers, Simone Gasparinetti, Paul Magnard, Anton Potočnik, Yves Salathé, Marek Pechal, Mintu Mondal, Markus Oppliger, Christopher Eichler, et al. Rapid high-fidelity single-shot dispersive readout of superconducting qubits. *Physical Review Applied*, 7(5):054020, 2017.

[42] Eccosorb cr. two part castable load absorber series. http://www.eccosorb.com/Collateral/Documents/English-US/CR.pdf, visited on Feb. 17, 2017). Technical Bulletin. Laird Technologies.